AERODYNAMIC FORCES ON A WEB

SUBJECTED TO THE COANDA AIR JET

By

EUI YEOL HONG

Bachelor of Engineering

Kon-Kuk University
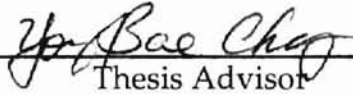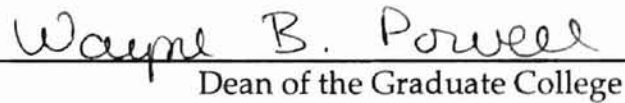
Seoul, Korea

1997

AERODYNAMIC FORCES ON A WEB

SUBJECTED TO THE COANDA AIR JET

Thesis Approved:

Thesis Advisor

Dean of the Graduate College

ACKNOWLEDGMENTS

TABLE OF CONTENTS

LIST OF TABLES

LIST OF FIGURES

xi

NOMENCLATURE

b   Nozzle width (Nozzle opening)

h   Vertical distance between the knife edge and the starting point of curvature, $h = s - R$

F   Aerodynamic traction on the web (Force per unit width of web)

H   Floatation height (Distance between the web and the top surface of the nozzle)

H_o Height of web supports (Distance between the flexible web at the supports and the top surface of the nozzle)

P   Static pressure on the web

p_o Supply air pressure in the plenum

R   Radius of curvature of the 90° convex surface

s   Nozzle offset, $s = h + R$

T   Applied tension on the web (Force per unit width of web)

x   Horizontal distance from the slot nozzle

τ_w Wall shear stress on the web

CHAPTER I

INTRODUCTION

1.1 Background

Thin, flexible materials such as paper, plastic films, metal foils, and fabrics are widely called webs. When web materials are coated or printed, the coated or printed surfaces cannot be touched until they become dry. Some materials such as photographic films require extreme care, and any minor contact during drying of the coatings can cause product defects. Adhesive tapes are another examples of web materials that cannot be handled by contact support rollers only. Air-flotation ovens are widely used for the purpose of drying web materials without mechanical contact. Typical air bars widely used in air-flotation ovens include airfoils (or airfoil bars). An airfoil bar has one slot nozzle through which hot air is ejected along a curved surface. In some designs, the air jet is ejected in the direction nearly parallel to the web. In other designs, the air jet exits a slot nozzle almost perpendicularly to the web, but changes its direction following a curved surface so that its final direction becomes nearly parallel to the web. The Coanda effect is a key in the latter type of designs.

There are some situations where the aerodynamic drag on a moving web is significant enough to be a concern. For example, a tissue web may run at 6000 fpm or faster, and the aerodynamic drag is not negligibly small compared to the web tension. In

1

such situations, a high-speed air jet can be used to maintain the tension constant along the machine direction or to propel the web.

Full-speed threading of paper machines is another area where the air jet can play an important roll. This application is closely related to the above one in that propelling of the web is a major concern. The main difference is that, for threading applications, the air jet needs to be able to handle the incoming free end of web, and web tension can be extremely low or zero.

As the web line speeds are ever increasing, aerodynamic effects become more significant. Air entrainment between a web and a support roller increases with web speed resulting in a slippage, which in turn causes scratches on the web surface. Also the air layer between a fast-moving web and a spreader roller can make the spreader roller malfunction. This trend calls for new methods of web support, spreading, and guiding of web. Air jets can possibly be used for those purposes.

1.2 Problem Statement

It is known that airfoil bars can cause a violent flutter in the web, generate traction on the web to the extent that the tension at the exit is different from that at the entrance of the oven, and sometimes cause touchdowns and touchups. In order to prevent such problems or to use the aerodynamic traction for better control of web dynamics, it is desirable to develop an understanding of the air flow near the air bars in the presence of the web, aerodynamic pressure on the web, aerodynamic traction on the web, and web deflection. Such air-web interaction problems are well understood yet.

In order to propell a tissue web and the like, we need to develop a method of

2

designing air nozzles what can deliver high speed air jets; the flow speed must be greater than the web speed even at a certain distance from the slot nozzle. Also the dynamics of air flow, static pressure on the moving web, and the traction need to be predicted. The air jet can be ejected parallel to the web or the Coanda effect can be used to eject the air in the direction perpendicular to the web and then turn its direction to become parallel to the web. The dynamics of a high speed air jet interacting with a moving web requires a new research. Development of new technologies of web handling require a clear understanding of the phenomena described above, especially the Coanda effect.

1.3   Objectives and Scope of Study

Among the many concerns partially addressed in Sections 1.1 and 1.2, this thesis focuses on the following objectives:

1. Measure and compute the aerodynamic pressure and traction on a rigid web placed near a Coanda air nozzle to provide a basic understanding the Coanda air jet interacting with a web nearby.

2. Measure and compute the aerodynamic pressure and traction on a flexible web subjected to the Coanda air jet.

3. Develop an understanding of the effects of supply air pressure, floatation height, and applied tension on the aerodynamic forces on the web subjected to the Coanda air jet.

CHAPTER II

LITERATURE REVIEW

When a stream of air is ejected into an open area, a large amount of ambient air is entrained into the stream. If there is a solid boundary near the air jet, a negative pressure is developed in the space between the air jet and the solid boundary because the wall blocks the air entrainment. This negative pressure forces the air jet to be bent toward or attached to the wall. This phenomenon is called the Coanda effect, which was discovered by Henry Coanda in 1910. Later Von Karman realized that this was a new phenomenon and named it the Coanda effect (Reba, 1996).

Squire (1950) studied the dynamics of jet flow including the Coanda effect and the effect of the air jet on drag and stability of aircraft. He conducted an experiment and proved that if there is an obstacle that prevents the surrounding from being entrained, a reduction in pressure would cause the air jet to deflect toward the wall.

Bourque and Newman (1960) studied the reattachment of a two-dimensional, incompressible, turbulent air jet near an inclined flat plate. They found that when the length of the plate and the Reynolds number are large they do not strongly affect the behavior of the jet. The angle of inclination of the plate, however, strongly affects the behavior of the flow.

The first European conference was held on the Coanda effect, or boundary layers and jets on curved walls, in Berlin in April 1965. Wille and Fernholz (1965) pointed out

4

two main effects on the Coanda phenomenon: the curvature forced upon the jet by the convex body, and the entrainment of fluid into the jet stream due to turbulent mixing leading to a force on the body in the same direction.

Felsing and Moller (1969) studied the Coanda effect for developing a new technique to control a thick axisymmetrical air jet in the design of VTOL aircraft (vertical take-off and landing craft). They investigated the locations of attachment and separation points over a circular cylinder with fluid injection to the cylinder surface. The low injection and high momentum could provide an efficient flow control in fluidics and VTOL craft.

Wetmore (1972) described a method of using the Coanda nozzle for a grain transporting system. He showed the possibility of using the Coanda nozzle as a pneumatic device.

Cornelius and Lucius (1984) studied the parameters that control the detachment of the Coanda jet from the curved surface. It was found that at a certain pressure ratio, the air jet seemed not to follow the curved wall surface.

Murai and others (1989) described the use of the Coanda effect to make a new phenomenon of jet oscillation in a rectangular duct channel. They found that the condition for stable oscillation of turbulent jet is dependent on the Strouhal number and the shape factor of the duct. They said that this oscillation could improve the mixing characteristics of two liquids.

Due to the tremendous improvement of computer technology in recent years, the field of CFD (computational fluid dynamics) has made great progress in fluid mechanics. The behavior of the Coanda air jet was studied computationally by Thirumal (1998). At

the same time, Aravamudhan (1998) performed an experimental study for applications of the Coanda nozzle used for web handling. They studied many parameters (surface roughness, nozzle width, nozzle offset, supply pressure, floatation height, radius of curvature of the 90° convex surface) to analyze the phenomenon of the Coanda effect. It was found that there are three different behavioral regions: the separated region, the attached region and the bistable region. They studied the interactions such as pressure profile and traction force on the web between a stationary rigid web and the Coanda air nozzle. They compared the computational and experimental results which seemed to agree each other.

CHAPTER III

EXPERIMENTS

3.1 Coanda Air Jet and a Stationary Rigid Web

3.1.1 Experimental setup

The first stage of experiment focused on the interaction between the Coanda air jet and a stationary rigid web. The main objective was to measure the aerodynamic pressure distribution and traction on the web. The measurement of aerodynamic traction is very important to examine the feasibility of using the Coanda air jet to generate the in-plane aerodynamic force on the web.

The setup consisted of a Coanda nozzle, a traversing table, a steel frame, four suspension strings, a rigid web (aluminum plate), and the instruments including a load cell and a pressure transducer. The Coanda nozzle is shown in Figure 1 and Figure 2.

One main component of the test setup was the aluminum block with a sharp edge (A in Figure 2), which was 8 inches high, 6 inches deep, and 3 inches long (in the horizontal direction). The knife edge of the block had an angle of around 45°, and the nozzle width was adjustable. The other aluminum block (B) had a 90° turning convex surface with the radius of curvature of 11/64 inches. Dimensions of the curved surface block were 4 inches in height, 6 inches in depth, and 2 inches in length (horizontal dimension). A flap, 4 inches in length, was attached to block B to increase the effective

length of the block.

The two side walls of the nozzle were made of half-inch thick transparent plaxiglass plates. They were extended about 3.5 inches above the top surface of the nozzle to make air dams for maintaining a two-dimensional flow field. Compressed air was supplied to the settling chamber through two air inlets and ejected through the slot nozzle. The settling chamber was filled with a porous material to make the air flow uniform. A perforated plate held the porous material in place. All these components were mounted on a 0.75-inch thick aluminum base plate.
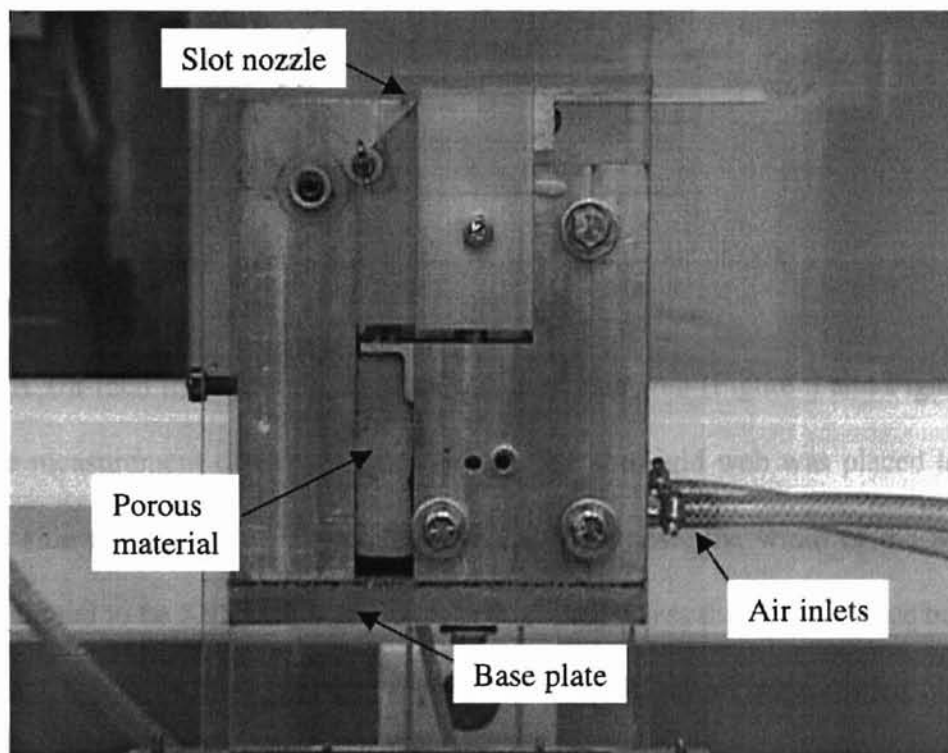
Figure 1. Picture of the Coanda air nozzle
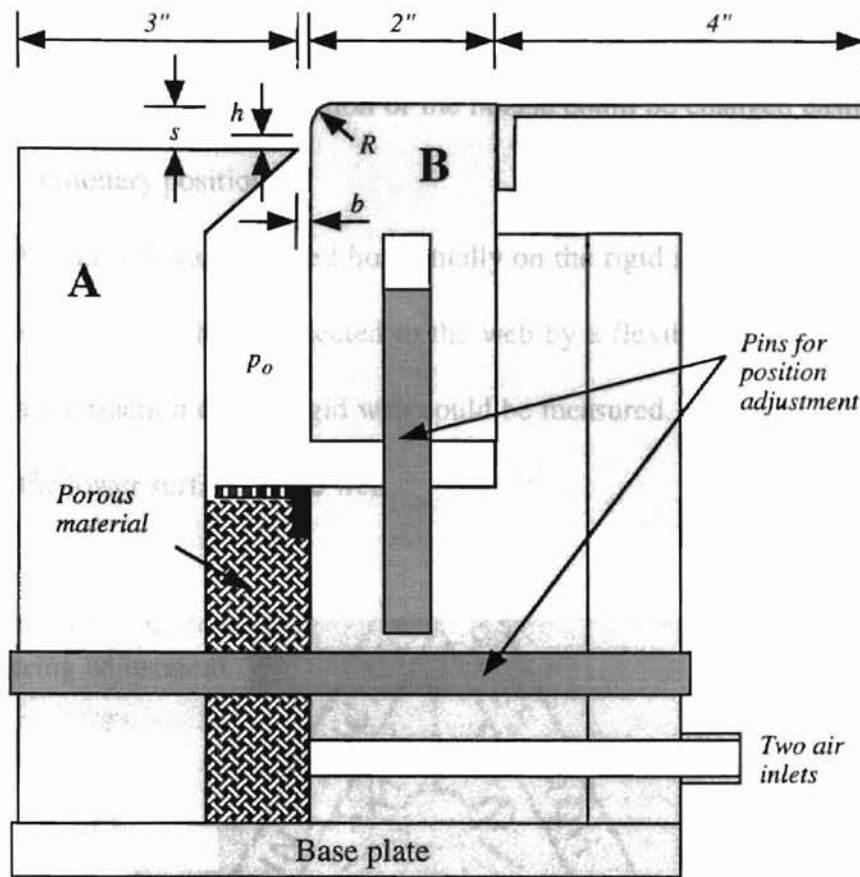
Figure 2. Schematic of the Coanda air nozzle

A 1/8-inch thick aluminum plate was used as a web (Figure 3 and Figure 4). For accurate measurement of the aerodynamic traction, the rigid web was placed in between the two side plates without any contact. For this purpose, the width of the web (plate) was machined to be 5.95 inches, which was 0.05 inches less than the distance between the air dams. A row of three pressure taps 1/32 inch in diameter were drilled on the plate with a space of 2 inches along the center line of the rigid web. A pressure transducer was connected to one of the pressure taps. The web was suspended from the steel frame using four vertical strings. In order to prevent the aerodynamic pressure on the web from affecting the traction measurement, the four suspension stings were carefully aligned. The rod seen at the top in Figure 3 and Figure 4 was used for adjusting the floatation

height of the web. The Coanda air nozzle setup including the air dams was placed on the traversing table so that the position of the nozzle could be changed easily, while the web was in a stationary position.

A load cell was mounted horizontally on the rigid steel frame while the other end of the load cell was then connected to the web by a flexible wire, so that the horizontal aerodynamic traction on the rigid web could be measured. The load cell was at the same level as the lower surface of the web.
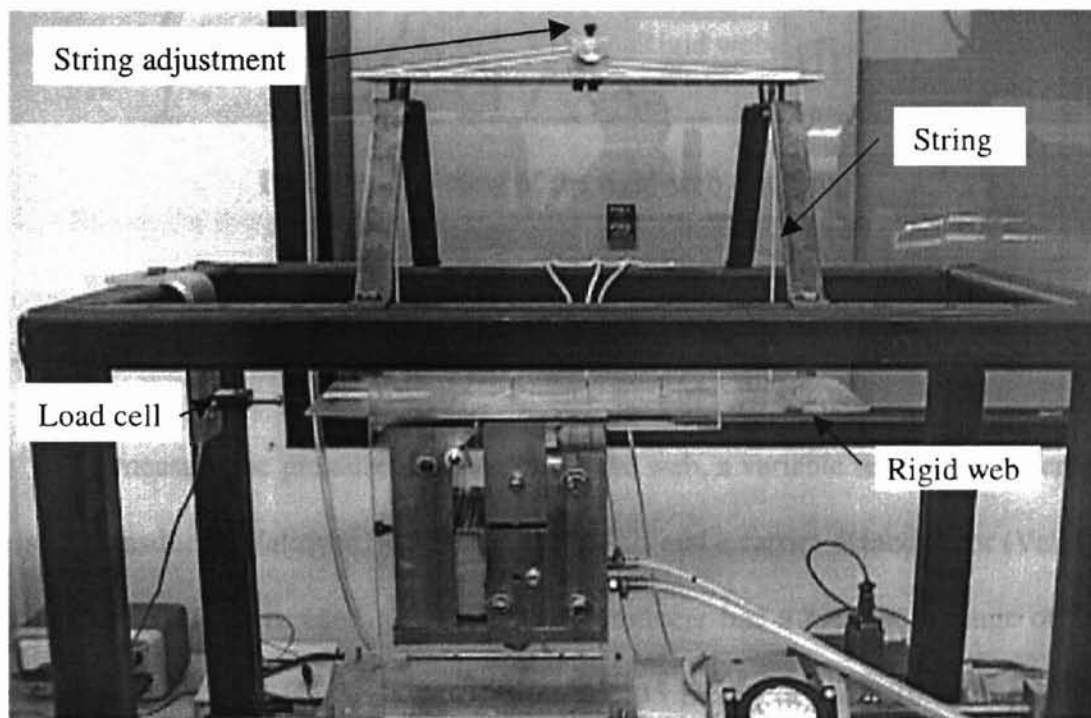
Figure 3. Side view of the rigid-web test setup
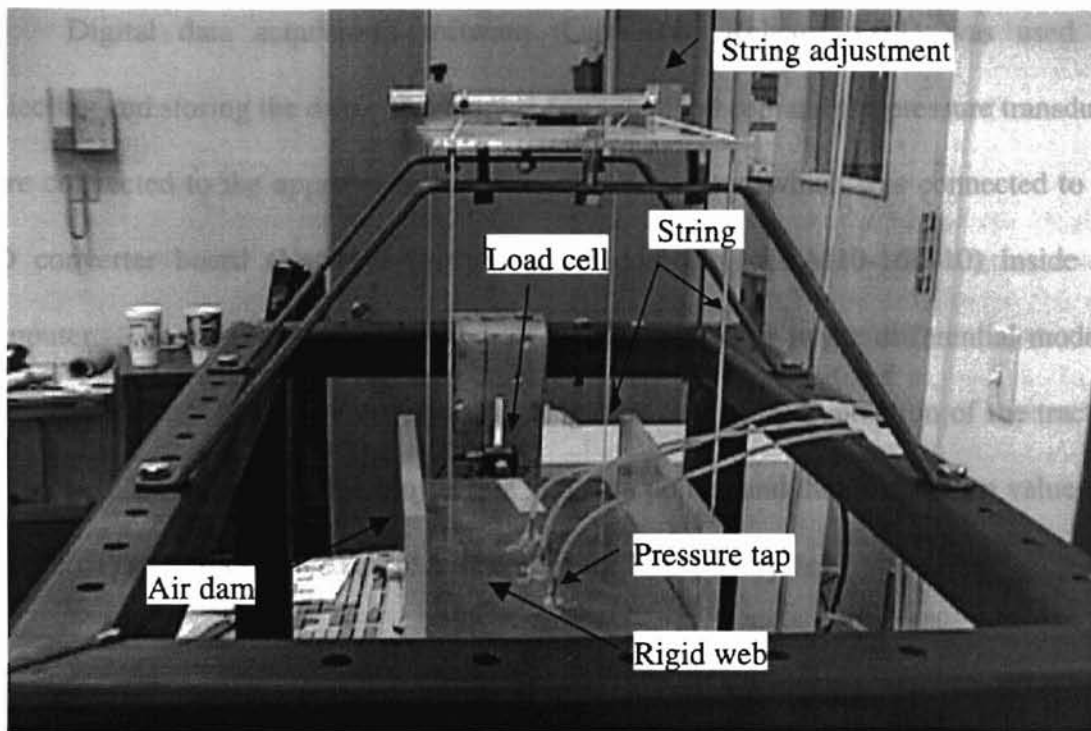
Figure 4. Top view of the rigid-web test setup

3.1.2 Instrumentation

To measure the pressure distribution on the web, a variable reluctance differential pressure transducer (Validyne, Model No. DP15-22) and a carrier demodulator (Validyne, Model No. CD15) were used. The pressure transducer had a maximum range of ± 5.5 inches of water (± 0.2 psi) with a resolution 0.0135 inches of water (0.0005 psi). The carrier yielded a DC voltage output, which was then fed into a digital data acquisition system.

For measurement of the aerodynamic traction force on the web, a strain gage type load cell (Transducer Techniques, Model No. MDB-2.5) was used. This load cell had a maximum range of ± 2.5 lbf with a resolution of 0.00025 lbf with a supply voltage of 10 volts.

Digital data acquisition software (LabVIEW, Release 4.0.1) was used for collecting and storing the data. The outputs from the load cell and the pressure transducer were connected to the appropriate channels of a connector, which was connected to the AD converter board (National Instruments, Model No. AT-M10-16E-10) inside the computer. The data acquisition system was configured to be in the differential mode to read all the data. To reduce the error that might be caused by fluctuation of the traction on the web, it was programmed to sample 200 data points, and then their mean value was recorded. The outputs were stored in text files for future analysis.

3.1.3 Test procedure

Before the test setup was integrated, the pressure transducer and the load cell were calibrated. The pressure transducer was calibrated against a vertical tube manometer in the range of 0 to +2 inches of water. The load cell was calibrated using dead weights in the range of 0 to 0.25 lbf in the compression mode.

After the various geometric parameters of the test setup had been fixed as planned, the setup was placed on the traversing table. Before taking any readings, the center line of the setup was aligned parallel to the direction of motion of the traversing table. If it is not parallel to the direction of traversing of the table, the setup would travel with an angle to the web and the suspended rigid web would be in contact with the side plates (air dams). Then, the top surface of the curved surface block and the surface of the other block were checked and adjusted using levels to ensure that they were parallel to the base plate. One of the important test parameters was the distance of the web from the top surface of the nozzle. The rigid web (aluminum plate) was placed and adjusted above the

12

nozzle at a certain floatation height using a level and a dial calipers. The horizontal position of the load cell was also adjusted and fixed to the web with a flexible wire so that no horizontal displacement of the web would be introduced.

After that, the zero corrections of the load cell and the pressure transducer were checked. Data were then taken while the traversing table was moved a total distance of 9 inches in steps of 0.1 inches, while the rigid web with pressure taps was kept at one position.

The main test parameters were the supply air pressure and the floatation height of the web. The values of the test variables are tabulated in Table 1. The errors of the dead weights used in the load cell calibration are tabulated in Table 2.

Table 1. Rigid-web test conditions

Parameter	Symbol	Value
Radius of curvature	R	11/64 inches
Nozzle width	b	0.01 inches
Nozzle offset	s	0.22 inches
Floatation height	H	0.1-1.0 inches
Supply pressure	p_0	1-3 psig

Table 2. Error of weights

Indicated mass (g)	Measured mass (g)	Error (%)
1.77185	1.7726	4.23×10^{-2}
3.54369	3.5453	4.54×10^{-2}
7.08738	7.0894	2.85×10^{-2}
14.17476	14.1756	0.59×10^{-2}
28.34952	28.3445	1.77×10^{-2}
56.69905	56.6753	4.19×10^{-2}

13

3.1.4 Results and discussion

Pressure profiles

Typical pressure profiles are shown in Figure 5, where the origin of the abscissa corresponds to the location of the slot nozzle. It is seen that the pressure on the web upstream of the slot nozzle is negative (sub-ambient) and it increases to positive values downstream of the slot nozzle. Two dips are observed upstream and near the slot nozzle. Similarly, two positive peaks are observed downstream of the slot nozzle. At further downstream, the pressure gradually decreases to the ambient pressure.

Pressure profile changes with the floatation height. The trend of the profile, however, is not strongly affected by the floatation height. The pressure on the web for the floatation height of 0.15" tends to be higher than that for 0.25".
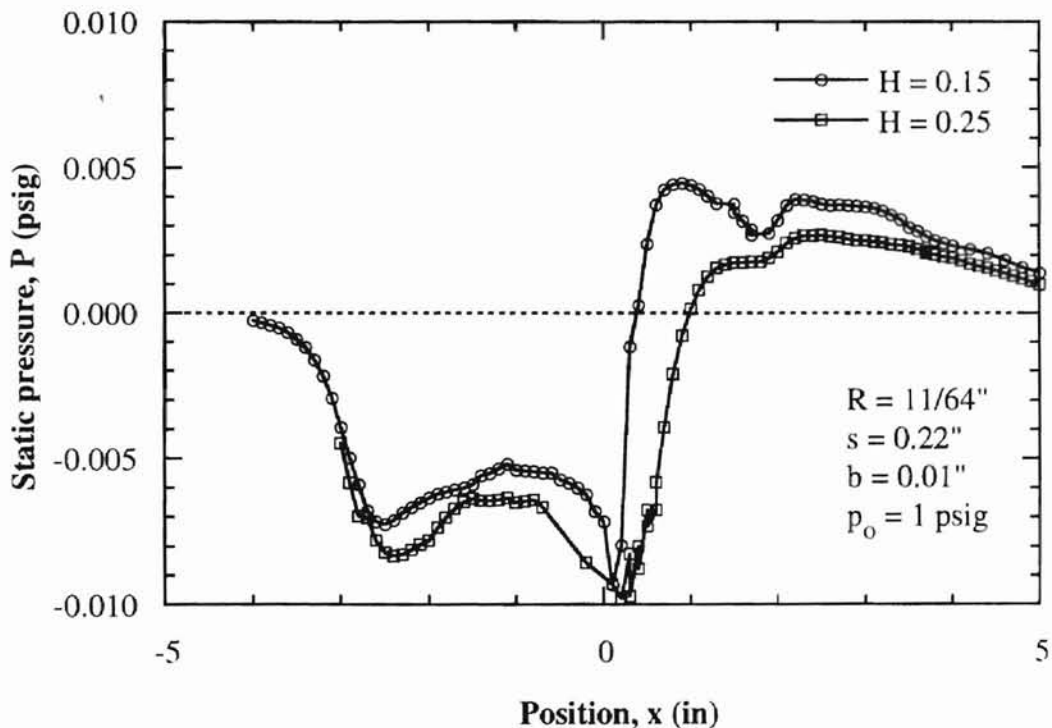
Figure 5. Effects of floatation height on measured pressure profile

Aerodynamic traction

The Coanda nozzle was traversed for the measurement of pressure profile as explained Chapter III. The traction, measured by a miniature load cell, was recorded each time the static pressure was measured. The aerodynamic traction (aerodynamic drag force per unit width of web) was determined by taking the average of those multiple values.

As seen in Figure 6, the aerodynamic traction tends to increase with the supply pressure. The traction for $H = 0.20"$ is always larger than that for $H = 0.25"$ when all other conditions are the same. Figure 7 shows the non-dimensional traction as a function of the supply air pressure. These figures indicate that the aerodynamic traction is nearly proportional to the supply pressure.
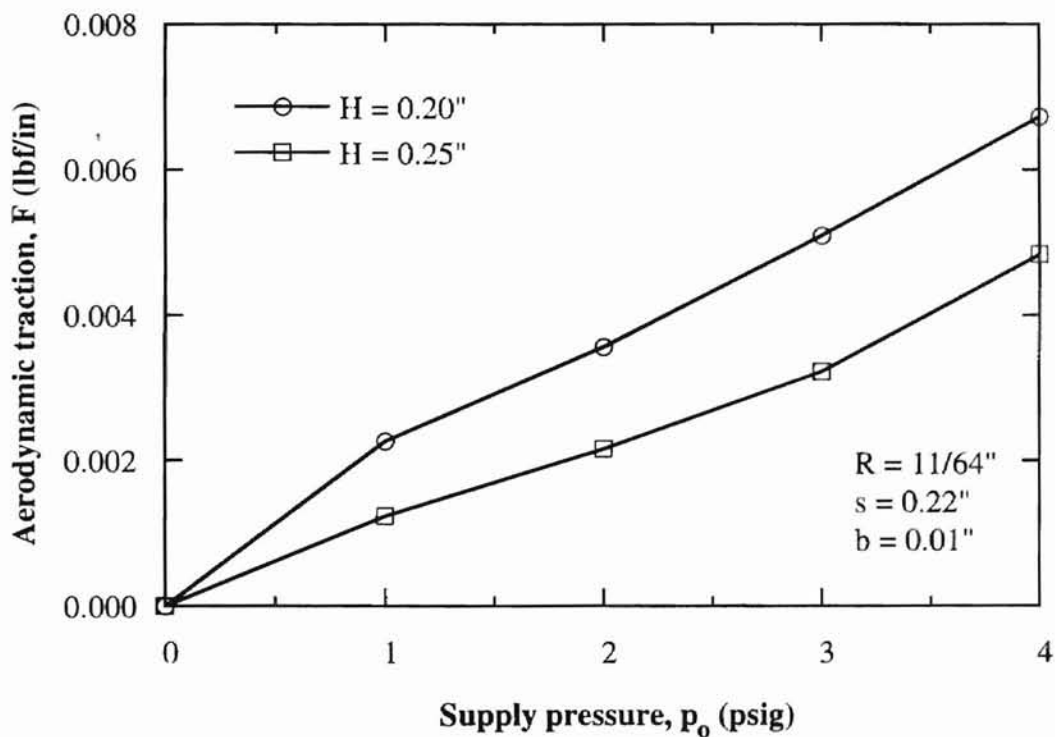
Figure 6. Effects of floatation height on measured traction
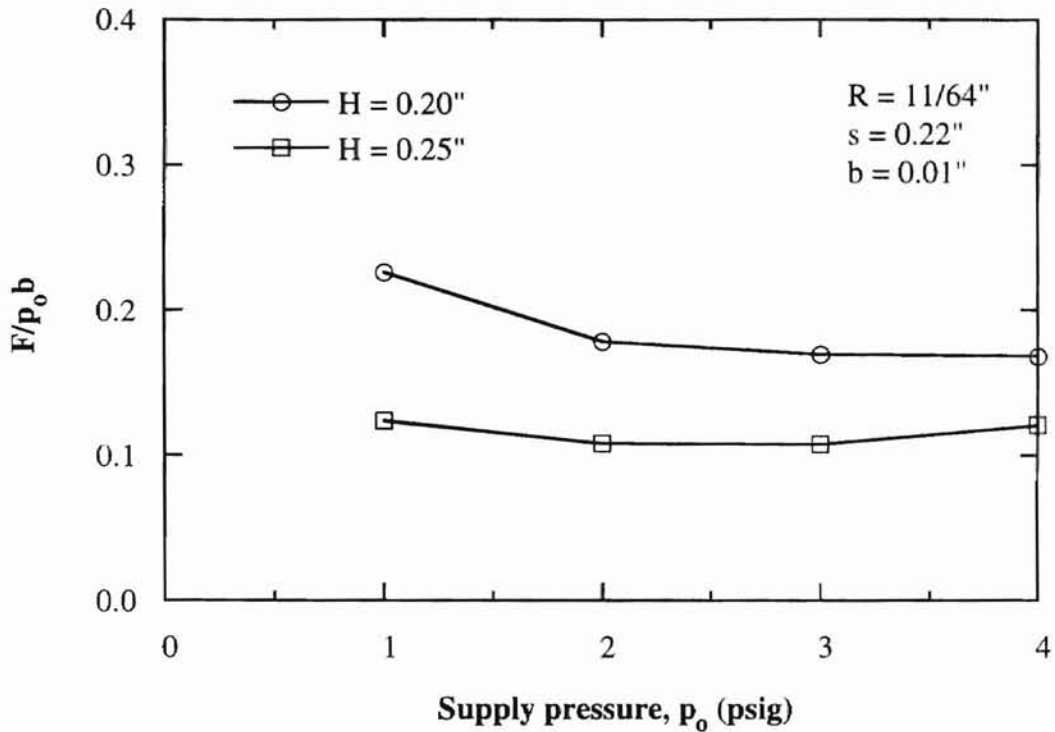
Figure 7. Effects of floatation height on non-dimensional traction

3.1.5 Uncertainty of measurements

.

The pressure transducer had a maximum range of ± 5.5 inches of water (± 0.2 psi) with an accuracy of 0.25 % of full scale, which is ± 0.01375 inches of water (0.0005 psi). The pressure transducer was calibrated against a vertical tube manometer in the range of 0 to 2 inches of water. The uncertainty of the manometer reading was ± 0.025 inches of water (0.0009 psi). The uncertainty of the position of the Coanda air nozzle in the traversing table was $\pm 3.5 \times 10^{-4}$ inches.

The load cell had a maximum range of ± 2.5 lbf with an accuracy of ± 0.00025 lbf when the supply voltage is 10 volts. The uncertainty of the dead weights used for

16

calibration of the load cell was ± 0.00005 g. The accuracy of the supply pressure was ± 0.25 psi.

3.2 Coanda Air Jet and a Stationary Flexible Web

3.2.1 Experimental setup and instrumentation

The second stage of the experiment focused on the interaction of the Coanda jet with a stationary, flexible web. The main concern in this experiment was to find the aerodynamic traction of the air jet on the flexible web; pressure on the web was not measured. The measurement of aerodynamic traction is very crucial to verify the feasibility of using the Coanda air jet to generate the in-plane aerodynamic force to handle web materials.

The same setup used for the rigid-web test was used with a minor modification to accommodate a flexible web. A 0.003 inches thick plastic web material was used. For accurate measurement of the aerodynamic traction, the flexible web was placed in between the two side plates without any contact. For this purpose, the web was cut 5.9 inches in width, which was 0.1 inches less than the distance between the air dams. The web was supported by two air bars, 2 inches in diameter, mounted on the steel frame as shown in Figure 8 and Figure 9. The purpose of supporting the web with air bars was to allow the web to move in the longitudinal direction without friction. The pressure on the web affected the out-of-plane defection profile of the web, which in turn caused longitudinal sliding of the web at the supports. Any friction at the supports would cause an error in the measurement of the aerodynamic traction. Because of the friction-free

supports (air bars) and a flutter of the web, the flexible web sometimes touched the air dams during the test. Contact between the web and the air dams might cause an error in the measurement of the aerodynamic traction on the web. A load cell was fixed on the rigid bottom plate, and its top was fixed to the end of the web by a vertical rod and a string as shown in Figure 9. A micrometer was mounted on the steel frame to measure the out-of-plane deflections of the web at selected points as shown in Figure 10.

The same instruments used for the rigid-web test were used, except the pressure transducer, which was not needed for the flexible-web test. Two identical weights were attached at the two ends of the web to apply web tension. A change of the force on the load cell caused by the air jet was measured.
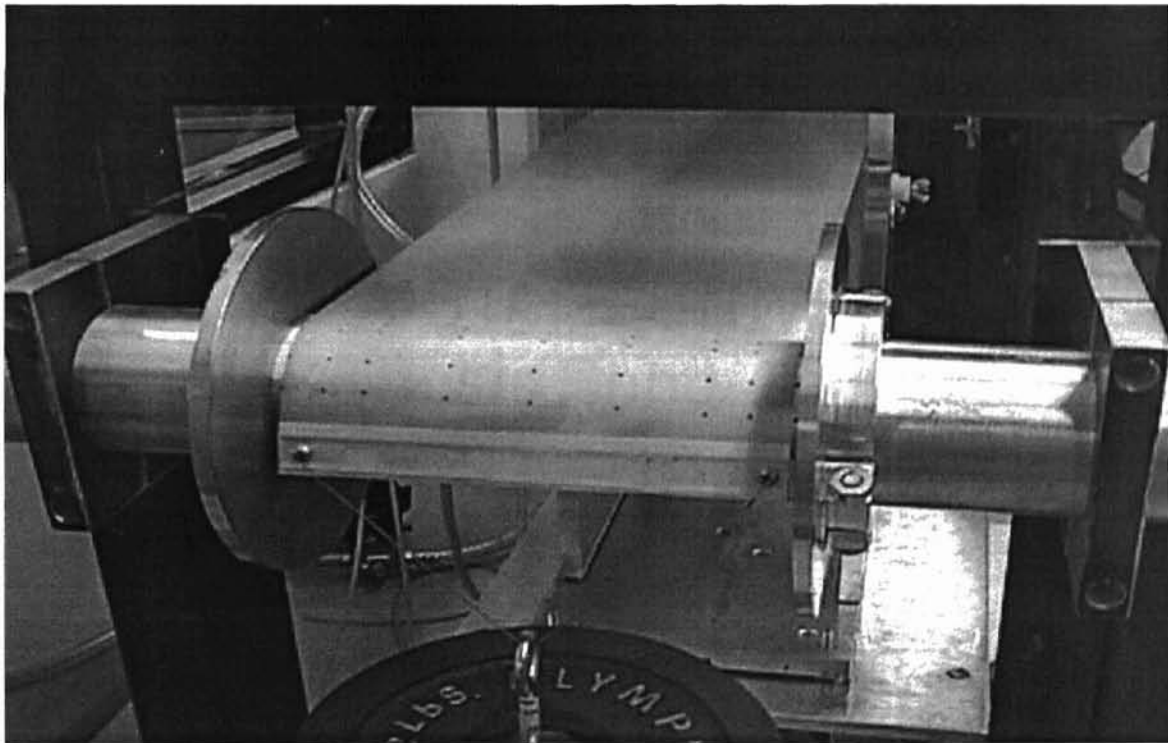
Figure 8. Non-contact support of the flexible web
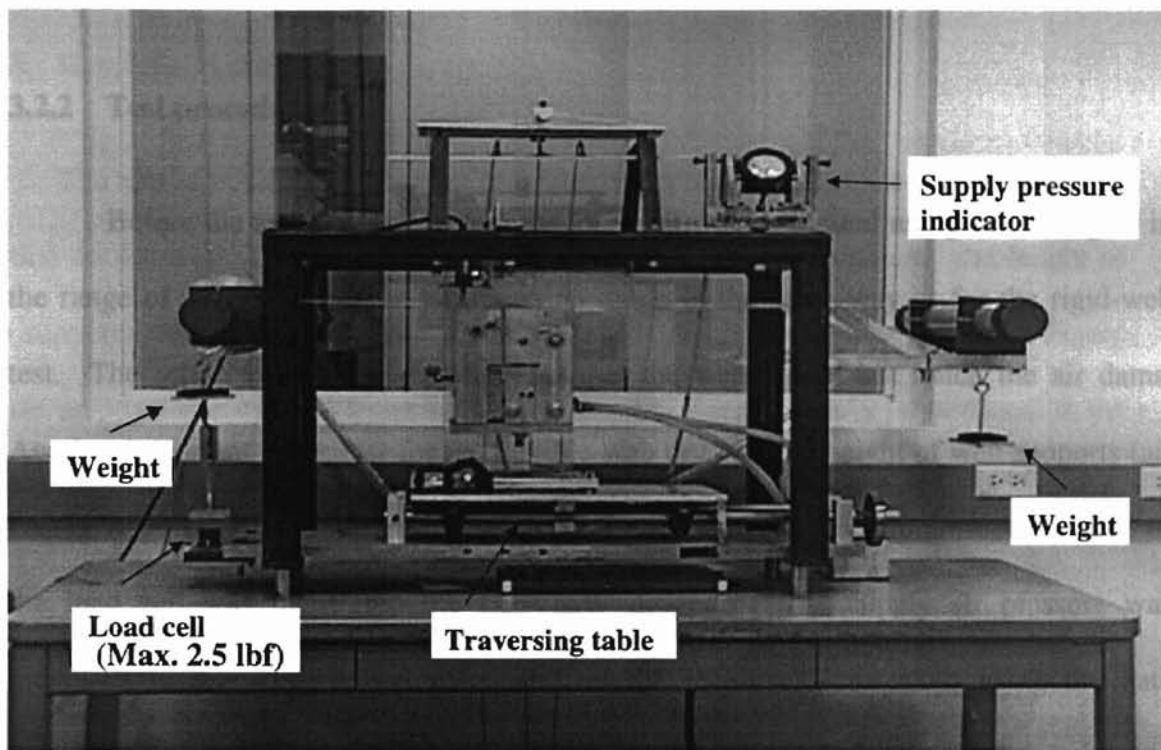
Figure 9. Side view of the flexible-web test setup
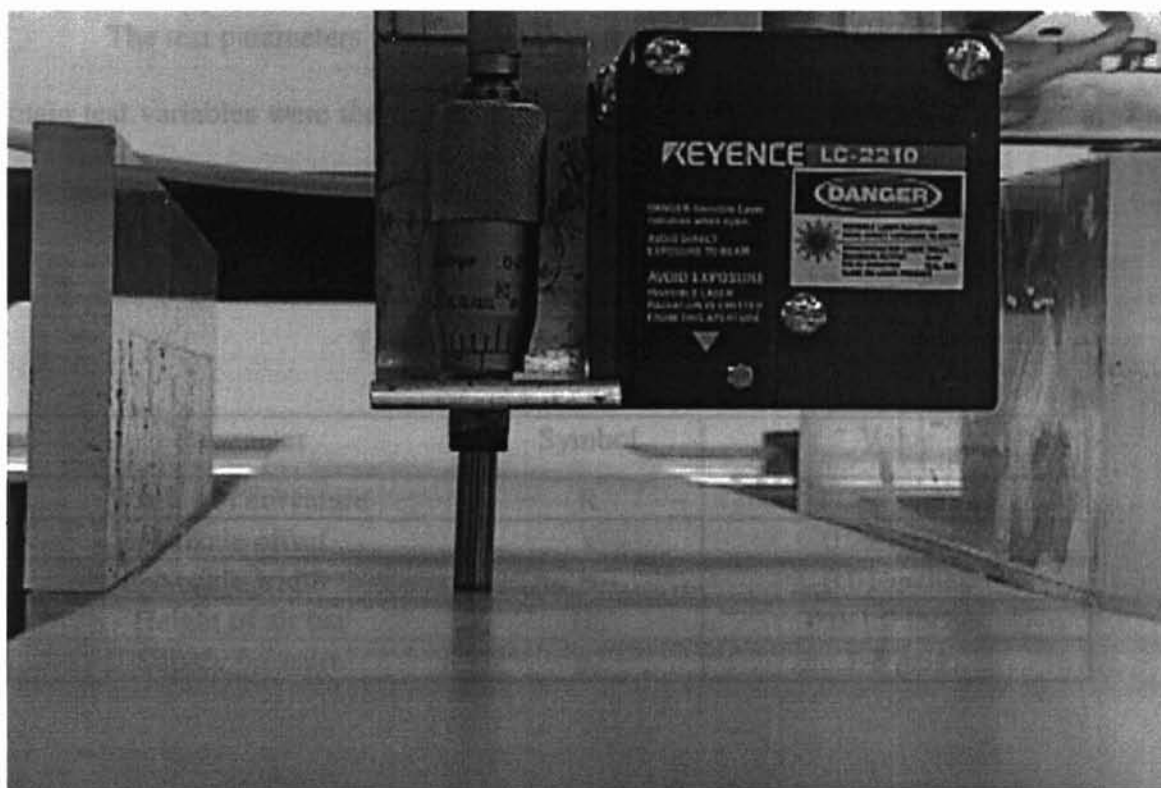
Figure 10. Micrometer used for measuring web deflections

3.2.2 Test procedure

Before the test was conducted, the load cell was calibrated using dead weights in the range of 0.0 to 0.25 lbf in compression mode in the same way as for the rigid-web test. The setup was aligned carefully so that the web would not touch the air dams. Another important parameter for the flexible-web test was the height of web supports (air bars). After all the parameters were adjusted and checked, the zero correction value of the load cell was input into the LabVIEW program. The supply air pressure was increased to a predetermined value and all the readings were taken using the data acquisition system. At the same time, the out-of-plane deflections of the web were measured using the micrometer.

The test parameters were almost the same as for the stationary rigid-web test. The main test variables were the supply air pressure, the height of air bars, and tension. The test conditions are tabulated in Table 3.

Table 3. Flexible-web test conditions

Parameter	Symbol	Value
Radius of curvature	R	11/64 inches
Nozzle offset	s	0.22 inches
Nozzle width	b	0.01 inches
Height of air bar	H_0	0.0-1.0 inches
Supply pressure	p_o	1-3 psig

3.2.3 Results and discussion

The aim of this second phase of the experiment was to determine the aerodynamic traction on the web. Effects of applied web tension, supply air pressure, and height of web supports were studied. In nearly all tested cases, including the case shown in Figure 11, the aerodynamic traction generated by the air jet is almost linearly proportional to the supply air pressure.

$$R = 11/64"$$
$$s = 0.22"$$
$$b = 0.01"$$
$$H_o = 0.25"$$
$$T = 0.417 \ lbf/in$$
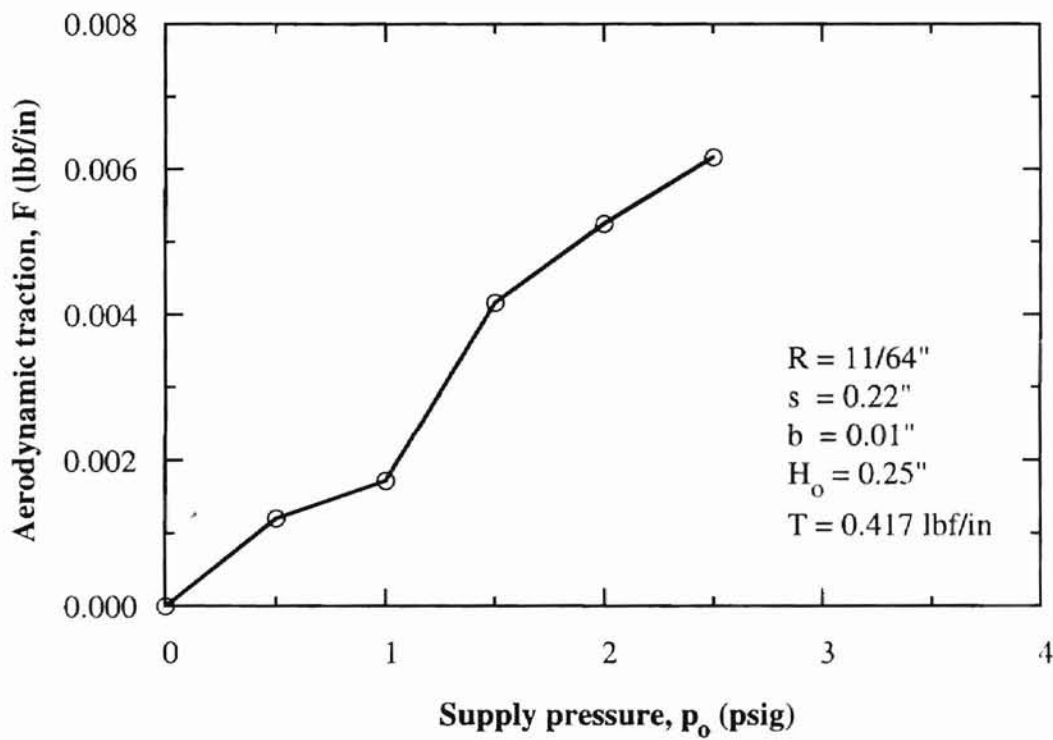
Figure 11. Measured aerodynamic traction on flexible web

Effect of support height on the aerodynamic traction

The traction caused by the air jet on the flexible web was measured for various values of heights of the supports including 0.0, 0.25, 0.50, and 1.0 inches.

The traction for $H_o = 0.00"$ is smaller than that for any other value of H_o; it seems that the traction is not strongly dependent on the support height when $H_o \geq 0.25"$ (Figure 12). The measured aerodynamic traction of the air jet is in the range of 20 - 30 percent of the supply pressure multiplied by the width of the air jet, $F/p_ob = 0.2 - 0.3$, in most test conditions except for when $H_o = 0"$ (Figure 13). This relationship needs to be confirmed by repeating the tests for various values of the nozzle width, b. The traction for other web tensions seems to have no significant relationship with the height of web supports.
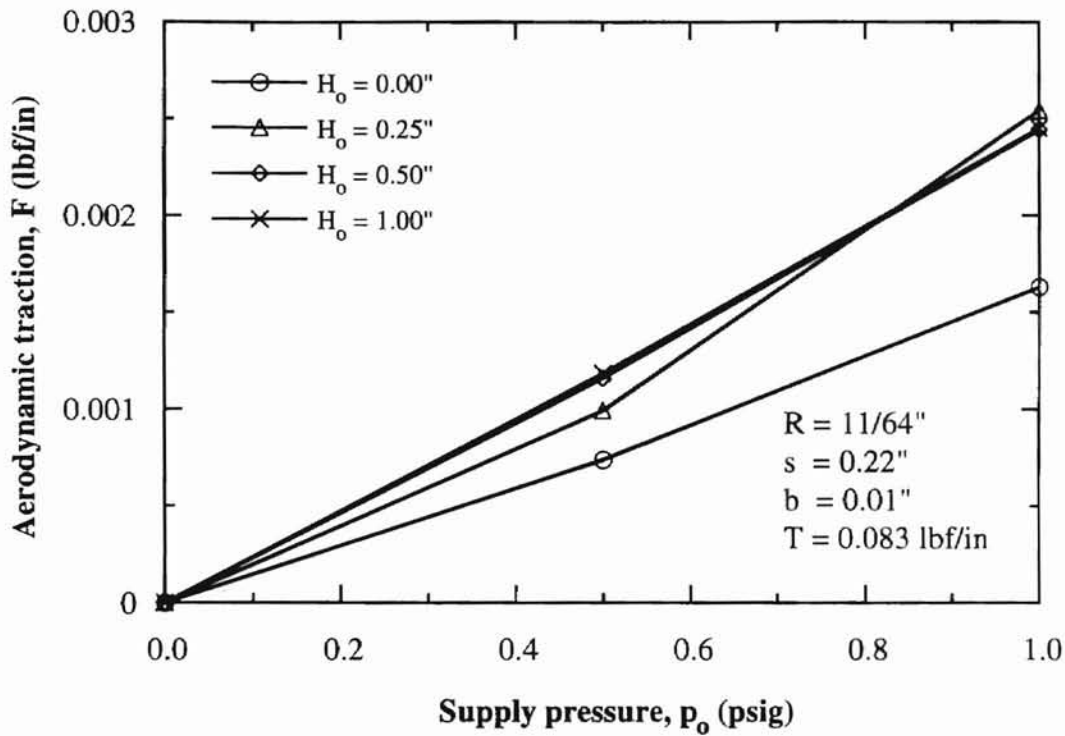
Figure 12. Effects of supply pressure and floatation height on traction (T = 0.083 lbf/in)
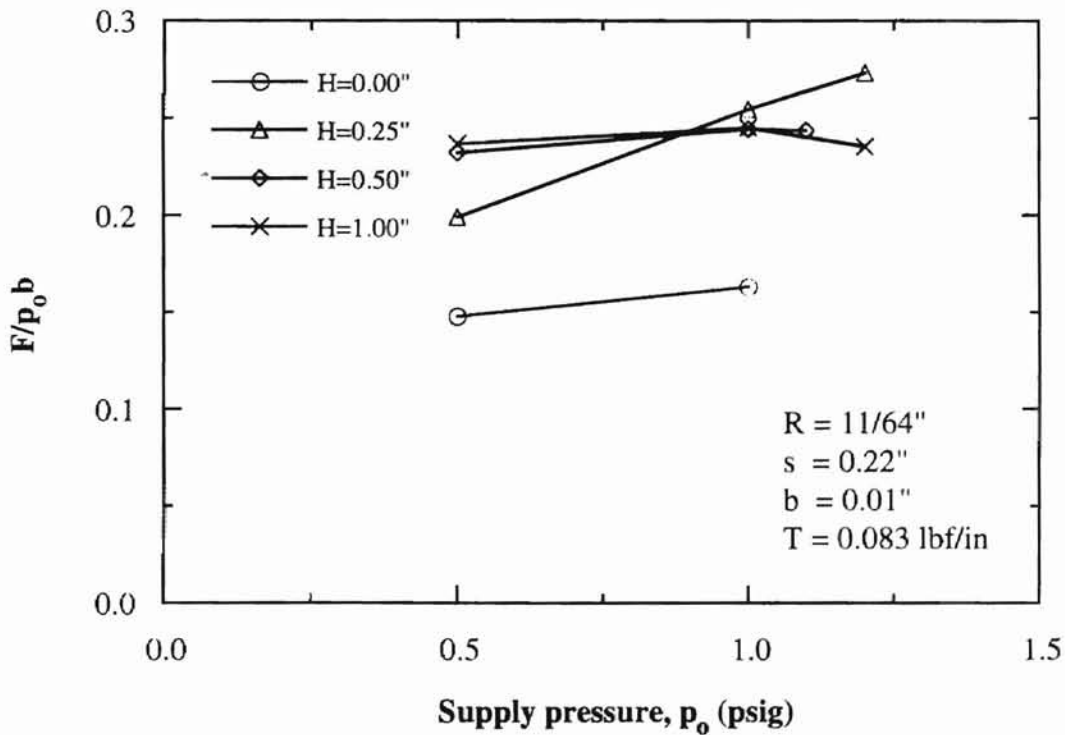
Figure 13. Effects of supply pressure and floatation height on non-dimensional traction (T = 0.083 lbf/in)
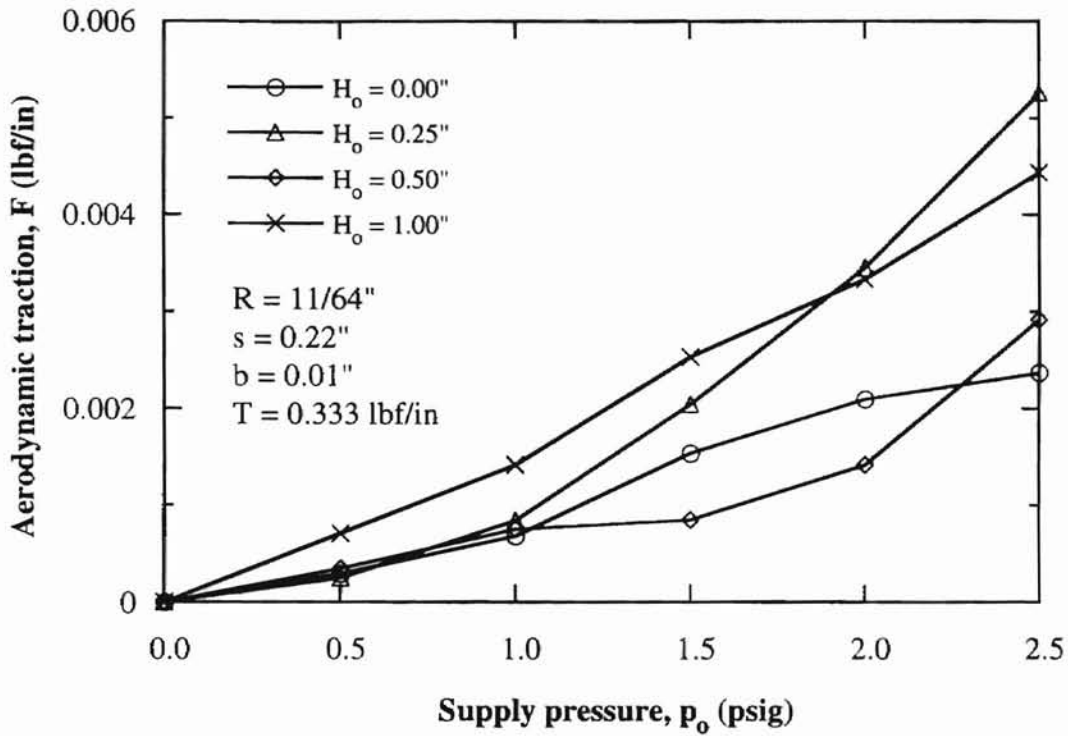
Figure 14. Effects of supply pressure and floatation height on traction (T = 0.333 lbf/in)
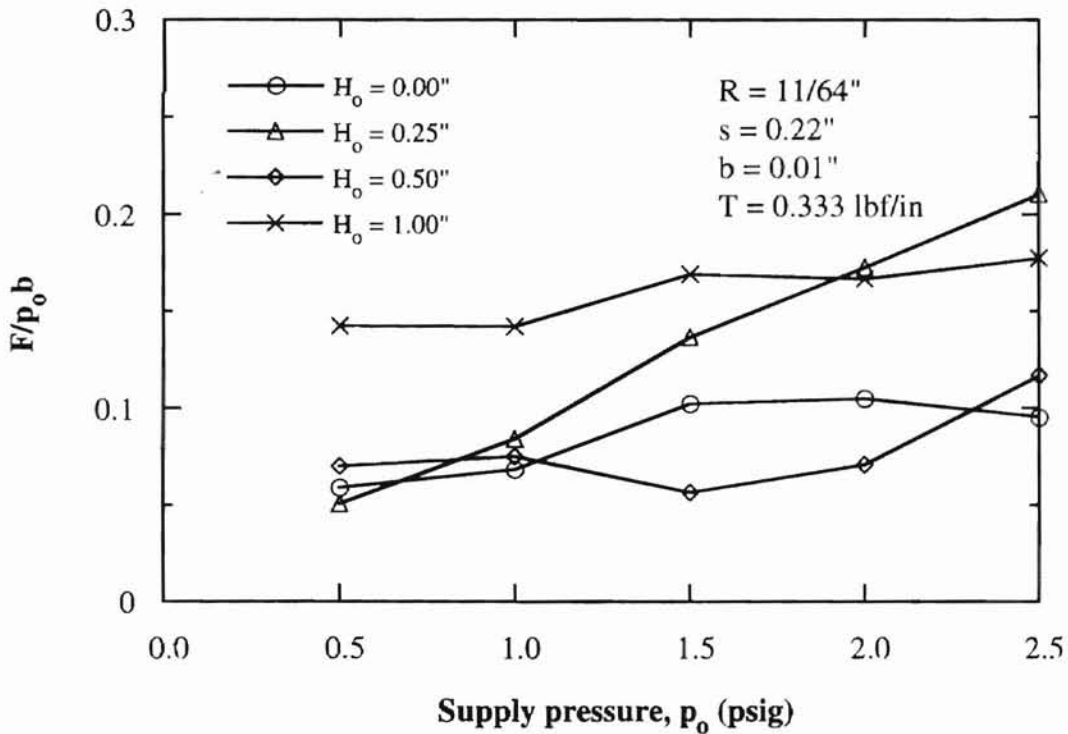
Figure 15. Effects of supply pressure and floatation height on non-dimensional traction (T = 0.333 lbf/in)

24
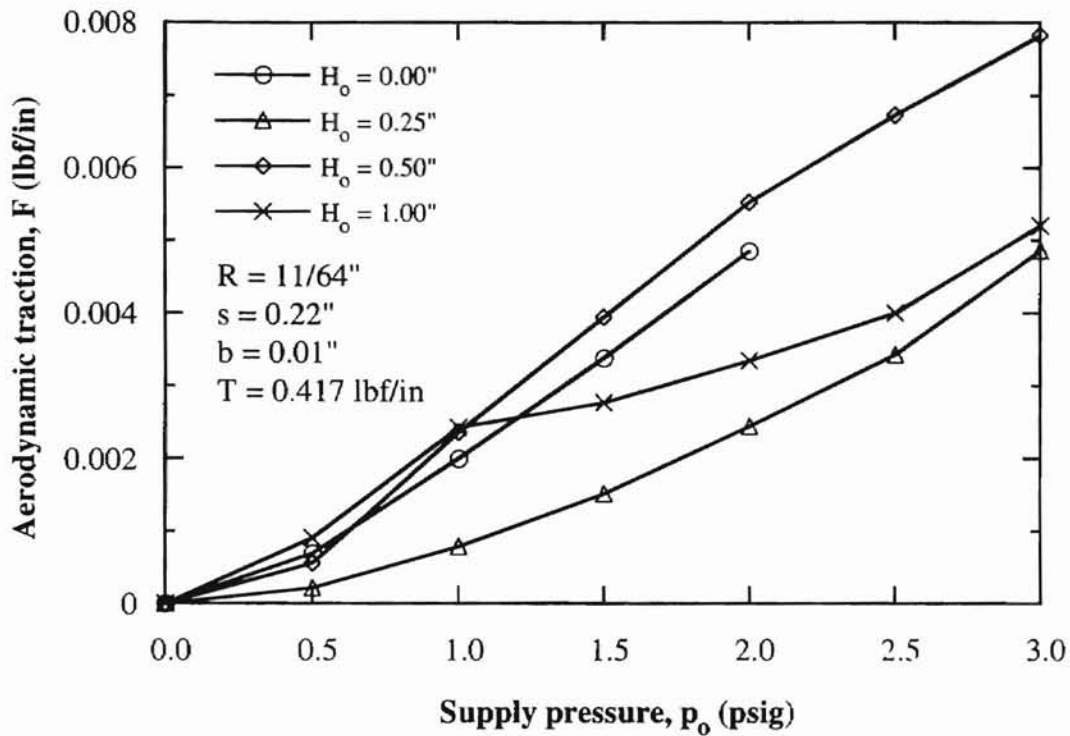
Figure 16. Effects of supply pressure and floatation height on traction (T = 0.417 lbf/in)
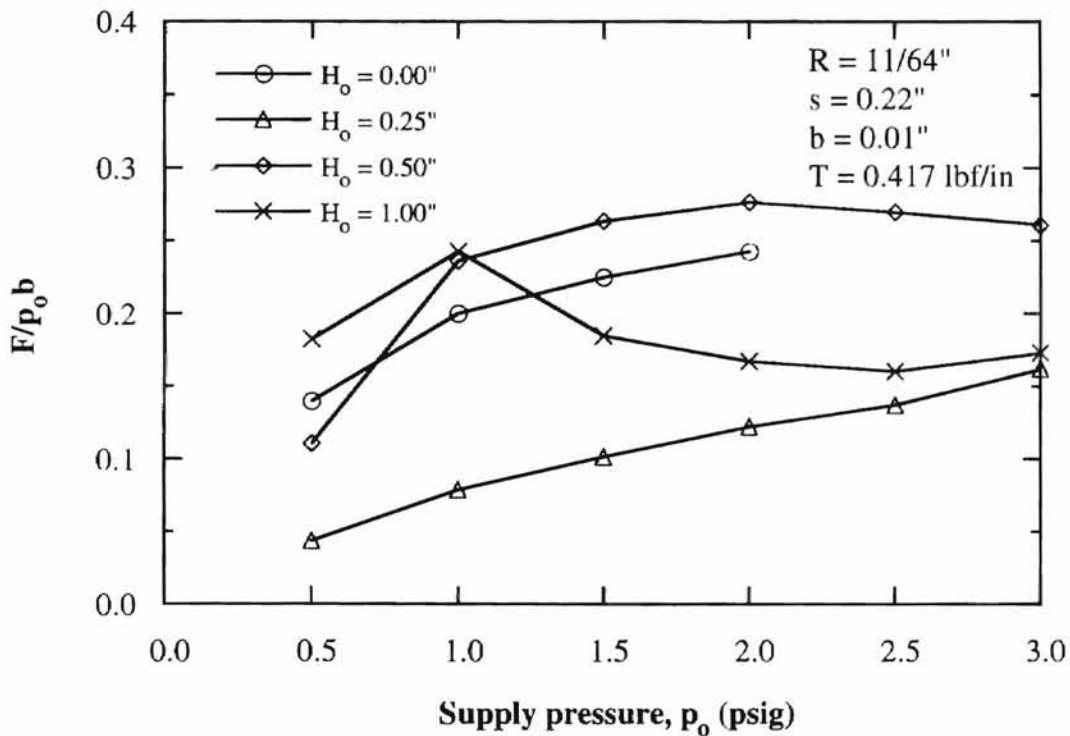
Figure 17. Effects of supply pressure and floatation height on non-dimensional traction (T = 0.417 lbf/in)

Effects of tension on the aerodynamic traction

Figure 18 through Figure 25 show the effects of web tension on the aerodynamic traction for various values of H_o. Note that H_o is the vertical distance between the web supports and the nozzle surface, or the distance between the flexible web and the nozzle surface when the supply pressure is zero. When $H_o = 0.00"$ (when the web supports are at the same level as the nozzle surface), web tension seems to affect the traction significantly; the traction for higher tension ($T = 0.417$ lbf/in) is larger than that for lower tension ($T = 0.333$ lbf/in). However, it is necessary to repeat the tests for many different values of tensions to determine its effects. When $H_o \geq 0.25"$, the effects of tension are not so significant as for $H_o = 0.00"$. The non-dimensional traction of the air jet on the web is in the range of 10 - 30 percent of the supply pressure multiplied by the width of the air jet, $F/p_ob = 0.1 - 0.3$, in most test conditions. This relationship needs to be confirmed through tests for different values of b.
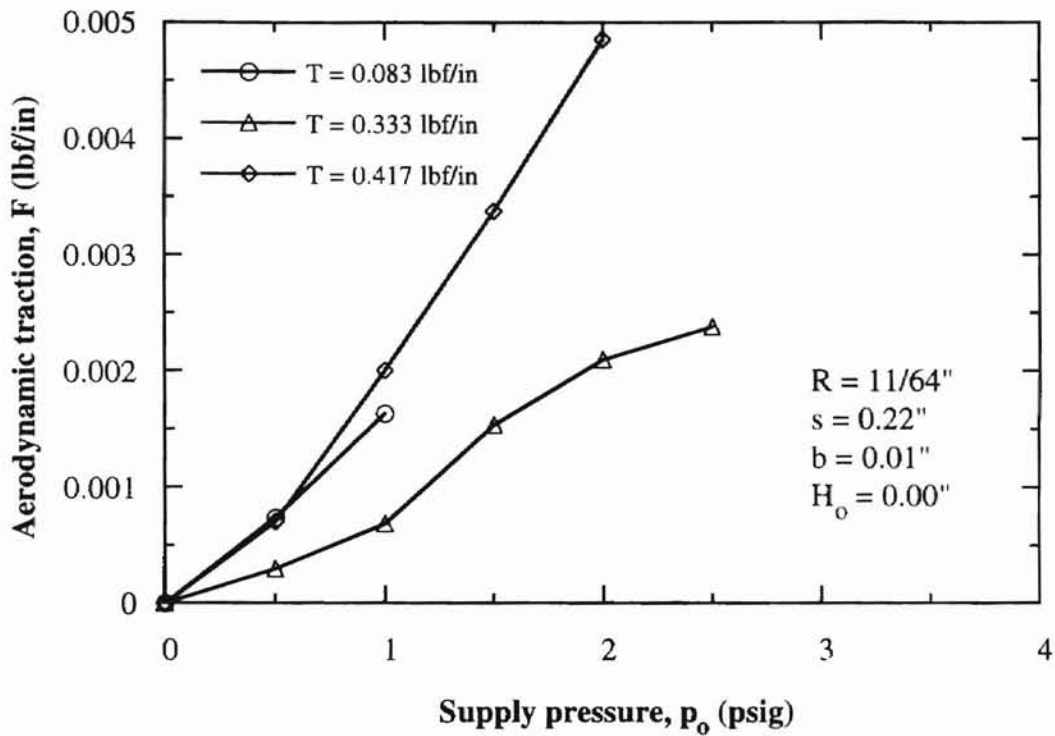
Figure 18. Effects of supply pressure and tension on traction ($H_o = 0.00$ in)
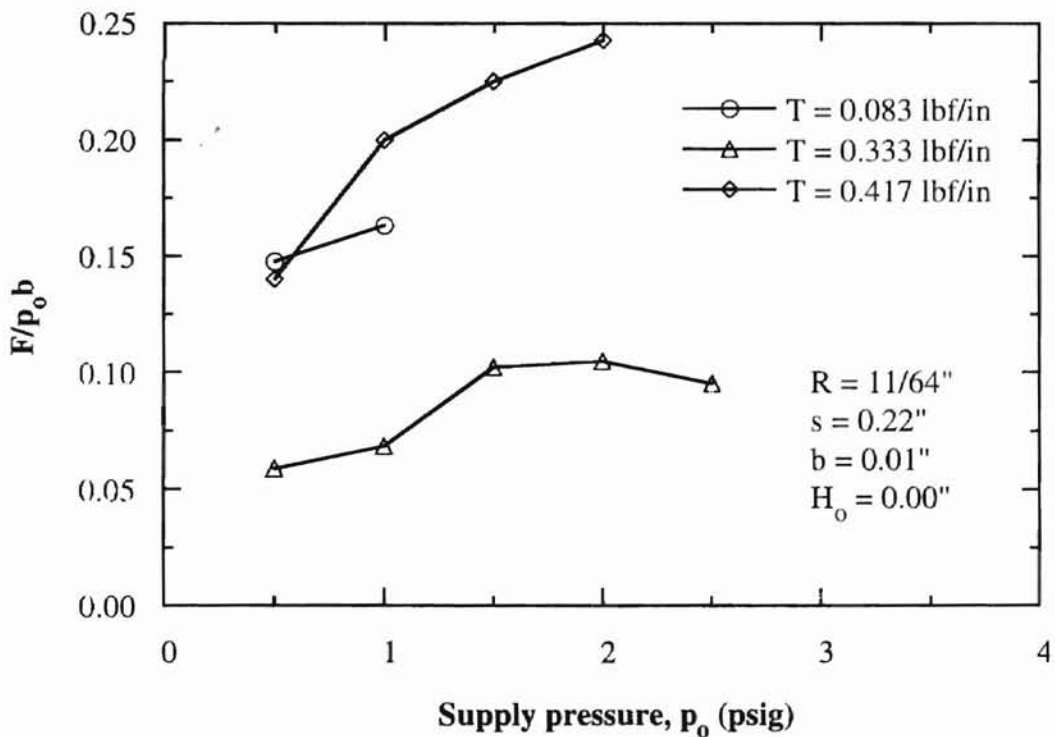
Figure 19. Effects of supply pressure and tension on non-dimensional traction ($H_o = 0.00$ in)

27
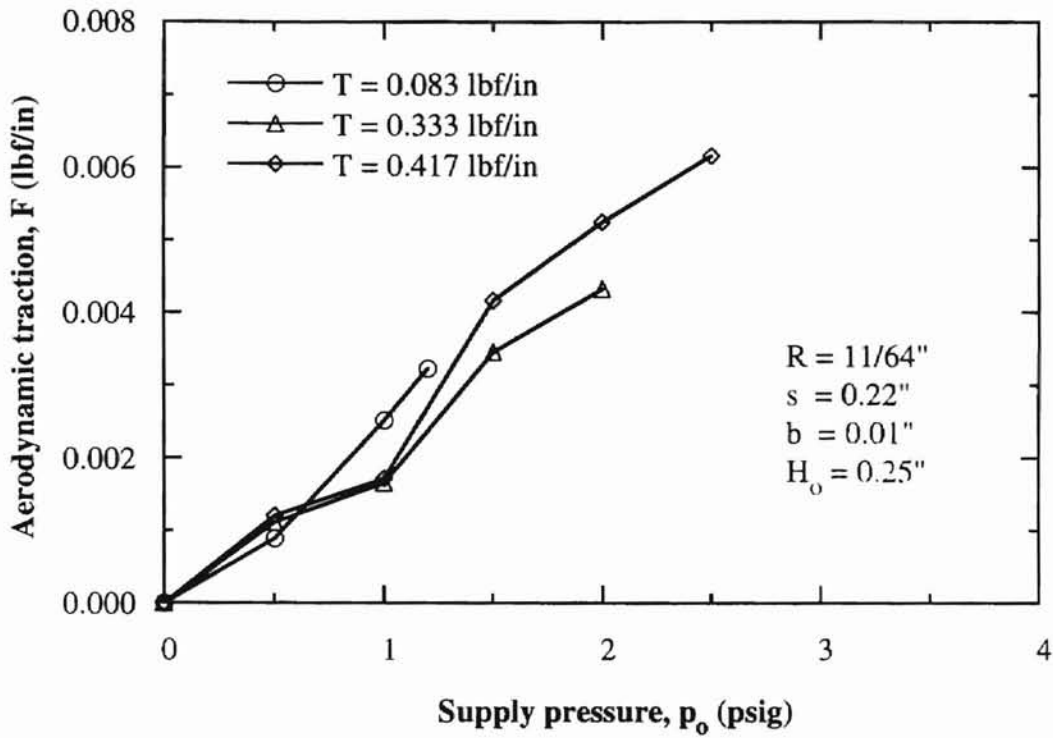
Figure 20. Effects of supply pressure and tension on traction (H_o = 0.25 in)
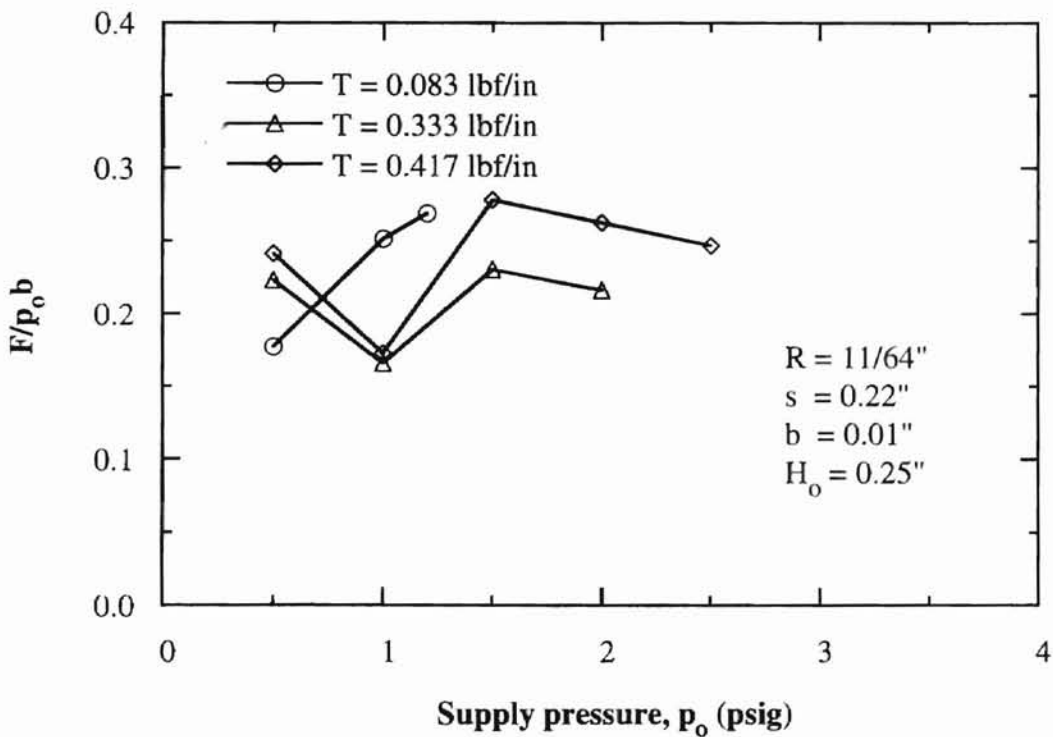
Figure 21. Effects of supply pressure and tension on non-dimensional traction (H_o = 0.25 in)

28
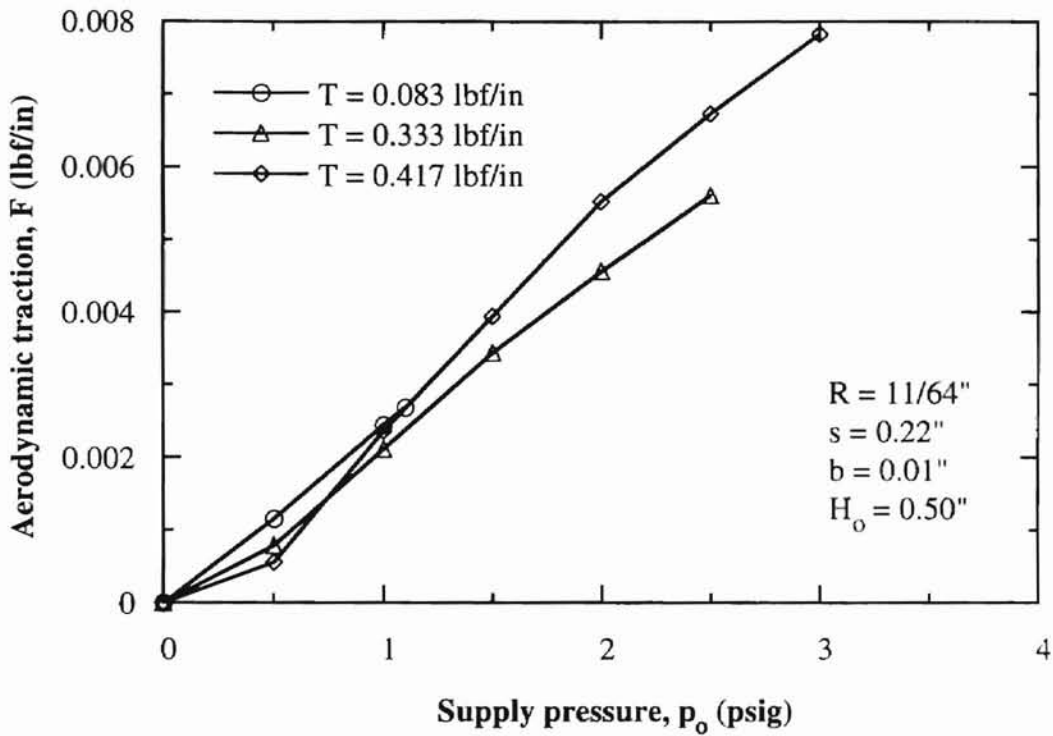
Figure 22. Effects of supply pressure and tension on traction ($H_o = 0.50$ in)
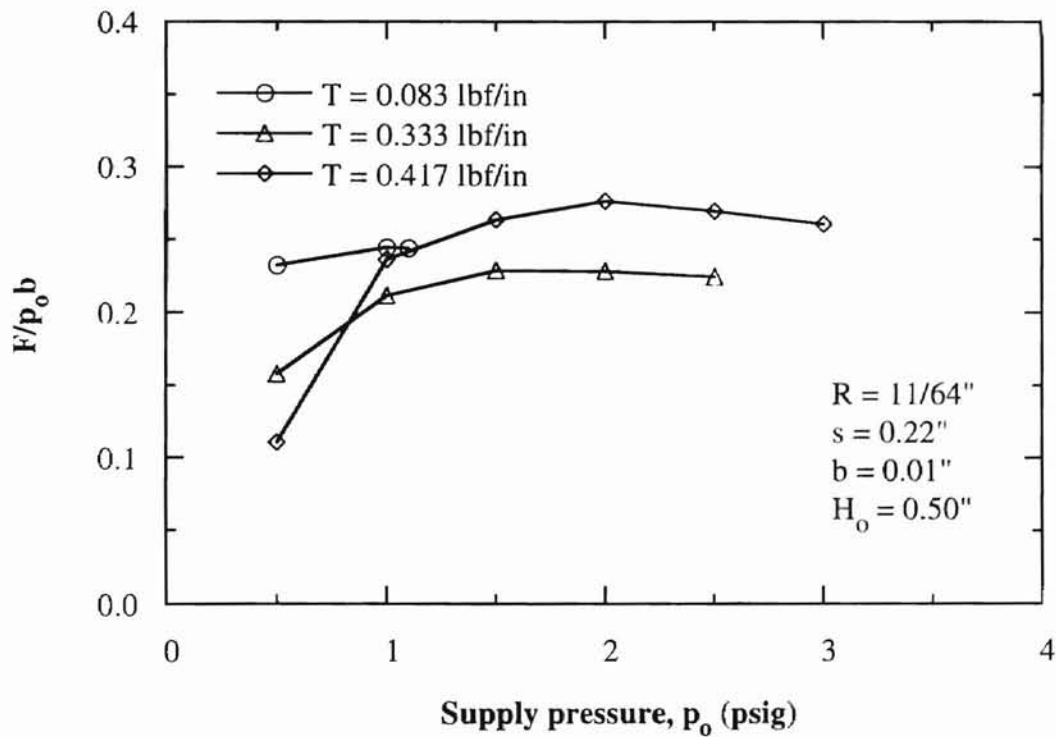
Figure 23. Effects of supply pressure and tension on non-dimensional traction ($H_o = 0.50$ in)
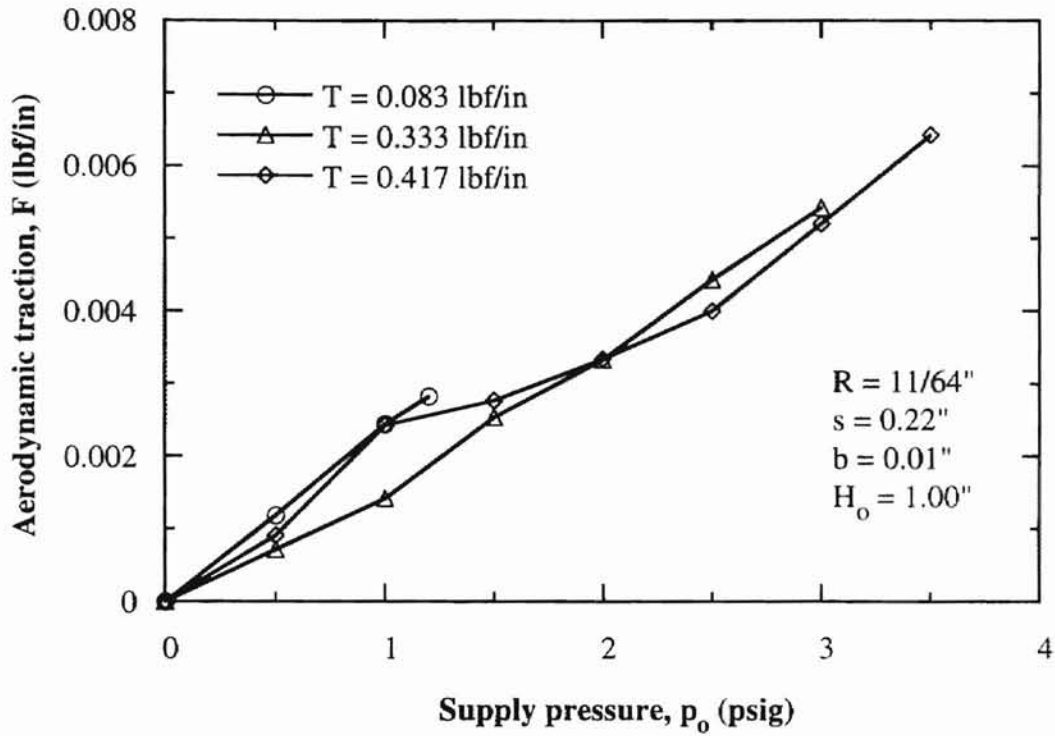
Figure 24. Effects of supply pressure and tension on traction (H_o = 1.00 in)
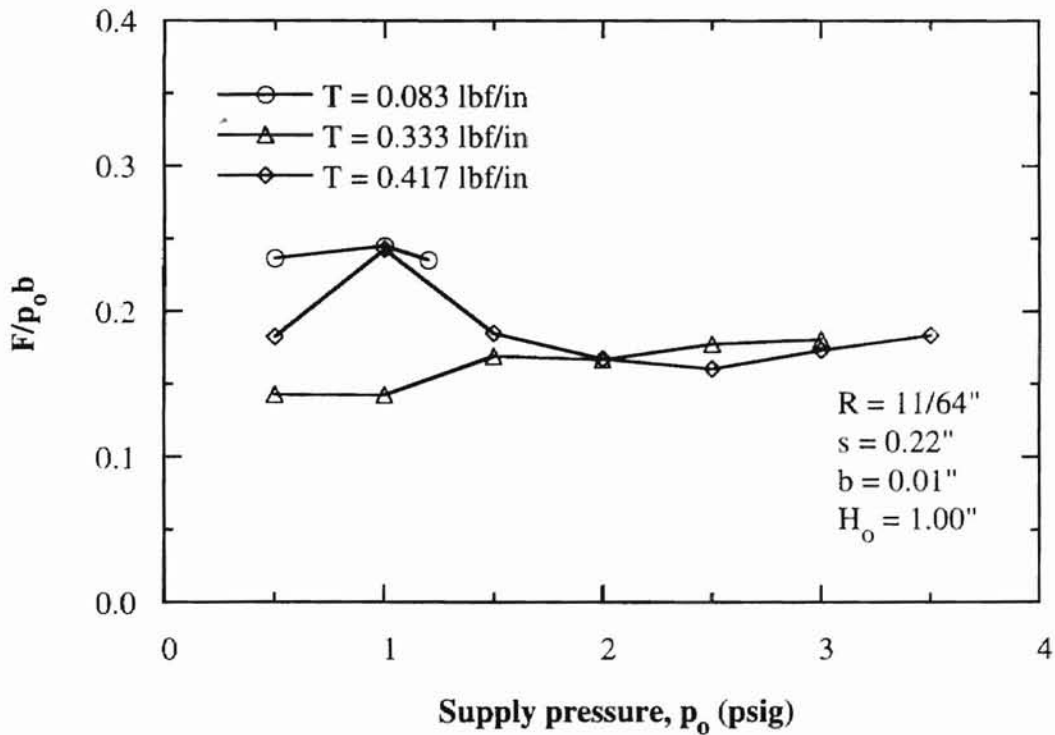
Figure 25. Effects of supply pressure and tension on non-dimensional traction (H_o = 1.00 in)

Repetition of tests

Because of excessive scatter of the experimental data, the tests for measuring the aerodynamic traction on a flexible web were repeated many times for $H_o = 0.25"$. Figure 26 through Figure 35 show the scatter of the experimental data and an average value of the non-dimensional traction (F/p_ob) at each condition. The scatter of the data becomes more excessive with the increase of web tension. It was discovered that the traction (drag force per unit width of web) is in the range of $20 - 30$ percent of the supply air pressure multiplied by the width of the air jet, $F/p_ob = 0.2 - 0.3$, in most test conditions. The main test variables were the air pressure in the nozzle (p_o), and web tension (T); other parameters such as the location of the web supports (H_o), the width of the nozzle (b), and the radius of curvature of the nozzle (R) were kept constant. The effects of the web tension and pressure in the nozzle on the traction and non-dimensional traction are shown in Figure 36 and Figure 37.
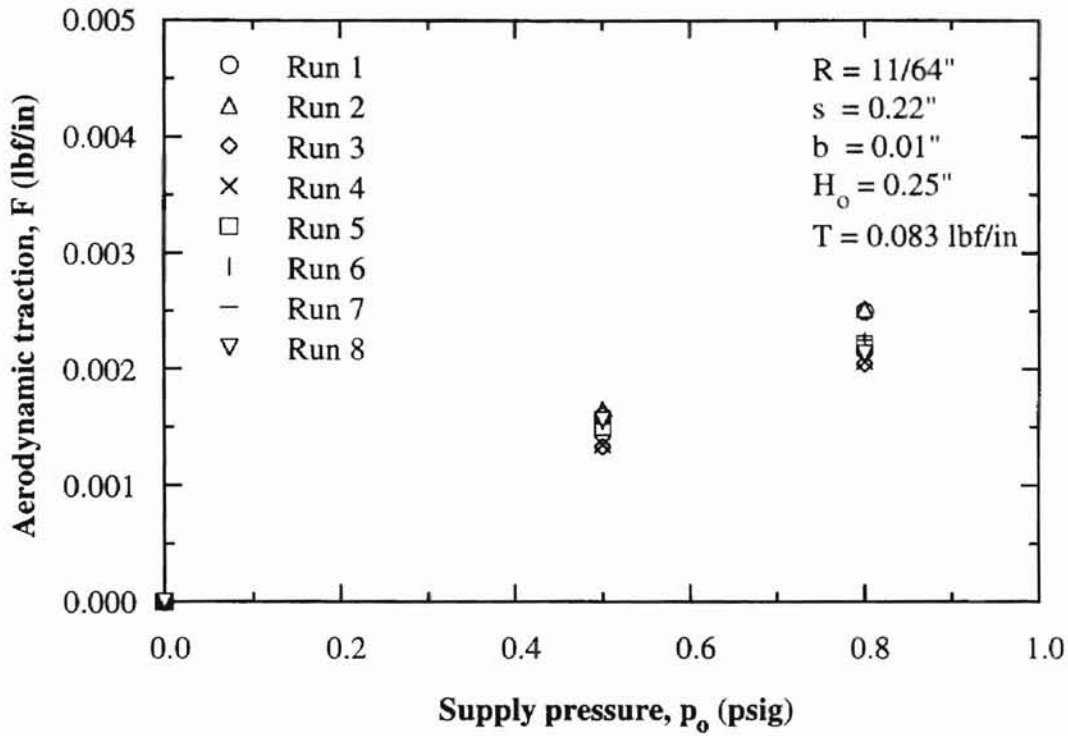
Figure 26. Effects of supply pressure on traction (T = 0.083 lbf/in)
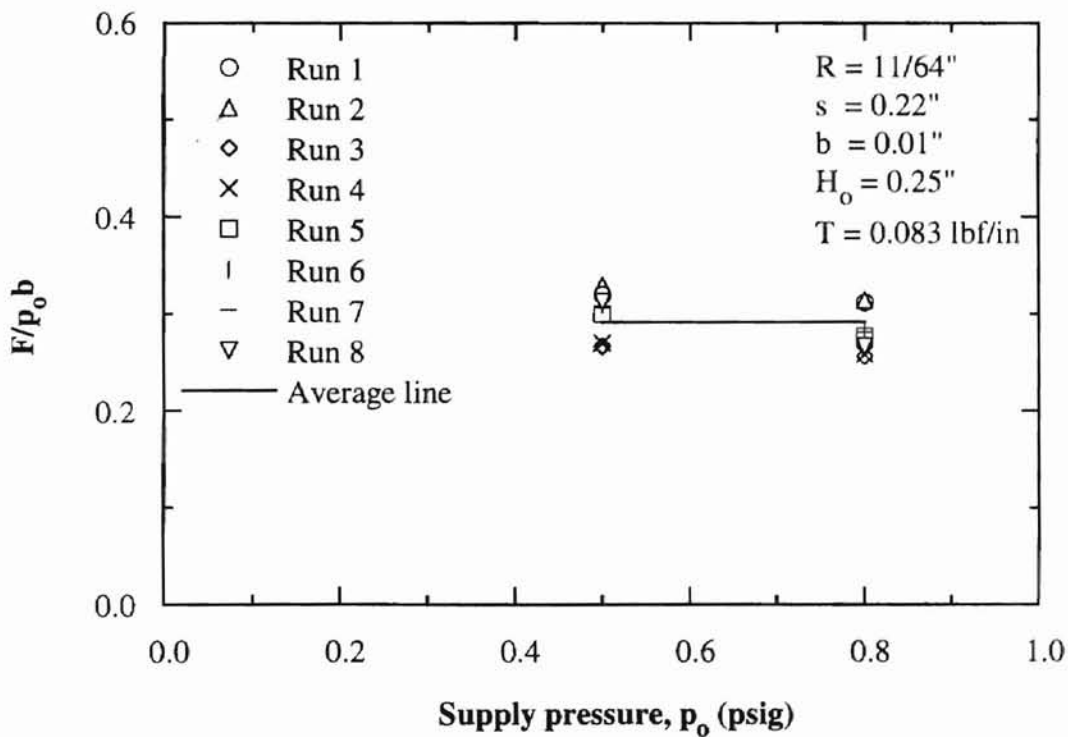
Figure 27. Effects of supply pressure on non-dimensional traction (T = 0.083 lbf/in)

Aerodynamic traction, F (lbf/in)

0.005

0.004

0.003

0.002

0.001

0.000

	Run 1
	Run 2
	Run 3
	Run 4
	Run 5
	Run 6

R = 11/64"
s = 0.22"
b = 0.01"
H_o = 0.25"
T = 0.167 lbf/in

0.0   0.2   0.4   0.6   0.8   1.0

Supply pressure, p_o (psig)
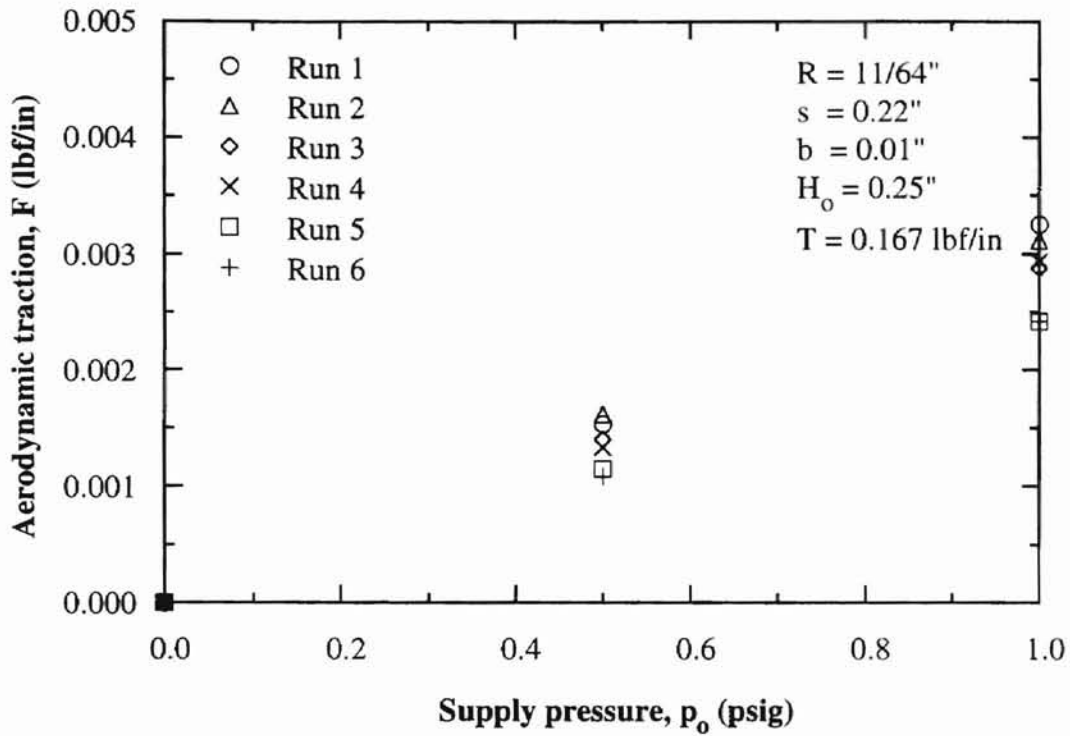
Figure 28. Effects of supply pressure on traction (T = 0.167 lbf/in)

$F/p_o b$

0.5

0.4

0.3

0.2

0.1

0.0

	Run 1
	Run 2
	Run 3
	Run 4
	Run 5
	Run 6
—	Average line

R = 11/64"
s = 0.22"
b = 0.01"
H_o = 0.25"
T = 0.167 lbf/in

0.0   0.2   0.4   0.6   0.8   1.0

Supply pressure, p_o (psig)
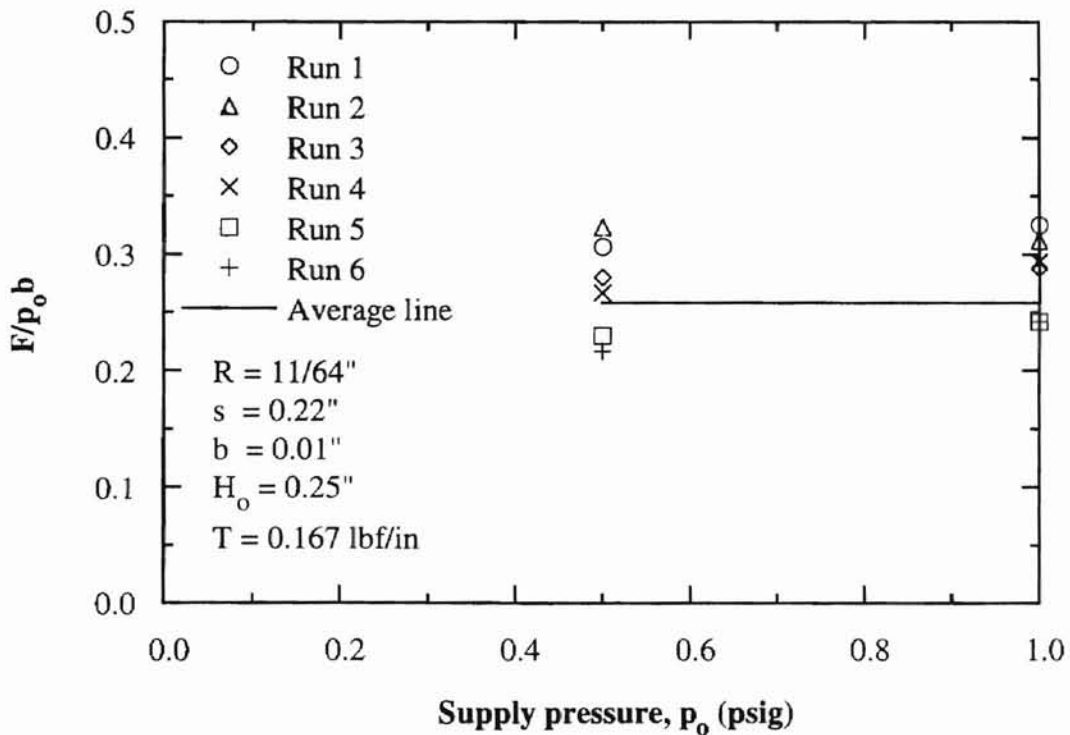
Figure 29. Effects of supply pressure on non-dimensional traction (T = 0.167 lbf/in)
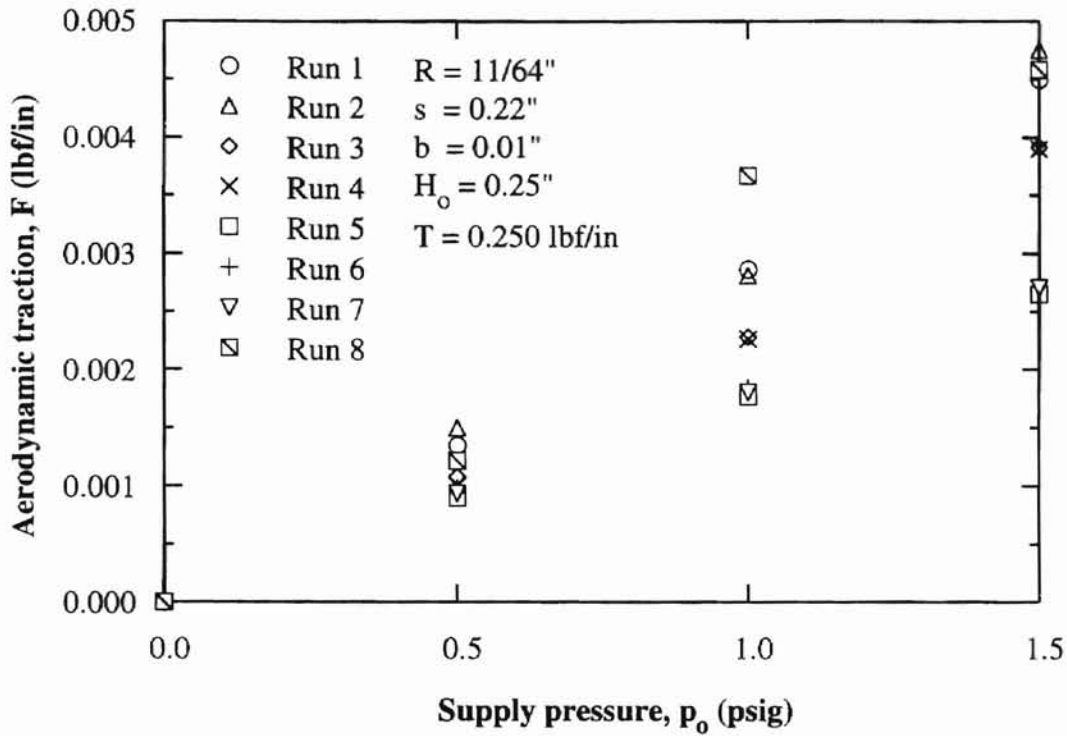
Figure 30. Effects of supply pressure on traction (T = 0.250 lbf/in)
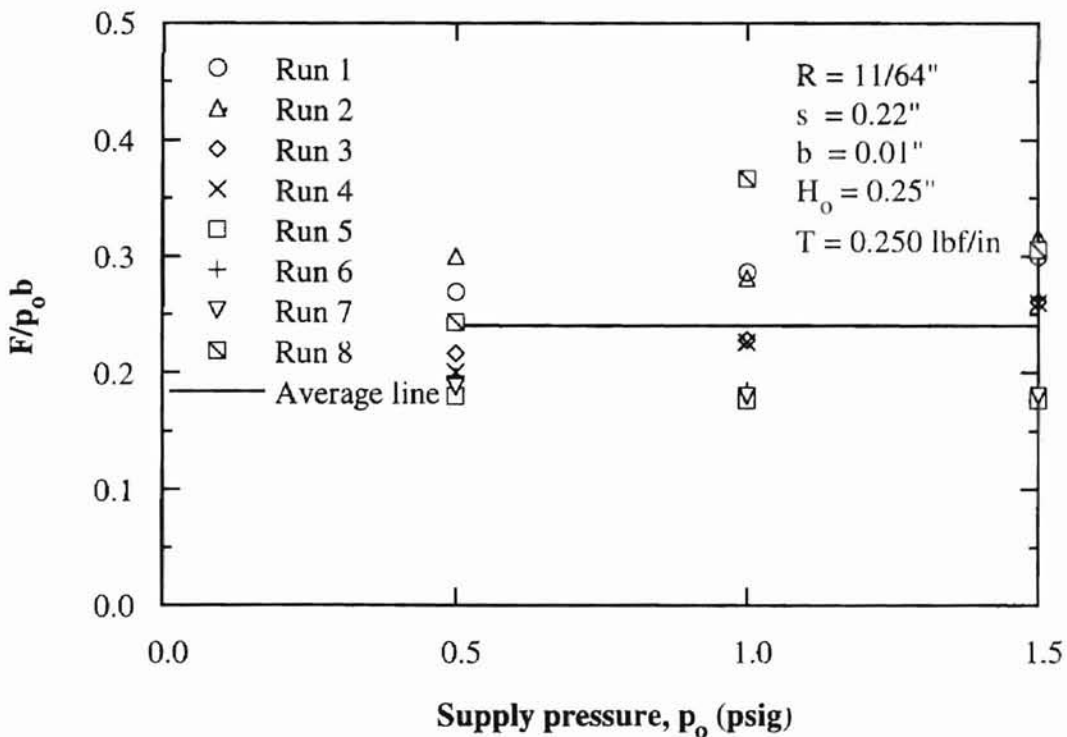
Figure 31. Effects of supply pressure on non-dimensional traction (T = 0.250 lbf/in)

34
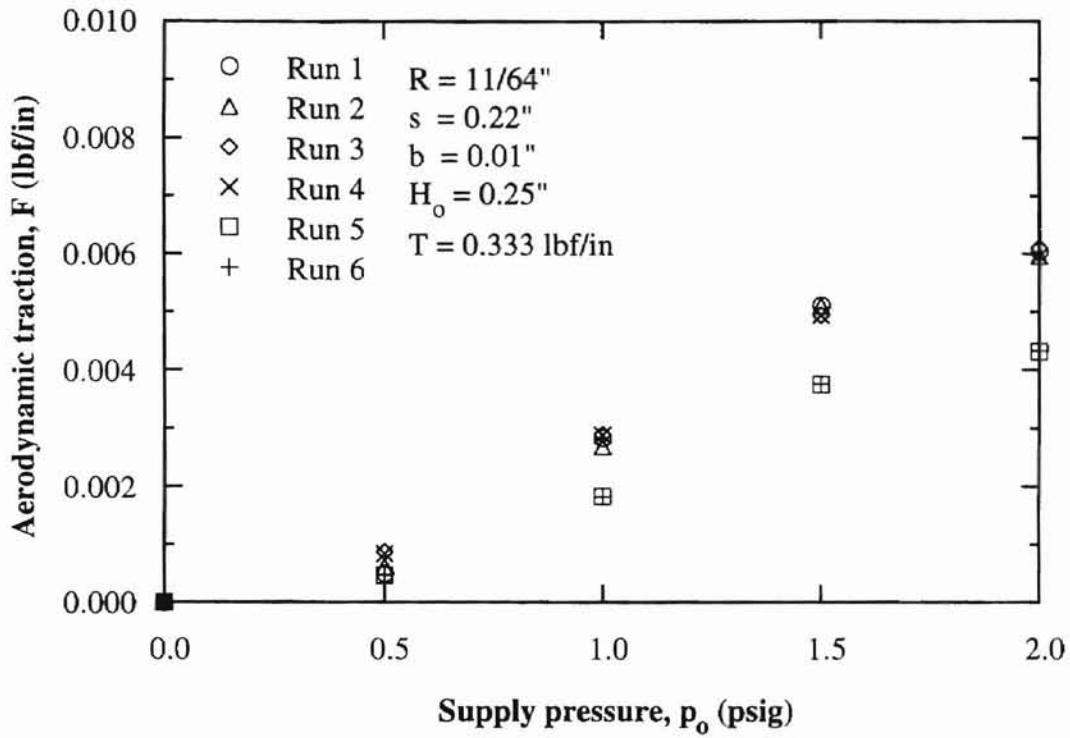
Figure 32. Effects of supply pressure on traction (T = 0.333 lbf/in)
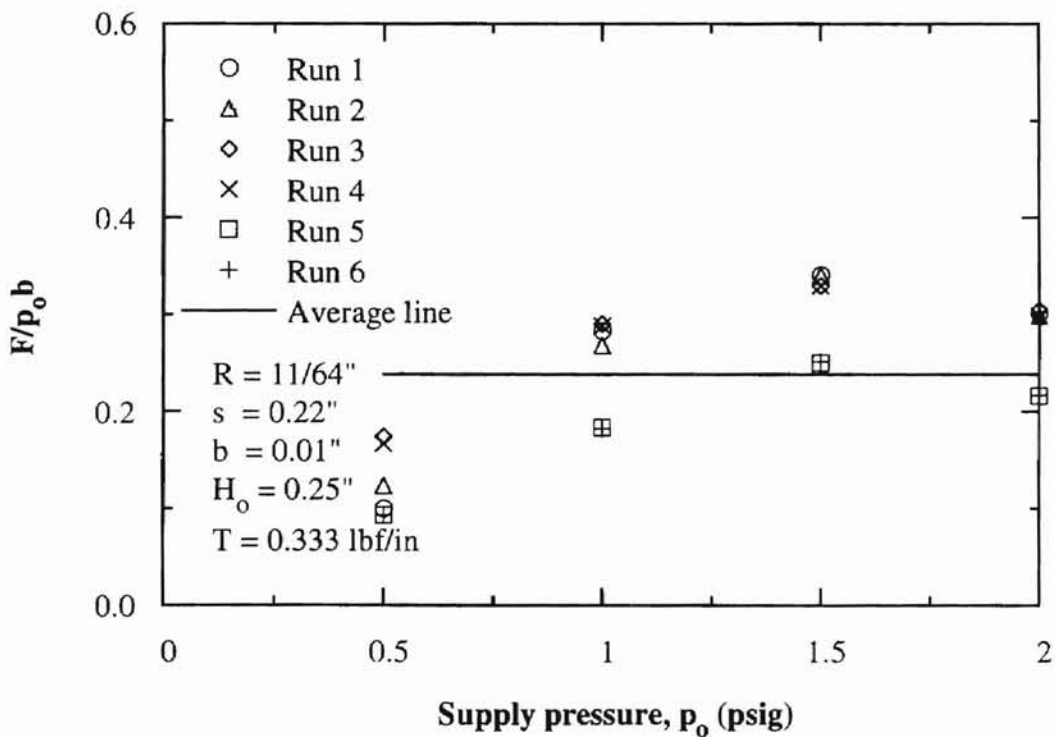
Figure 33. Effects of supply pressure on non-dimensional traction (T = 0.333 lbf/in)

35
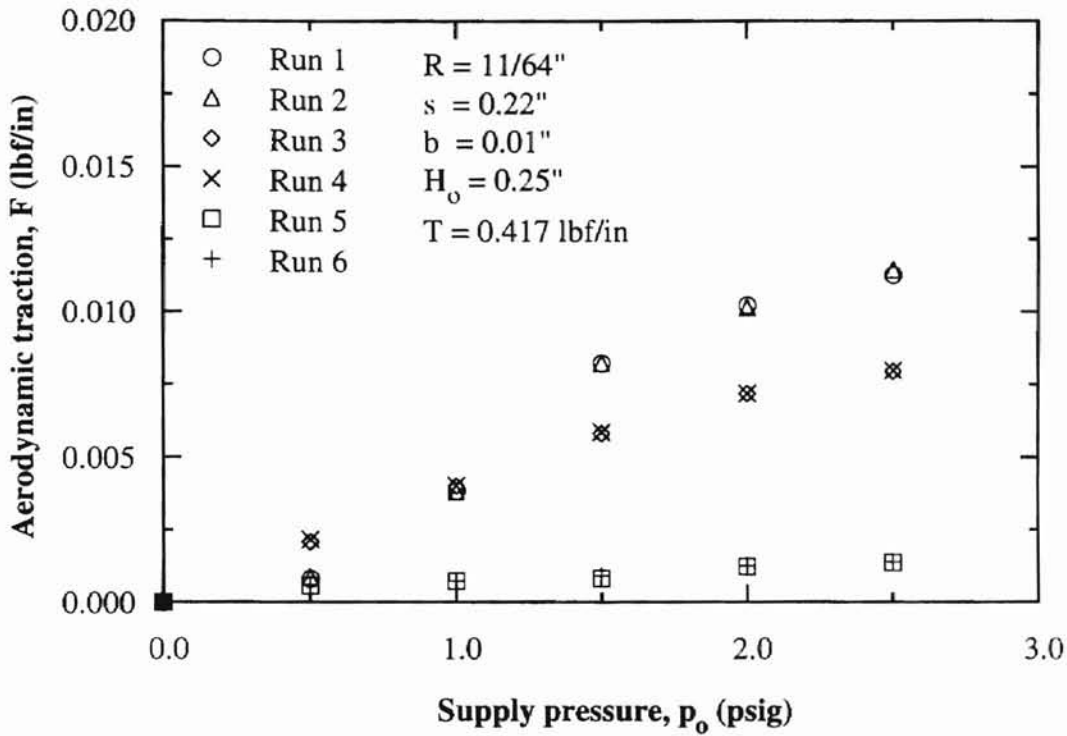
Figure 34. Effects of supply pressure on traction (T = 0.4178 lbf/in)
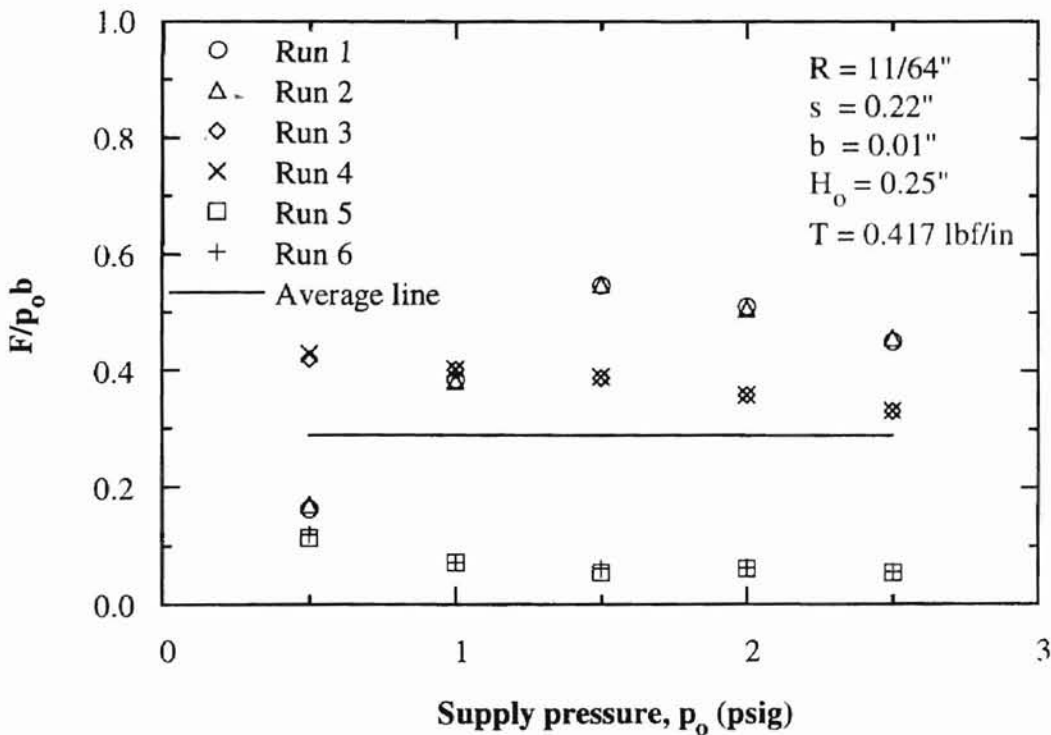
Figure 35. Effects of supply pressure on non-dimensional traction (T = 0.333 lbf/in)

36
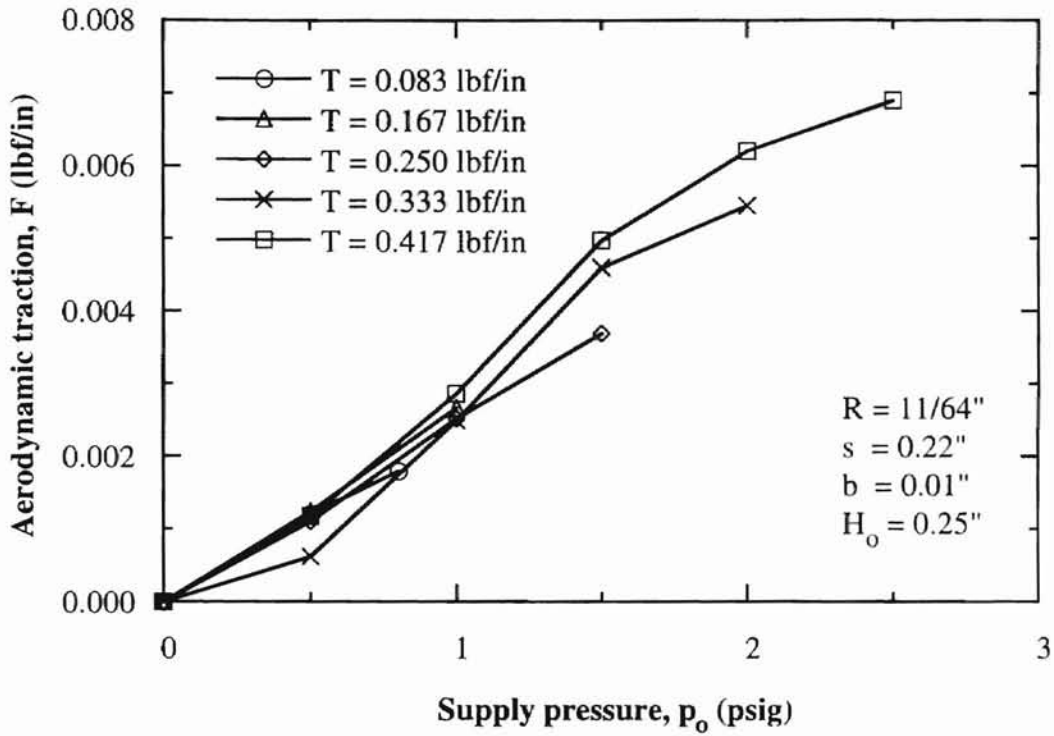
Figure 36. Effects of supply pressure and tension on traction (H_o = 0.25 in)
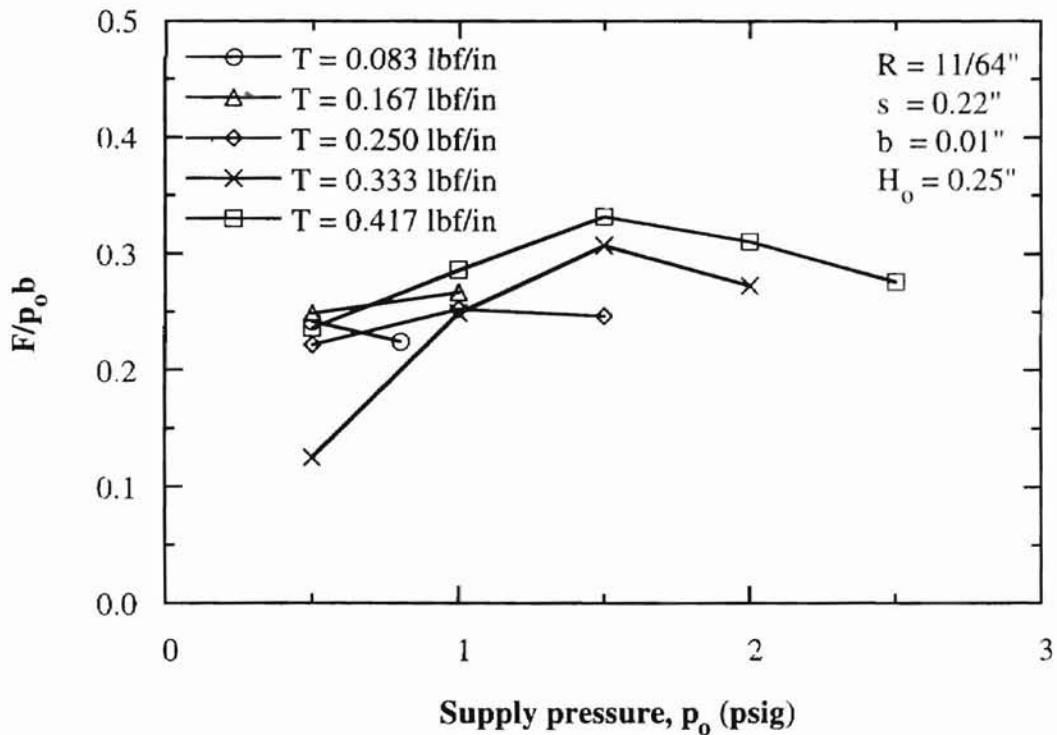
Figure 37. Effects of supply pressure and tension on non-dimensional traction (H_o = 0.25 in)

3.2.4 Uncertainty of measurements

The uncertainty of the traction measurement data for the flexible web is the same as for the rigid-web test because the same load cell was used for both series of experiments. The uncertainty of the micrometer reading was ± 0.001 inches.

CHAPTER IV

COMPUTATIONS

4.1 Using FLUENT/UNS

4.1.1 Considerations in using FLUENT/UNS

To obtain accurate and stable solutions using FLUENT/UNS, a few factors need to be considered. They include mesh type, skewness, discretization scheme, and turbulence model.

Quadrilateral/Hexahedral and Triangular/Tetrahedral meshes are available in FLUENT/UNS. In this study, the triangular unstructured grid was used, because this grid type is the best choice for the complex geometry near the nozzle region where the high velocity and pressure gradients are expected. This type of mesh can be easily varied to maintain a reasonable number of cells in the grid by using a triangular grid instead of the mesh with quadrilateral grids. The quality of mesh is determined by the skewness, which is defined as 1 minus the ratio of the actual cell size to the optimal cell size which is the size of an equilateral cell with the same circumradius. FLUENT/UNS manual states that a maximum skewness should be less than 0.7 for two-dimensional triangular grids. The skewness of the meshes used in this study was approximately 0.5, and the quality of meshes was considered reasonably good.

Numerical diffusion arises primarily due to truncation errors introduced by each

discrete grid containing fluid flow equations. The numerical diffusion is minimized when the flow is aligned with the grid. The unstructured triangular mesh may cause numerical diffusion because the flow is never aligned with the grid. FLUENT/UNS manual states that in order to reduce the effects of numerical diffusion on the solution, the second order discretization scheme is recommended for all the parameters of a solution when using an unstructured triangular grid. The truncation error in the second order scheme will be very low when this criterion is followed.

FLUENT/UNS offers several turbulence viscous models such as the Standard $\kappa - \varepsilon$ Model, the RNG $\kappa - \varepsilon$ (Renormalization Group) Model, and the Reynolds Stress Model including Non-equilibrium Wall Function. Among these turbulence viscous models, the Reynolds Stress Model was selected. The Reynolds Stress Model gives more accurate results for modeling of flow separation and attachment than any other models available in FLUENT/UNS. This model is recommended for an accurate analysis of turbulent flow near the wall region. It uses the Non-equilibrium Wall Function which is good in handling complex flows involving separation, reattachment, and impingement. Examples of such flows are wall-bounded turbulent jet flows, where the mean flow and turbulence are subjected to severe pressure gradients and change rapidly.

4.1.2 Procedure of computation

Calculations were done following the procedure shown below and in Figure 38.

Step 1: Create geometry model and grid.

Step 2: Specify the boundary conditions such as pressure inlet, pressure outlet, wall boundary.

Step 3: Choose the solver in FLUENT/UNS for two-dimensional dimensional or three-dimensional model.

Step 4: Read scheme file including material properties.

Step 5: Import the grid from Geomesh to UNS 2D for 2D case.

Step 6: Check and scale grid size and convert the units as modeled.

Step 7: Choose the model and equations to be used in solving the problem.

Step 8: Specify material properties.

Step 9: Specify boundary conditions.

Step 10: Set the value of convergence criterion.

Step 11: Initialize the computation domain.

Step 12: Perform calculations and obtain solutions.

Step 13: Examine the results.

Step 14: If necessary, refine the grid using Adaption and continue calculation.

Step 15: Export the FLUENT data.
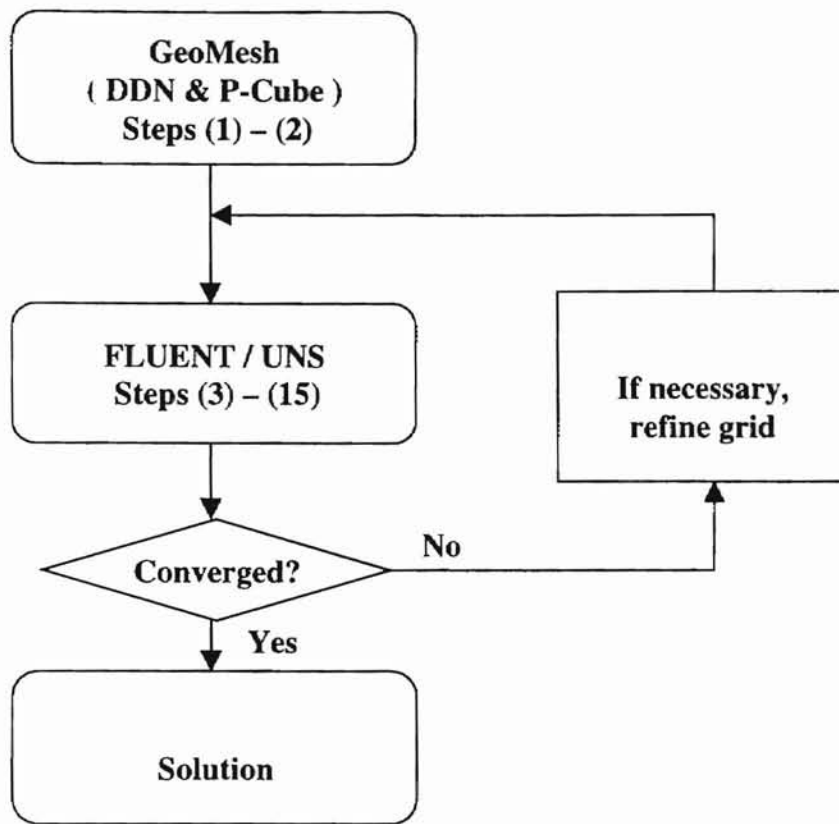
Figure 38. Flow chart of calculation steps

4.2 Coanda Air Jet and a Stationary Rigid Web

4.2.1 Description of the computational model

The computational model shown in Figure 39 simulates the experimental model schematically shown in Figure 40. Pressure outlet boundaries are the surfaces where the total pressure in constant, which is the atmospheric pressure in this study; There is no pressure gradient at the pressure boundaries. The right side pressure boundary was placed 80 inches from the slot nozzle, and the left side pressure boundary was placed 40 inches from the slot nozzle. These distances seem to be adequate.
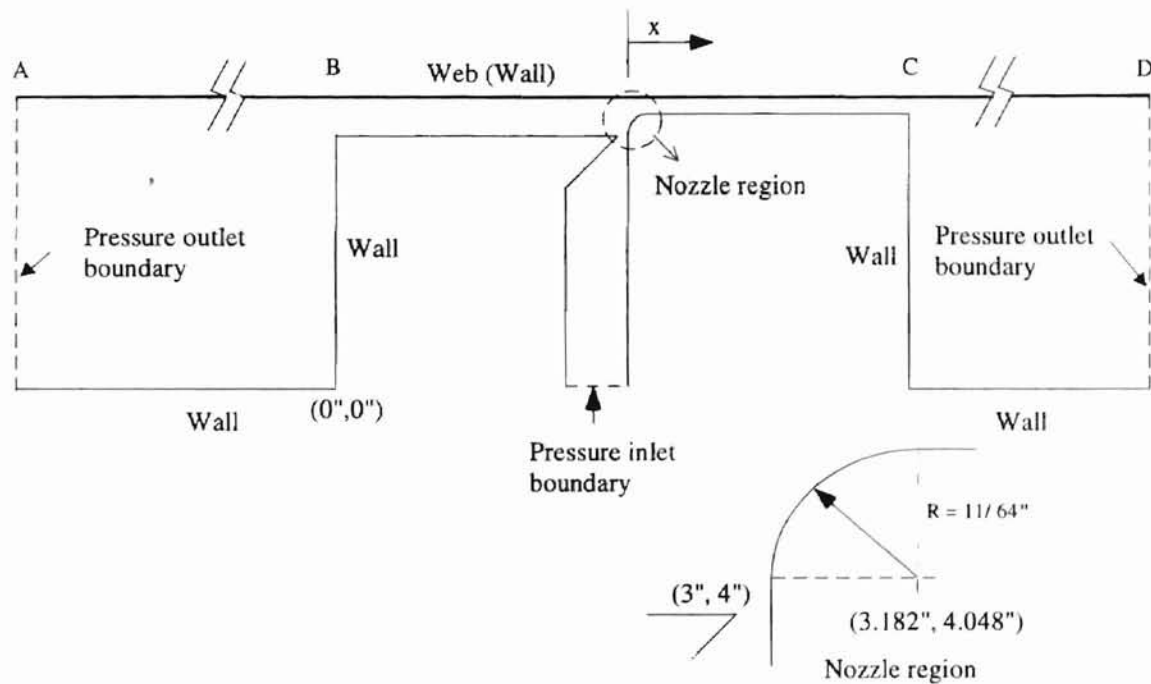
Figure 39. Computational model
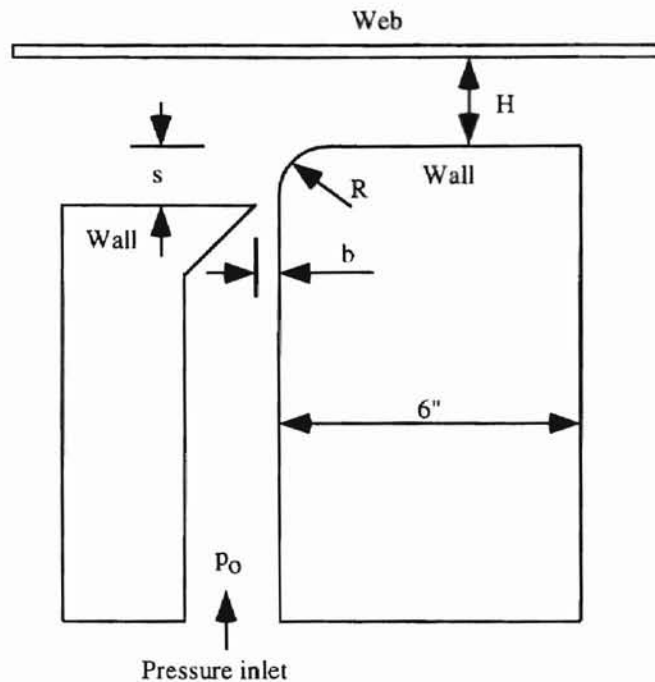
Figure 40. Schematic of the computational model with a web

The stationary rigid web, which has a surface roughness of 4.5×10^{-5} inches, is divided into three sections instead of one so that more nodes can be applied to each section. FLUENT/UNS has a limitation in the number of nodes being applied to a section. The maximum number of nodes is 240 nodes per section. Section BC should be much more dense than other areas. If an inappropriate mesh was designed close to the nozzle region and wall region, the solution may oscillate due to the large gradients of the pressure and velocity instead of reaching a stable solution.

The mesh in the region between the web and the wall near the nozzle region should be dense, since the velocity and pressure gradients are large in that region. An example mesh near the nozzle region is as shown in Figure 41. The nozzle region was refined as shown in Figure 42. The "Boundary Adaption" feature of FLUENT/UNS was used to refine the near wall region, which resulted in mesh refinement as seen in Figure

44

43. The mesh around the upper wall (web) remains fine to capture the effect of no-slip condition and the turbulent jet flow near the walls.

An important fact is that using the "Boundary Adaption", which is a refinement function of FLUENT/UNS, increases the time of calculation and the use of memory. So, an optimum mesh should be found by the subsequent refinements. When the refinement was done, the mesh had 10,497 nodes over all the computation domain, and 2780 nodes at the wall (Section AD in Figure 39).

Normally the number of iterations to convergence was around 1500 - 2500 for a residual value of 1×10^{-5}. When residuals become smaller than 1×10^{-5}, the solution is considered converged. In order to get a fully converged solution, iteration should be continued until the residuals do not decrease any more.

Grid

Fluent/UNS 4.2 (2d, rsm)
Thu Jun 10 1999
Fluent Inc.
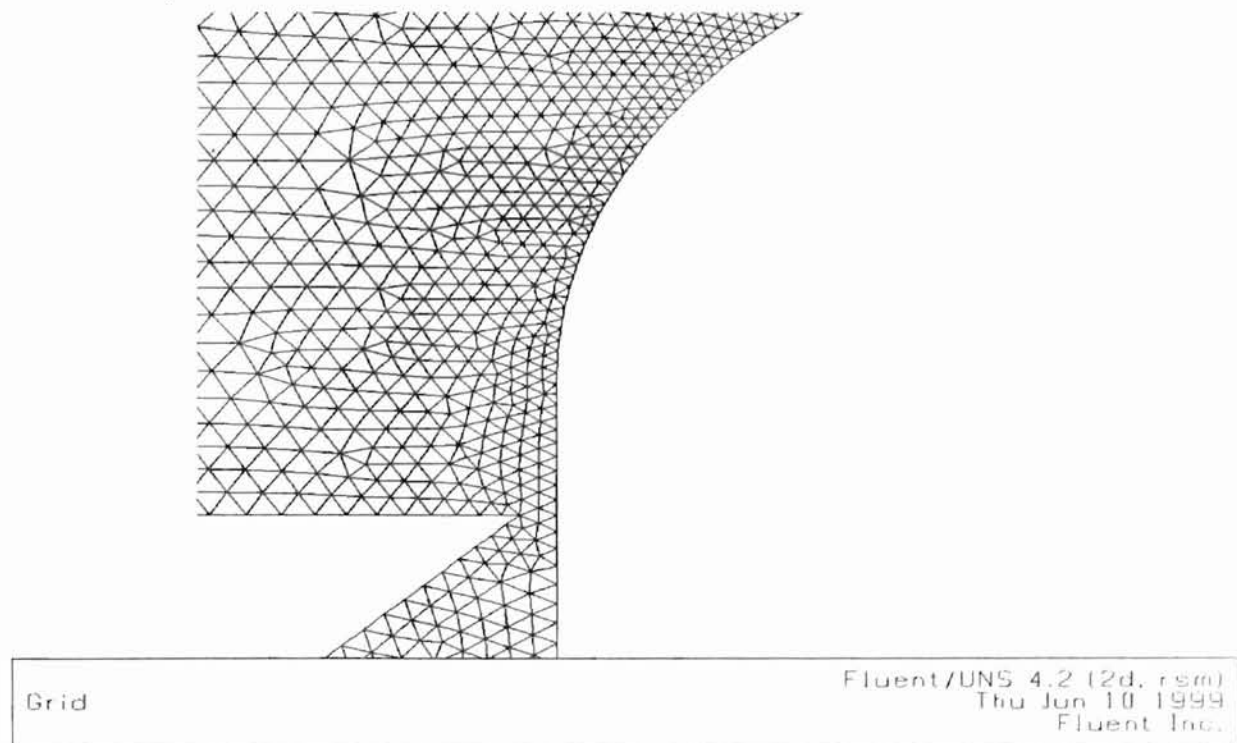
Figure 41. Mesh in the nozzle region before refinement

Grid
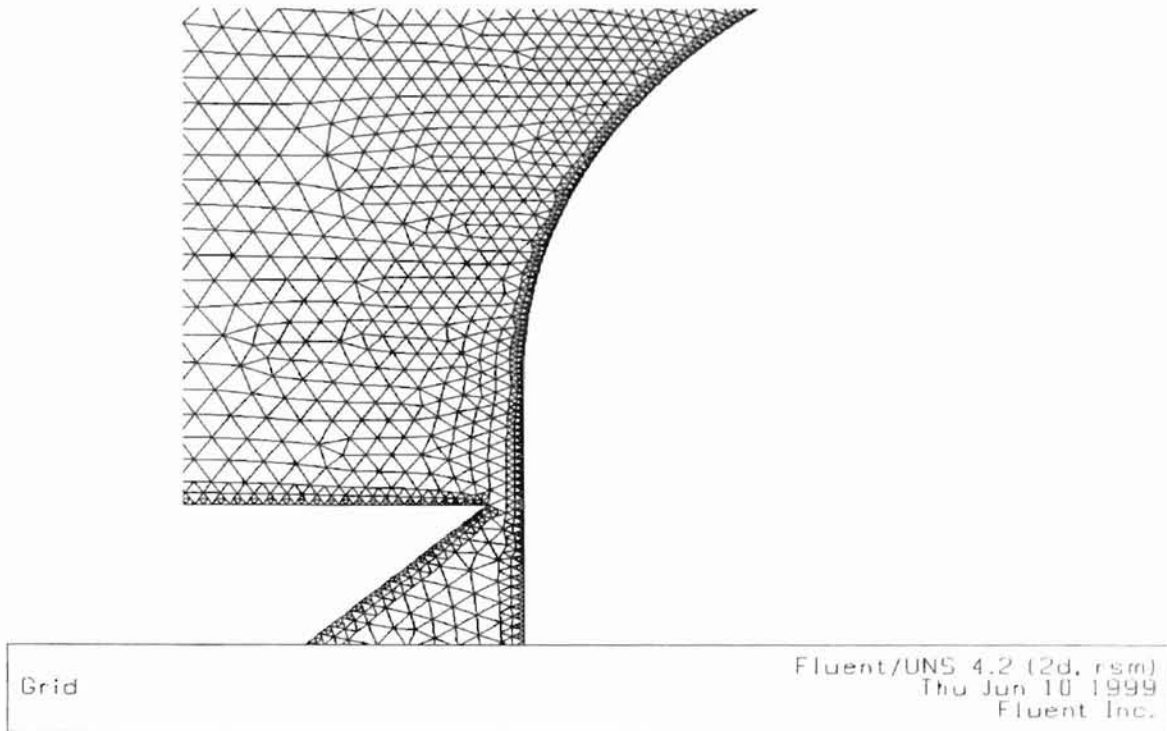
Figure 42. Mesh in the nozzle region after refinement

Grid
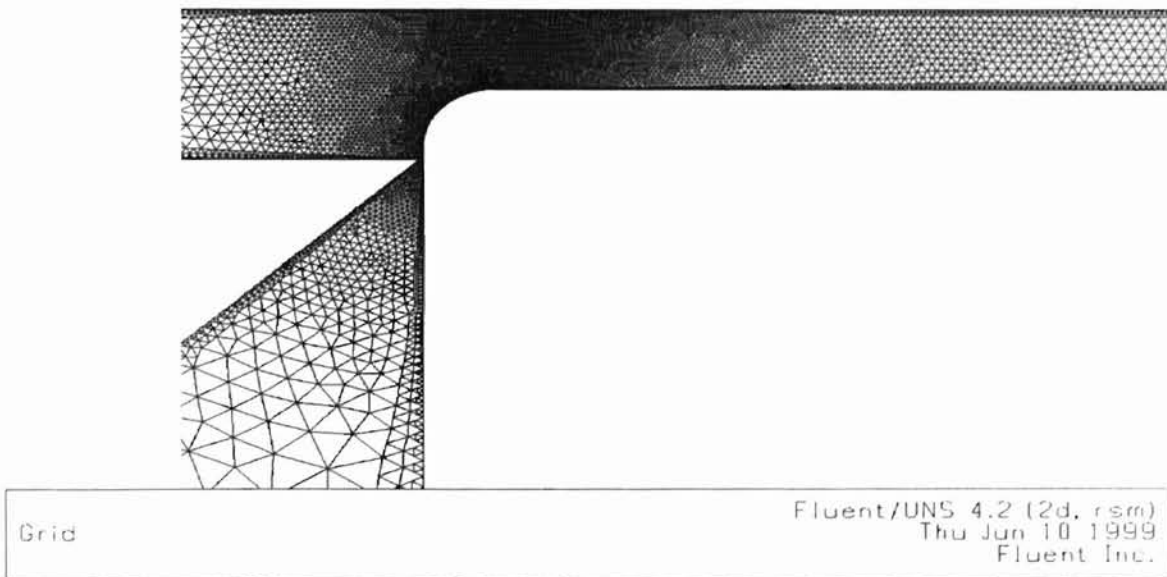
Figure 43. Mesh after refinement (same as Figure 42)

46

4.2.2   Results and discussion

Pressure distribution

A typical static profile on the web is shown in Figure 44. It is seen that the static

pressure on the web is negative (sub-ambient) upstream of and at the slot nozzle, but

become positive downstream of the slot nozzle. Note the dip in pressure profile at the

location of the slot nozzle and the sharp increase of pressure very near the slot nozzle.
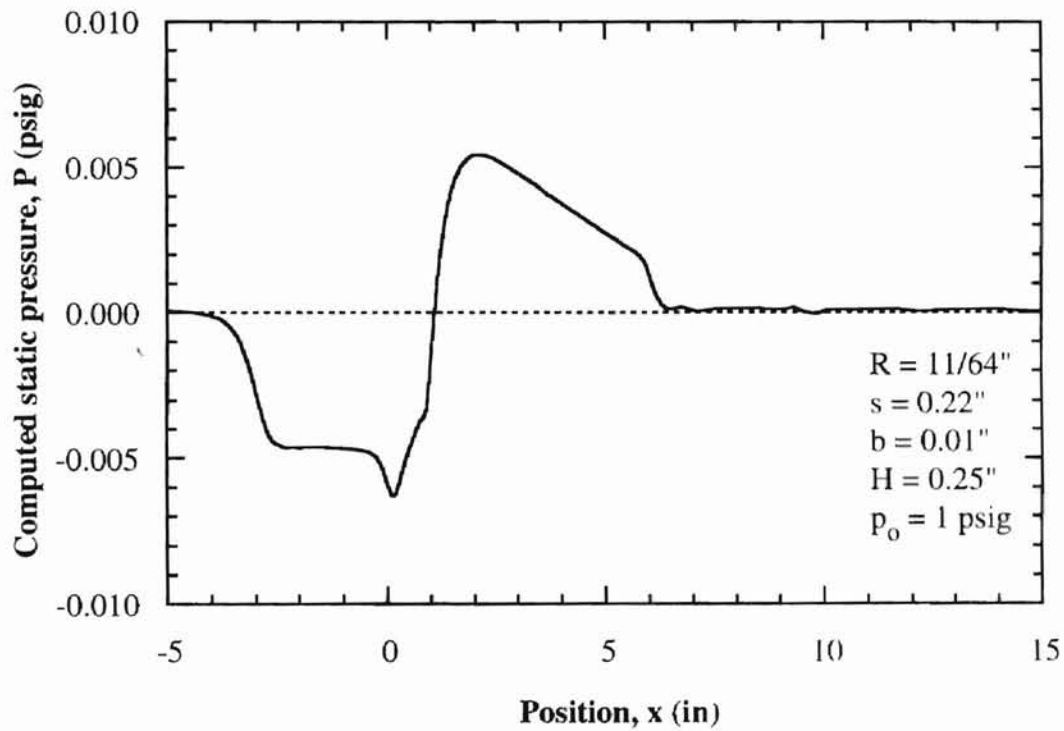
Figure 44. Pressure distribution on the stationary rigid web

When H = 0.10", smaller than the case shown in Figure 44, the positive pressure in the downstream of the slot nozzle significantly increases (Figure 45). The pressure profile is strongly affected by the floatation height H (Figure 45 and Figure 47). Negative pressure is dominant when the web is placed at a higher position; and positive pressure is dominant when floatation height is small. In all cases, the magnitude of the pressure is really proportional to the supply pressure (Figure 45 and Figure 47).
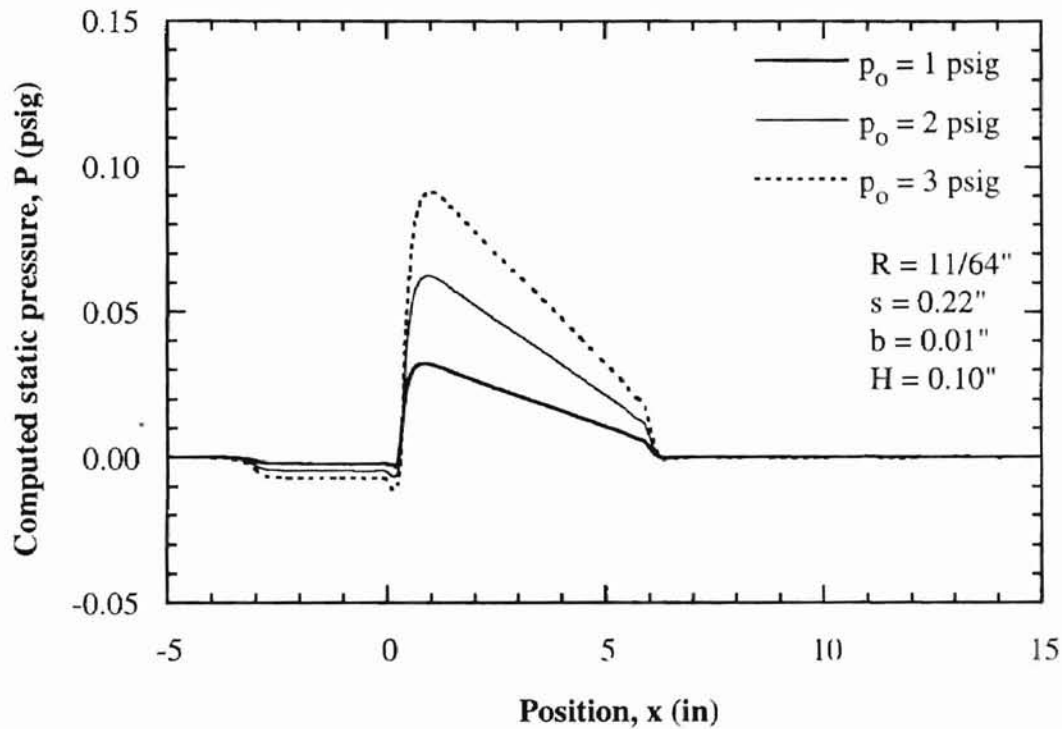
Figure 45. Pressure distribution on the web for different supply pressures (H = 0.1 in)
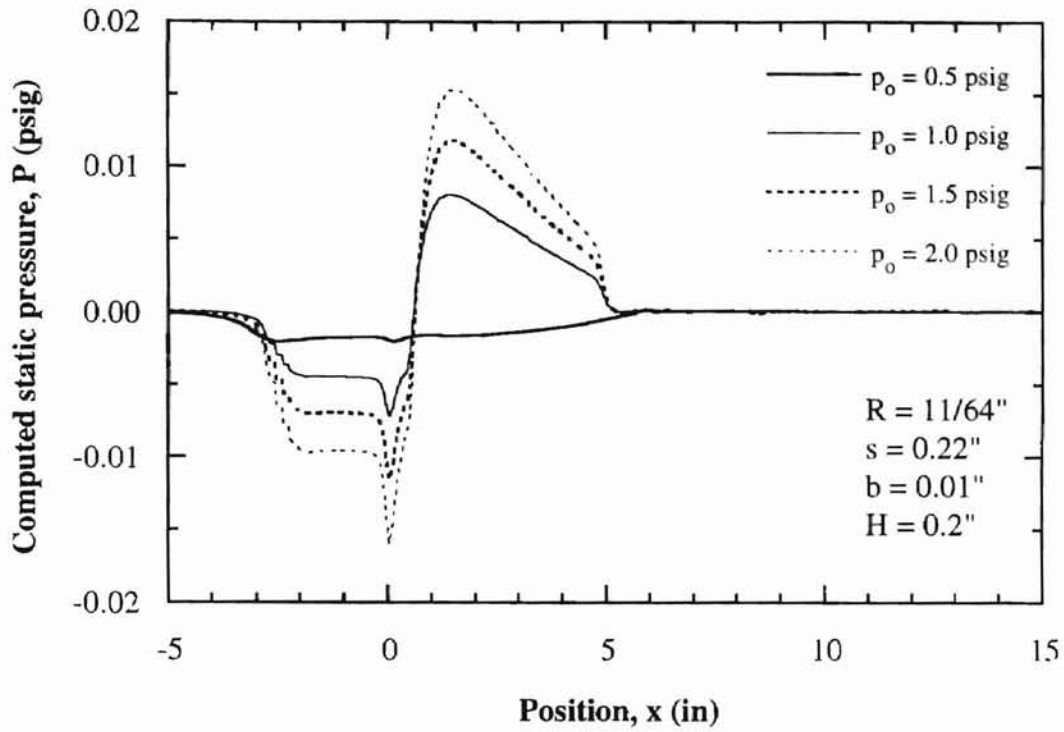
Figure 46. Pressure distribution on the web for different supply pressures (H = 0.2 in)
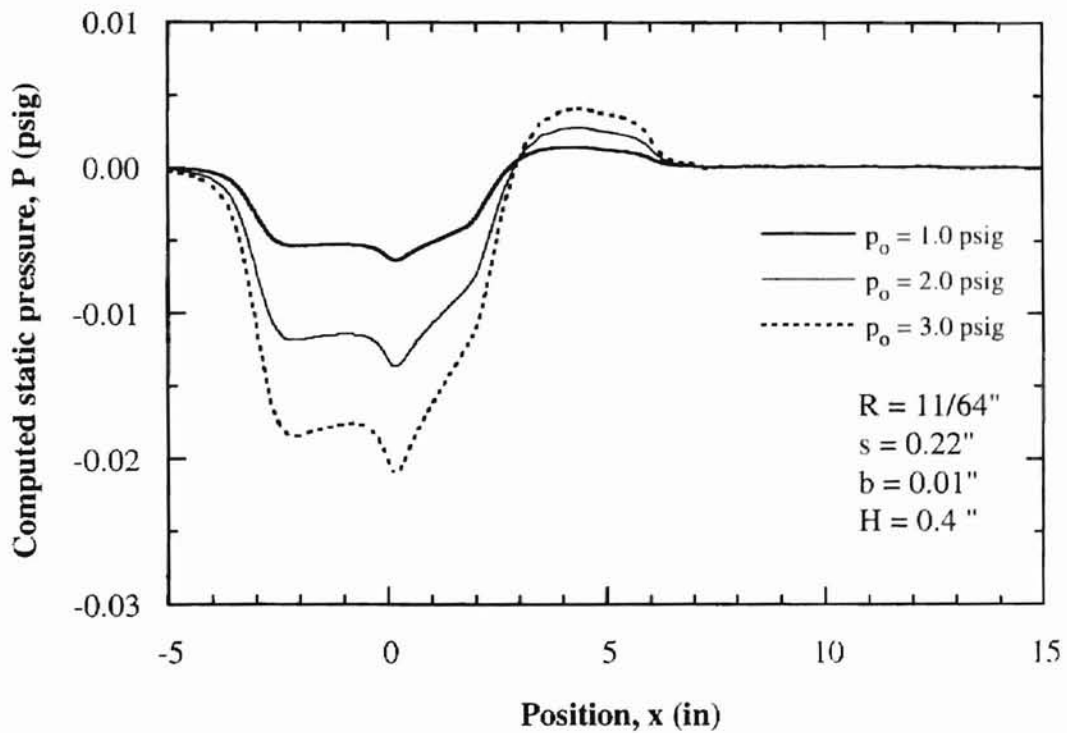
Figure 47. Pressure distribution on the web for different supply pressures (H = 0.4 in)

Pressure profiles on the rigid web are shown for various floatation heights for p_o = 1psig (Figure 48), p_o = 2psig (Figure 49), p_o = 3psig (Figure 50). These figures clearly show that the location when the static pressure becomes maximum shifts toward the downstream as the floatation height increases in all cases.
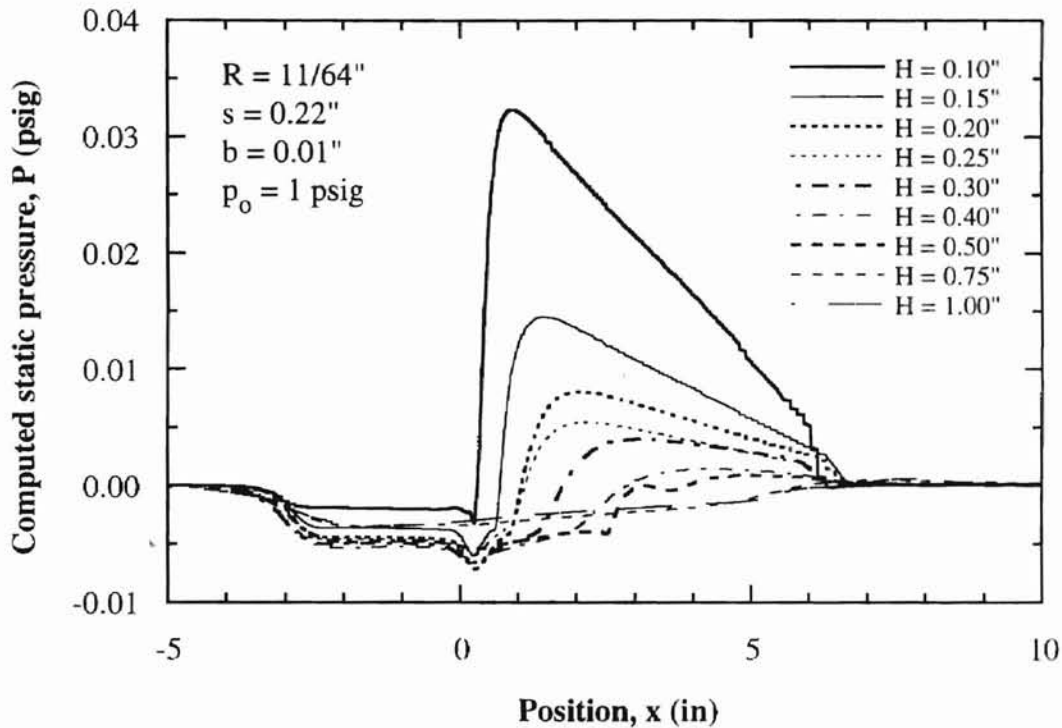
Figure 48. Pressure distribution on the web for different floatation heights (p_o = 1 psig)

Figure 48 shows the pressure distribution near the nozzle region. Comparing the pressure profiles for different floatation heights, the peak shifts up as the web is placed at a lower position. The change in magnitude of the pressure peaks show that positive pressure is dominant at a lower floatation height. Other examples for the different supply pressures are shown in Figure 49 and Figure 50.
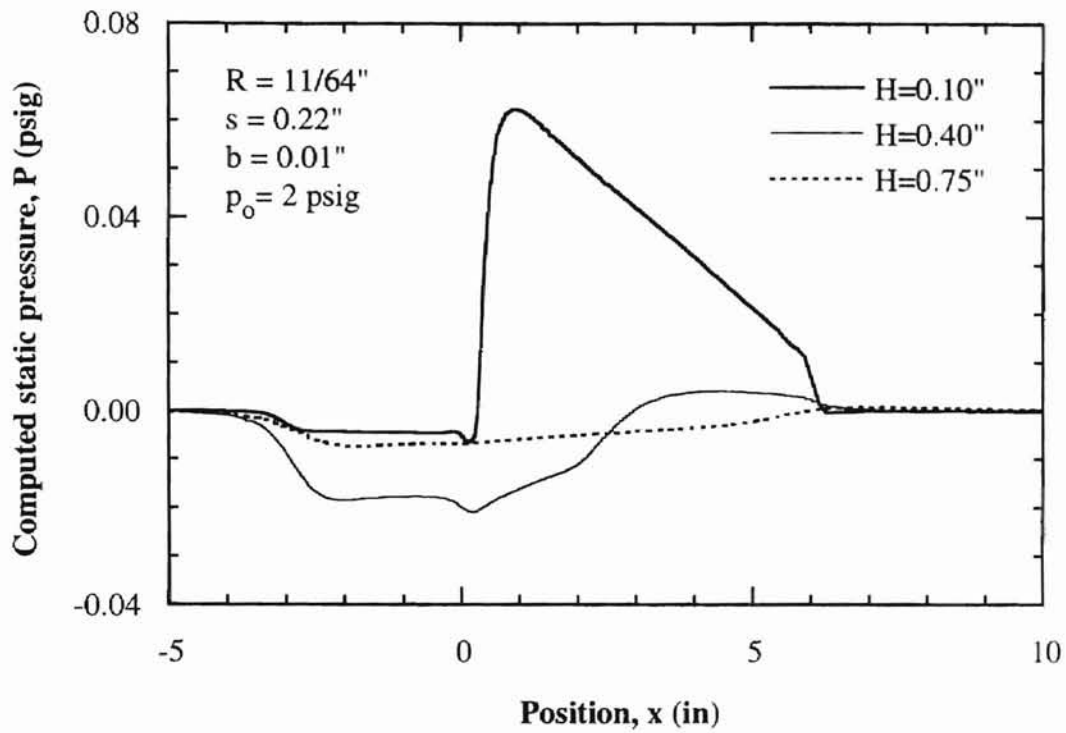
Figure 49. Pressure distribution on the web for different floatation heights (p_o = 2 psig)
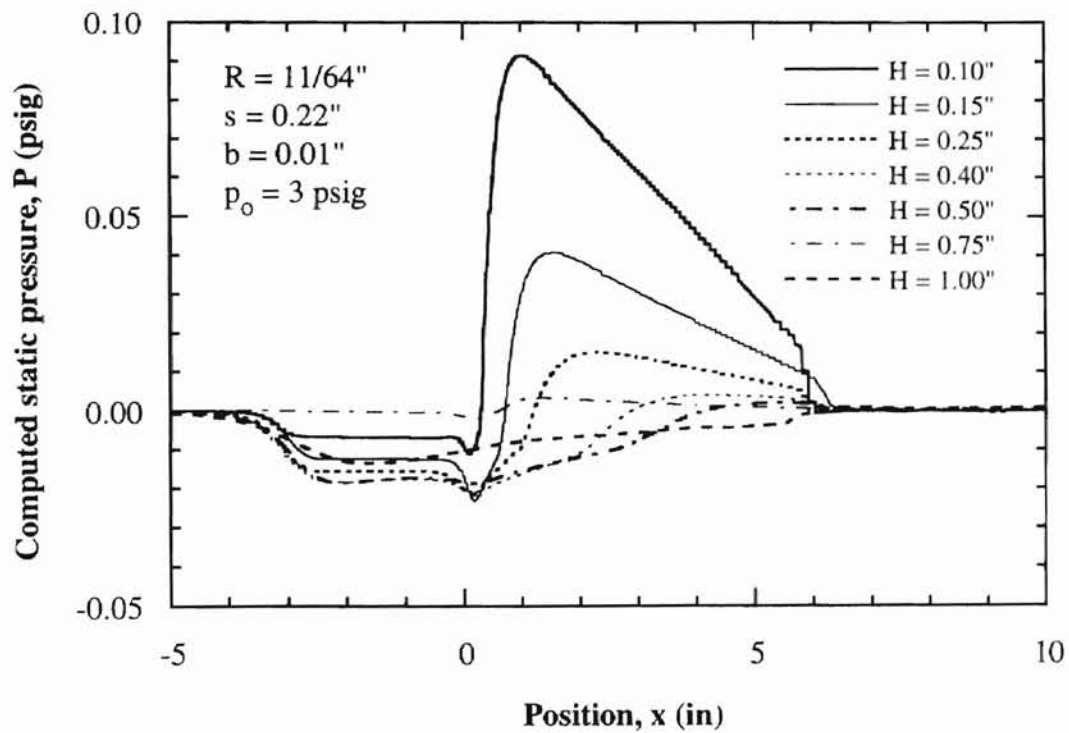
Figure 50. Pressure distribution on the web for different floatation heights (p_o = 3 psig)

The total lift force (per unit width of web) is obtained by integrating the pressure profile. Figure 51 and Figure 52 show the dependence of lift force on supply air pressure and floatation height. When the floatation height is small (H = 0.10"), the lift force is positive in the entire range of test, and increases with the supply pressure. At a large value of floatation height (H = 0.50"), the lift force is negative, and its magnitude increases with the supply pressure. It appears that there is a value of floatation height, near H = 0.25", at which the lift force becomes nearly zero without being affected by the supply pressure. That is the floatation height of H = 0.25" is the equilibrium position for a rigid, non-tilted, web with a nozzle width of b = 0.01". This value of floatation height is barely affected by the supply air pressure.
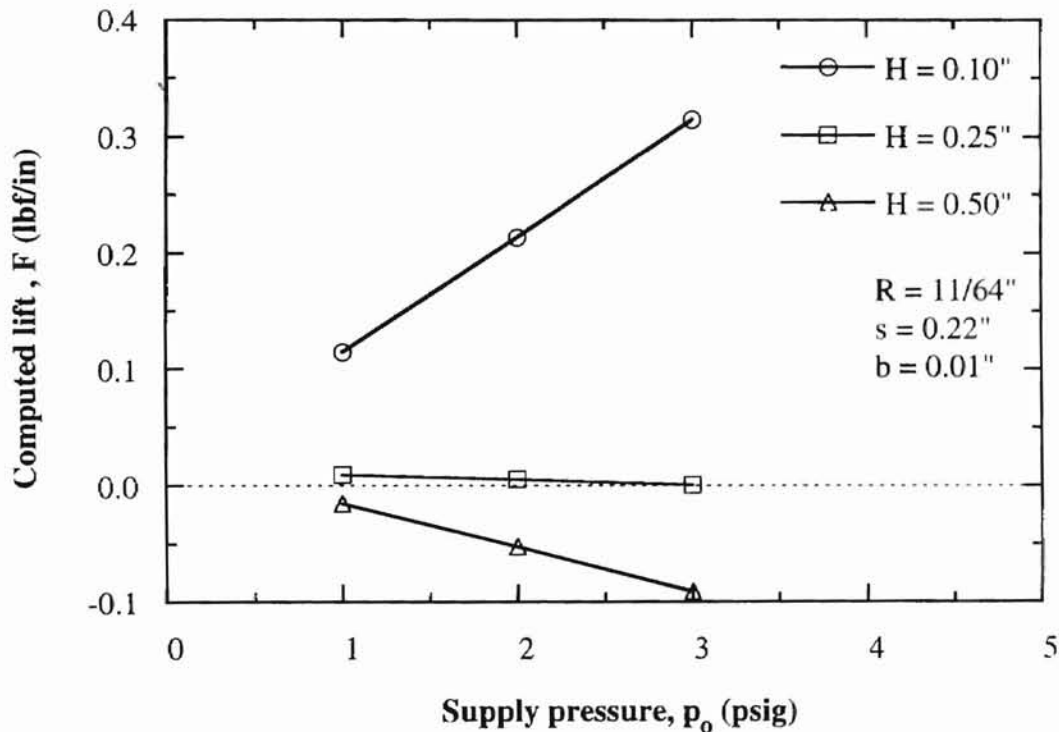
Figure 51. Effects of supply pressure and floatation height on lift force
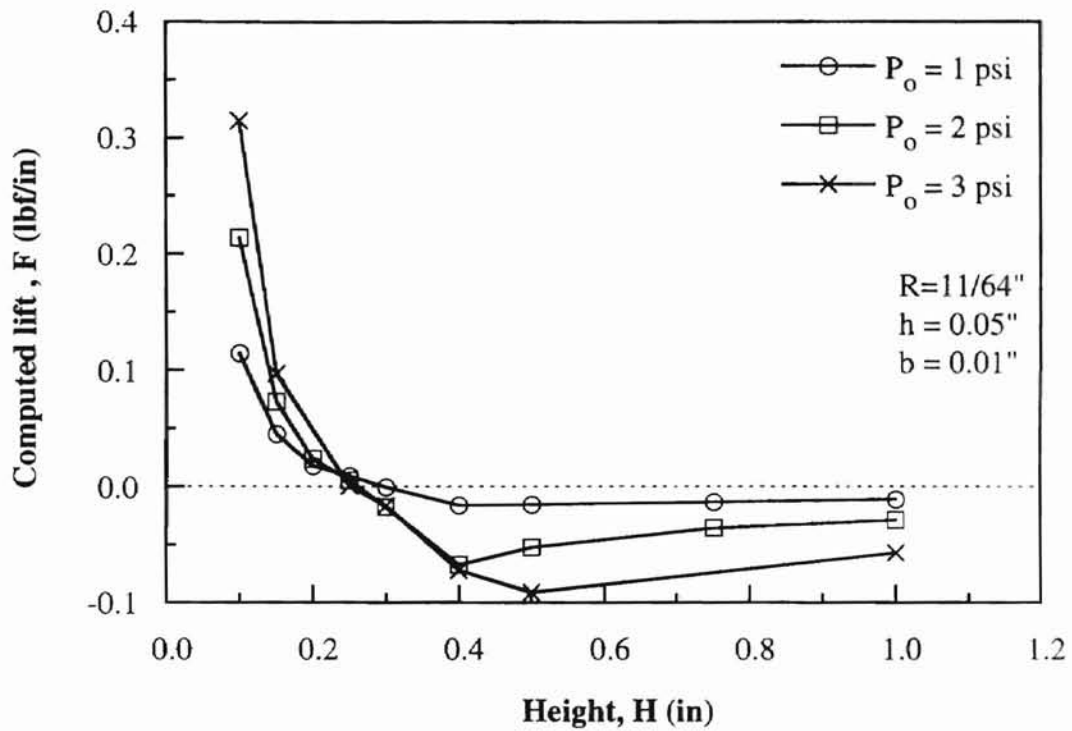
Figure 52. Effects of floatation height and supply pressure on lift force

Aerodynamic traction on the web

Wall shear stress profiles for various flotation heights are shown in Figure 53. The shear stress downstream of the air exit (slot) dramatically reduces as the floatation height increases.
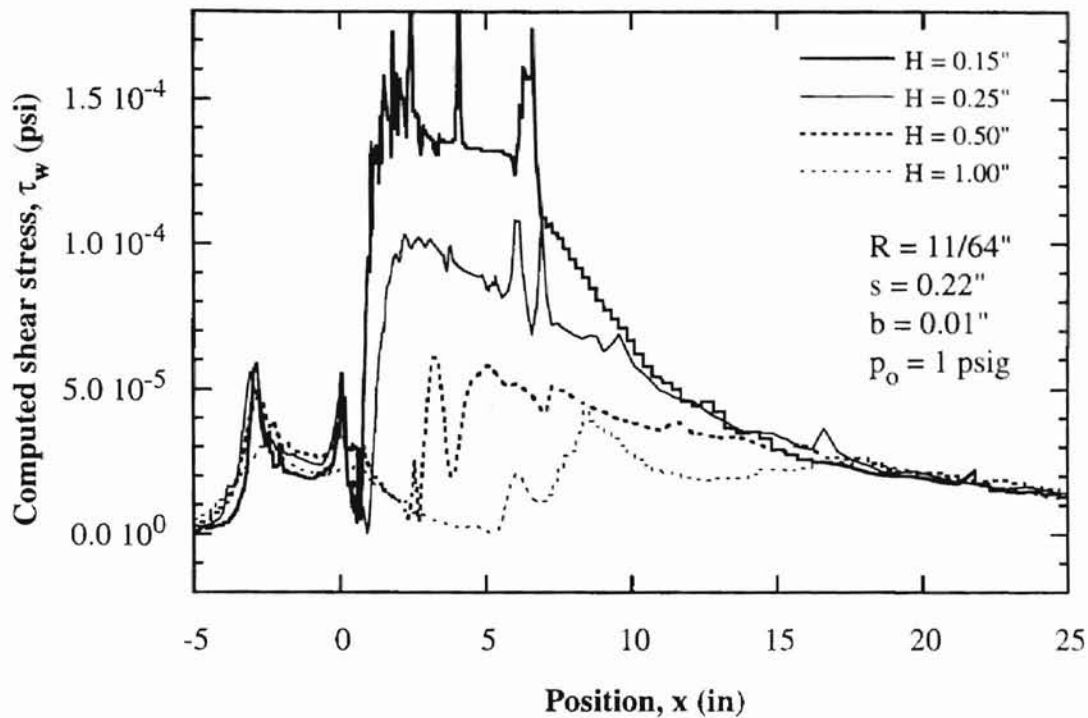
Figure 53. Distribution of wall shear stress on the stationary rigid web

By integrating the shear stress profiles along the flow direction, the aerodynamic traction (force per unit width) was obtained for various values of floatation height and supply air pressure as shown in Figure 54. The trapezoidal method was used to perform this integration. It is seen that the aerodynamic traction on the web is almost linearly proportional to the supply air pressure. It is also seen that the effect of the supply pressure is more dramatic when the floatation height is small. The same data shown in Figure 54 is plotted in Figure 55 in different format. Refer to Table 4 for exact values of the data.
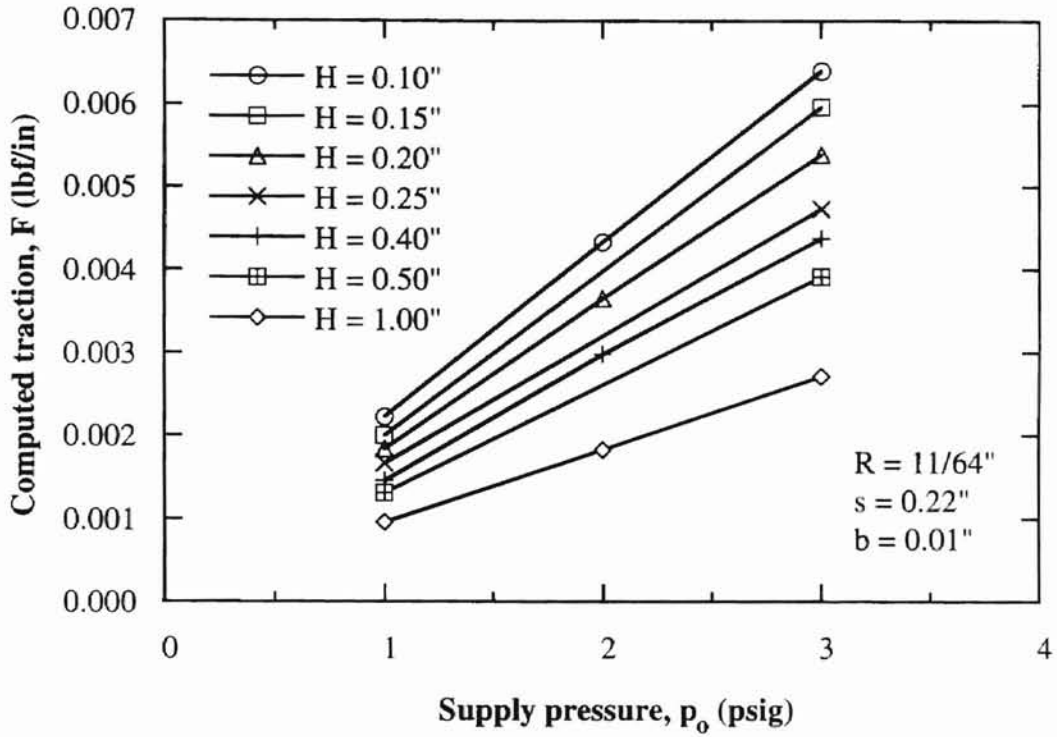
Figure 54. Effects of supply pressure and floatation height on traction
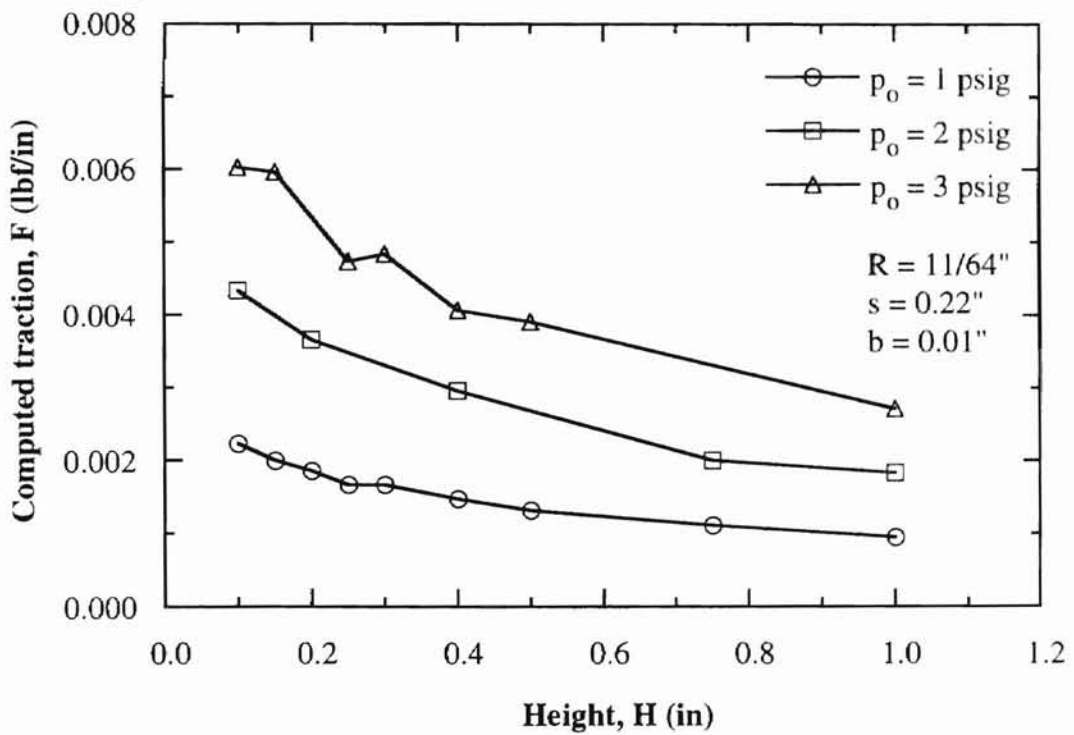
Figure 55. Effects of floatation height and supply pressure on traction

Table 4. Computed aerodynamic traction on a stationary rigid web for various supply
pressures and floatation heights (lbf/in)

	H = 0.1"	H = 0.2"	H = 0.4"	H = 1.0"
P_o = 1 psig	0.002228	0.001843	0.001459	0.000954
P_o = 2 psig	0.004338	0.003659	0.002980	0.001834
P_o = 3 psig	0.006402	0.005389	0.004376	0.002714

4.3 Coanda Air Jet and a Moving Rigid Web

4.3.1 Description of the computational model

The computational model shown in Figure 56. The model is the same as that described in Section 4.3.1 with minor differences. It is almost the same as the previous model of the stationary rigid web, but a moving situation is now presented. The right pressure boundary was placed 160 inches from the slot nozzle, and the left pressure boundary was placed 40 inches from the slot nozzle.
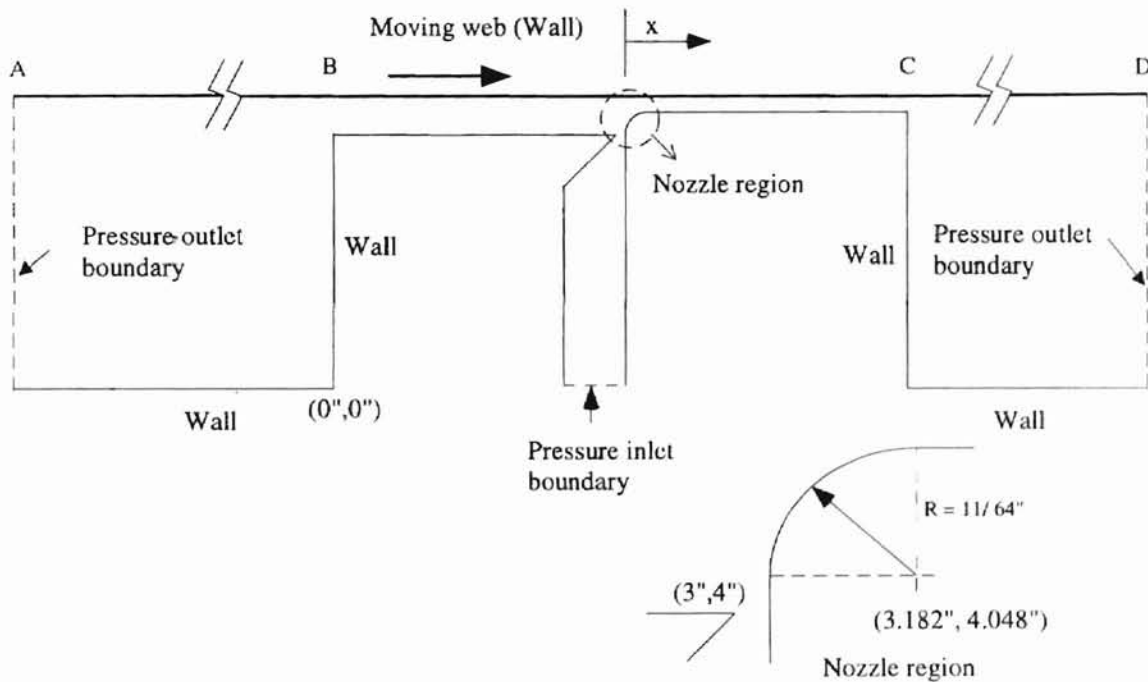
Figure 56. Computational model for a moving rigid web

Figure 57 shows the original mesh in the wall region. The original mesh near the wall region was refined as shown in Figure 58. To capture the effect of no-slip condition and the turbulent jet at the walls, the "Boundary Adaption" feature of FLUENT/UNS was

used twice to refine the mesh near the wall region.

Figure 59 shows a varying pressure profile with different mesh densities along the web. Finally, 2692 nodes fit this calculation at the wall with a roughness of 4.5 E-5 inches (Section BC in Figure 56). When the mesh was created, the final refined mesh contained 18,449 nodes.
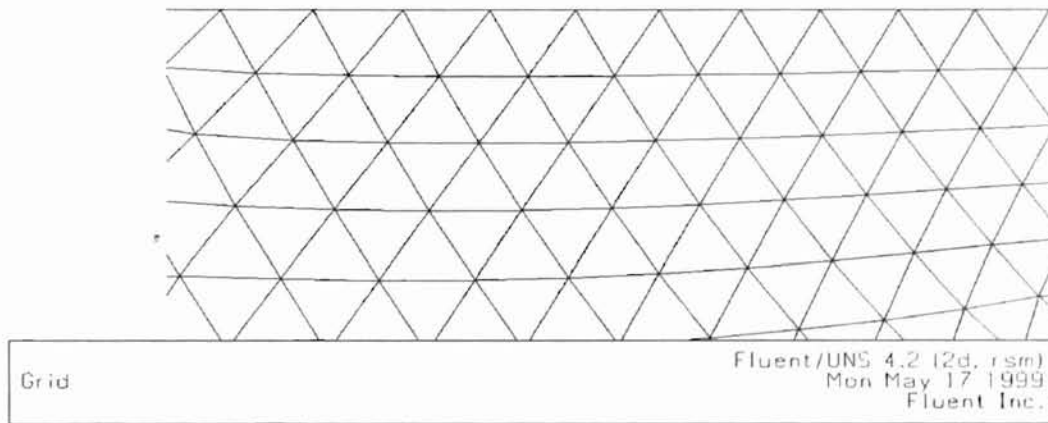
Figure 57. Mesh in the wall region before refinement
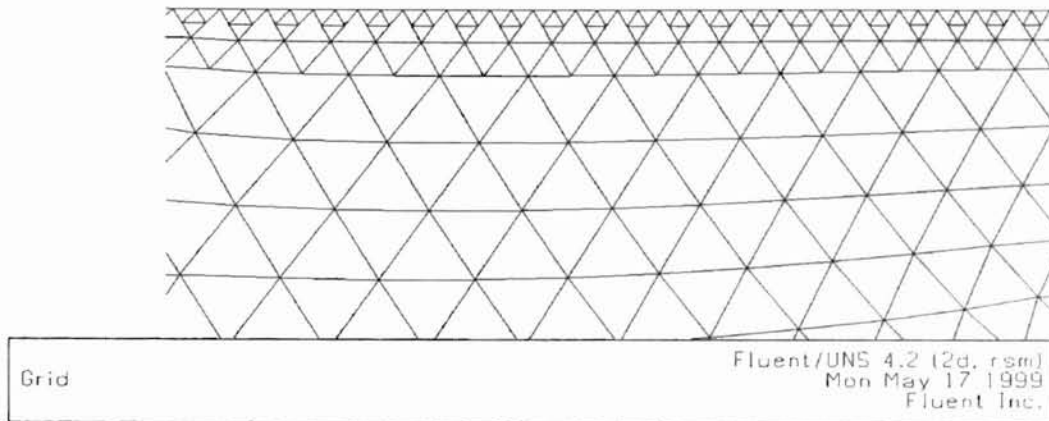
Figure 58. Varying mesh density in the wall region after refinement

As seen in Figure 59, the treatment near the wall significantly impacts the fidelity of numerical solutions, because the walls are the main source of mean vorticity and turbulence. It is in the wall region that the momentum and other scalar transports change to a large degree. Thus, the accurate treatment near the wall determines successful predictions of wall-bounded turbulent flow. It is known that the region near the wall is divided into three layers: viscous sublayer, buffer layer, and fully turbulent region or log-law region. The viscous sublayer is almost laminar, and the viscosity plays a major role in momentum and heat or mass transfer in that region; in the log-law region turbulence plays a dominant role: and the effect of viscosity and turbulence are equally important in the buffer layer between the viscous sublayer and fully turbulent layer. FLUENT/UNS has three models for the wall treatment: Standard Wall Function, Non-Equilibrium Wall Function, and Two-Layer Zonal Model. In this study the Non-Equilibrium Wall Function

was used for the region near the wall. This approach does not resolve all the way down to the wall, but this wall function will bridge the viscosity-affected region between the wall and the fully turbulent region. The wall function approach is popular because it is economical, robust, and reasonably accurate. The FLUENT/UNS manual recommends that among the wall functions the Non-Equilibrium Wall Function is especially good for use in complex flows involving separation, reattachment, and impingement where the mean flow and turbulence are subjected to severe pressure gradients and rapid changes. The Two-Layer Zonal Model is recommended for a pervasive low-Reynolds-number, massive transpiration, and severe pressure gradients leading to boundary layer separations. An excessively fine mesh near the wall region should be avoided because the wall functions cease to be valid in viscous sub-layer. If the user wants to use the Two-Layer Zonal Model for proper situations as mentioned above, ten cells must be within the viscosity affected near-wall region, which includes the viscous sub-layer and the buffer layer. After the mesh has been created with the concept mentioned above, an appropriate mesh for the near wall region is found using the Adaption, which is a refinement function of FLUENT/UNS. As seen in Figure 59, the solution of the static pressure on the web does not change much with the second adaption of the mesh near the wall. This is the appropriate mesh for the wall for this calculation.
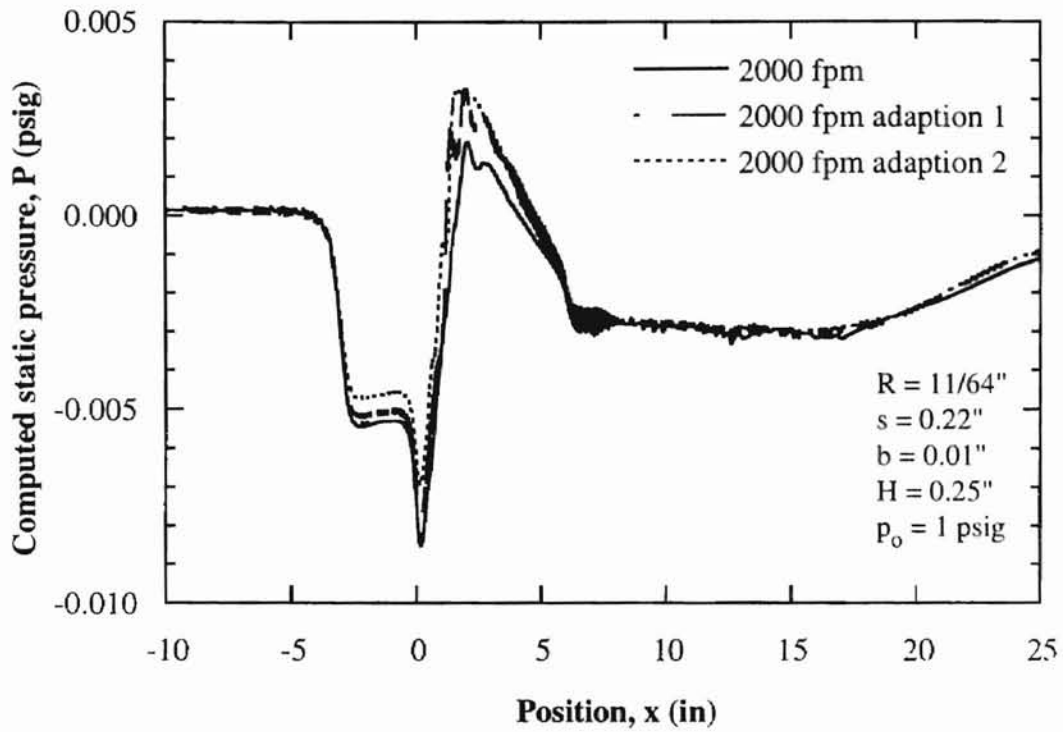
Figure 59. Effect of mesh adaption on pressure profile

The number of iterations to convergence was about 2500 - 3000 to meet a residual

value of 1×10^{-5} for this simulation. When residuals become smaller than 1×10^{-5}, the

solution is considered converged.

4.3.2   Results and discussion

Pressure distribution

The effects of the translating motion of a rigid web on the pressure profile are shown in Figure 60. The main effect of web speed appears as reduction of pressure on the web, especially in the region downstream of the slot nozzle.
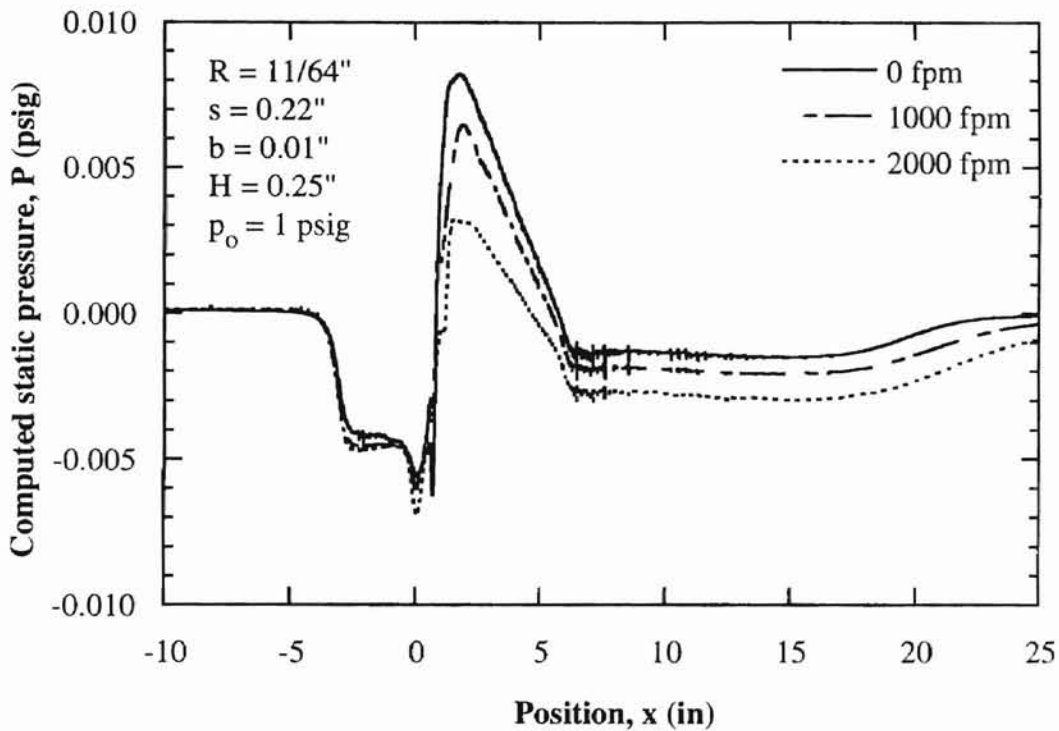
Figure 60. Effects of speed of web on pressure distribution (p_o = 1 psig)

Figure 61 shows another example of the pressure distribution near the nozzle region for the supply pressure of 2 psig. High translating speed of the web makes the pressure on the web reduced as for p_o = 1 psig. Compared to the case for p_o = 1 psig,

however, the effect of web speed on the pressure profile is less significant when $p_o = 2$ psig. The effect of web speed becomes almost negligible when the supply pressure is 3 psig (Figure 62).
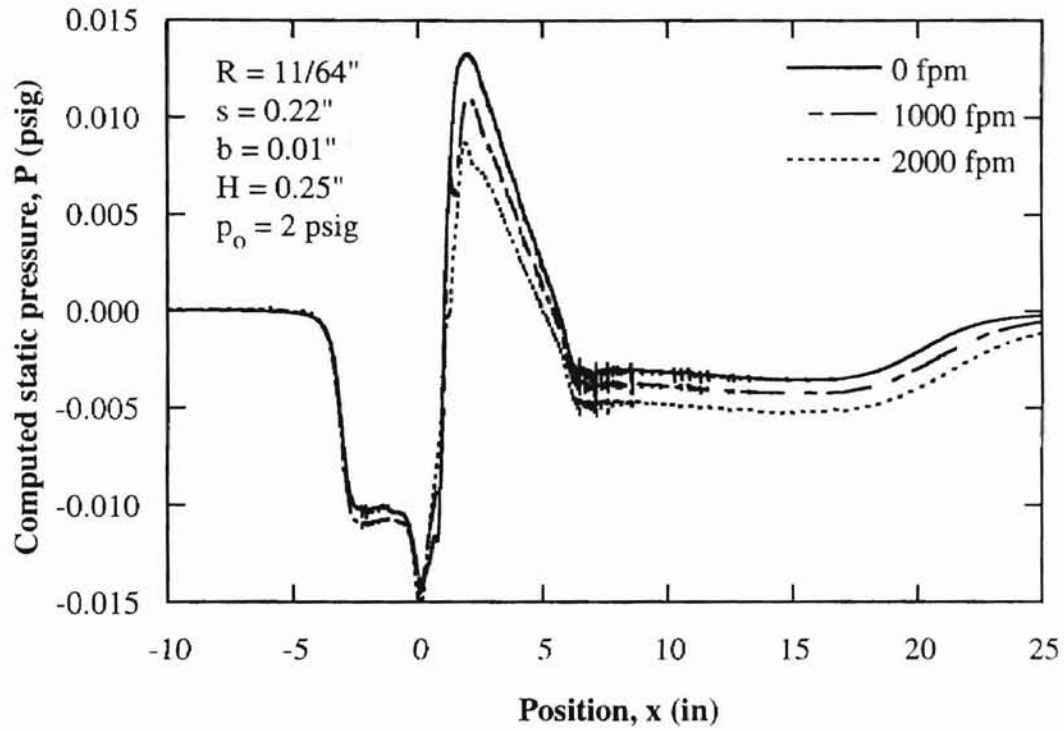
Figure 61. Effects of speed of web on pressure distribution ($p_o = 2$ psig)
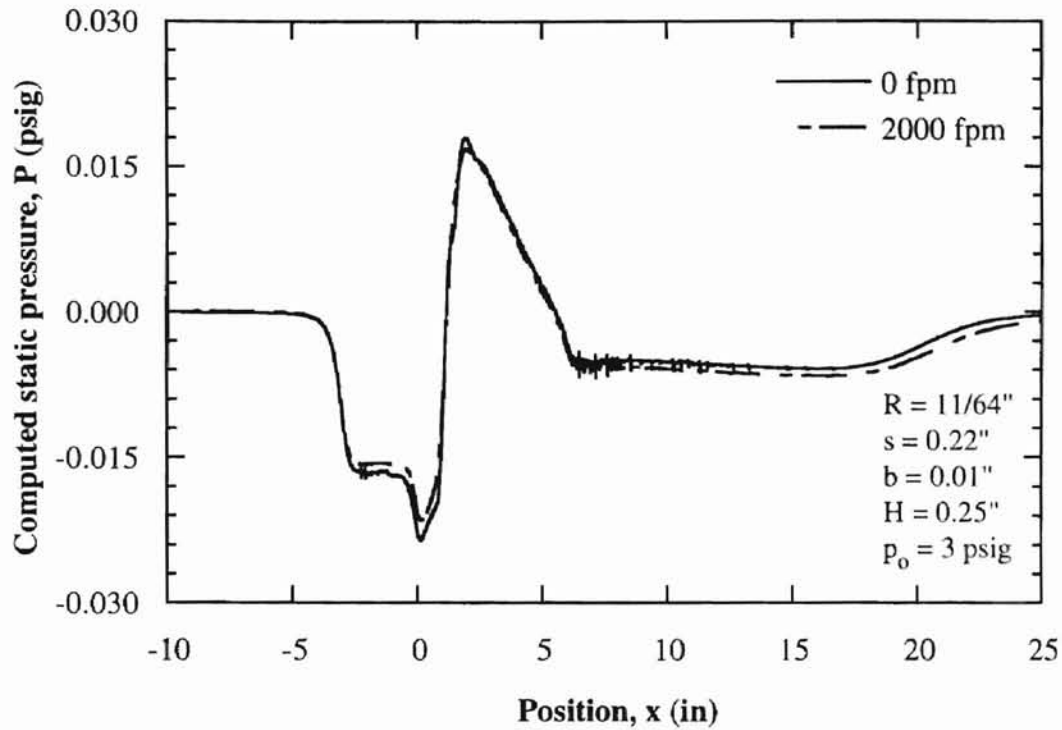
Figure 62. Effects of speed of web on pressure distribution (p_o = 3 psig)

As shown in Figure 63, the lift force on the web decreases as the web speed increases. This implies that the equilibrium position of a translation rigid web will be lower than that of a stationary web. This effect is clearly seen for lower supply pressures such as 1 and 2 psig.
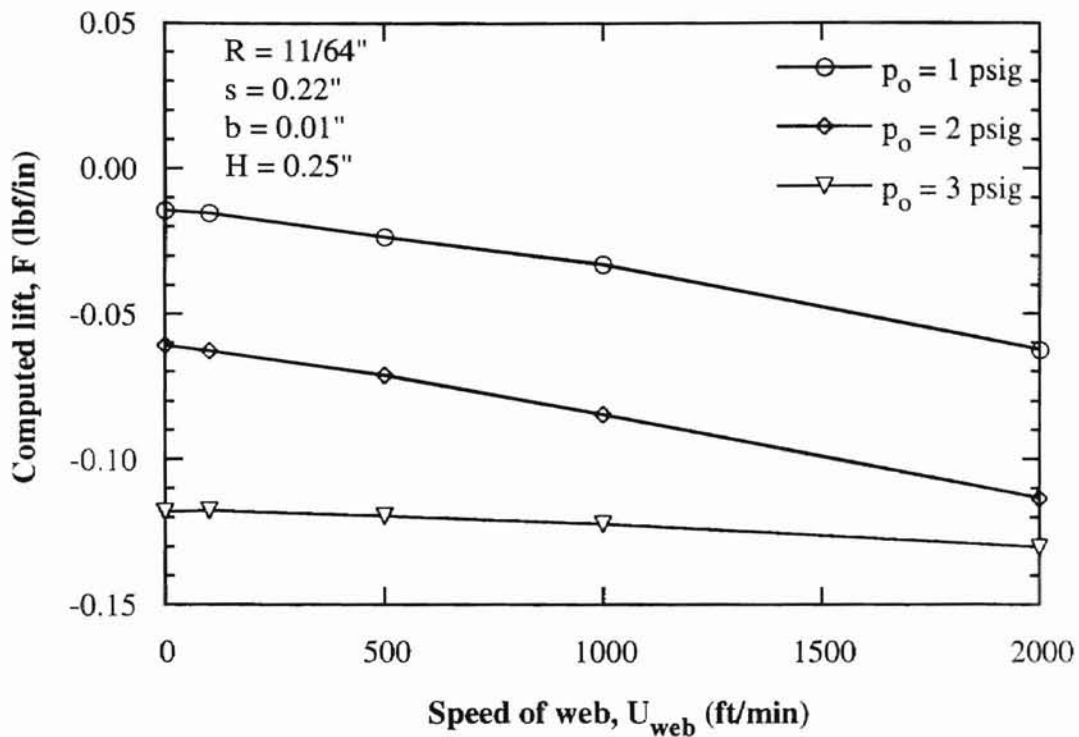
Figure 63. Effects of speed of web and supply pressure on lift force (H = 0.25 in)

Aerodynamic traction on the web

Wall shear stress profiles on a moving, rigid web are shown in Figure 64. The magnitude of the shear stress in the main working region ($0 < x < 6$") seems to be inversely proportional to the speed of the web.

Wall shear stress profiles on the rigid moving web at different supply pressures (2 and 3 psi) are shown in Figure 65 and Figure 66. The general trend of the curve is almost the same as shown in Figure 64 for $p_o = 1$ psi. The difference is that the effect of web speed seems less significant at high supply pressures.
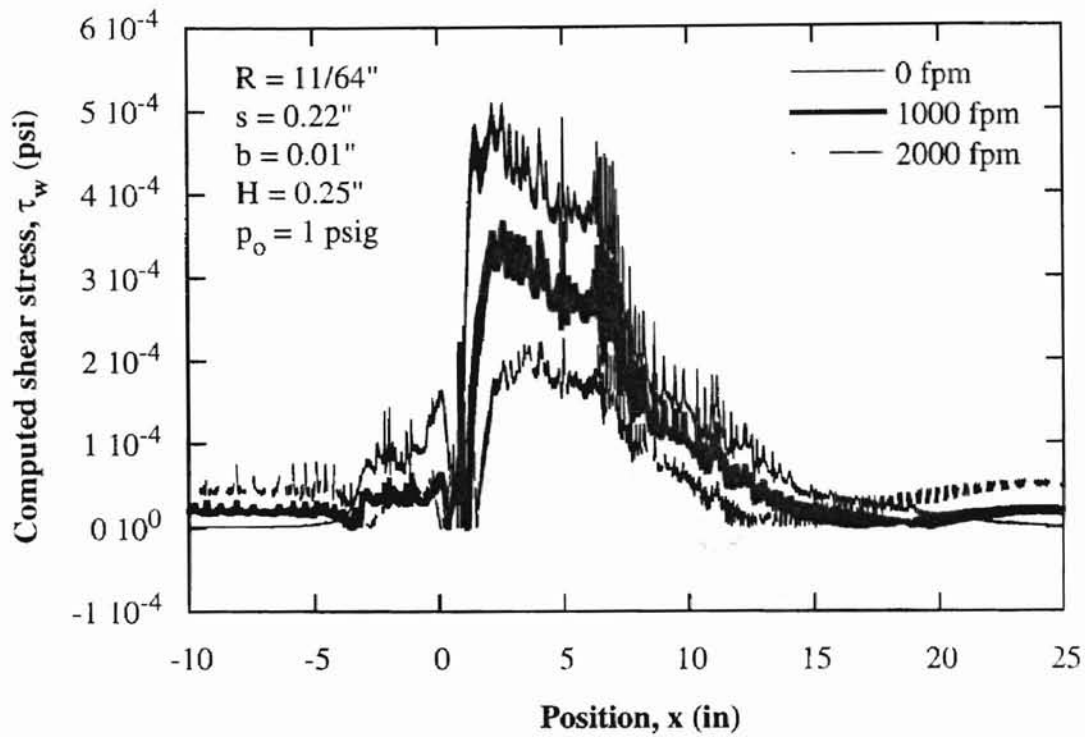
Figure 64. Effects of web speed on the shear stress profile (p_o = 1 psig)
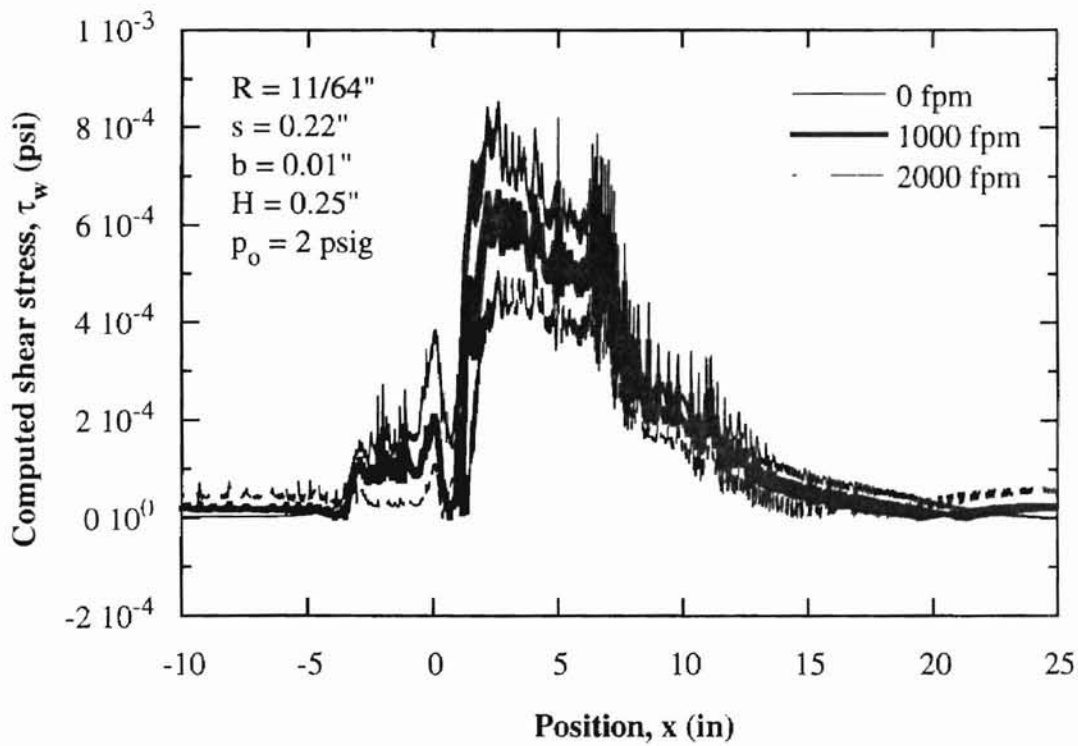
Figure 65. Effects of speed of web on shear stress profile (p_o = 2 psig)
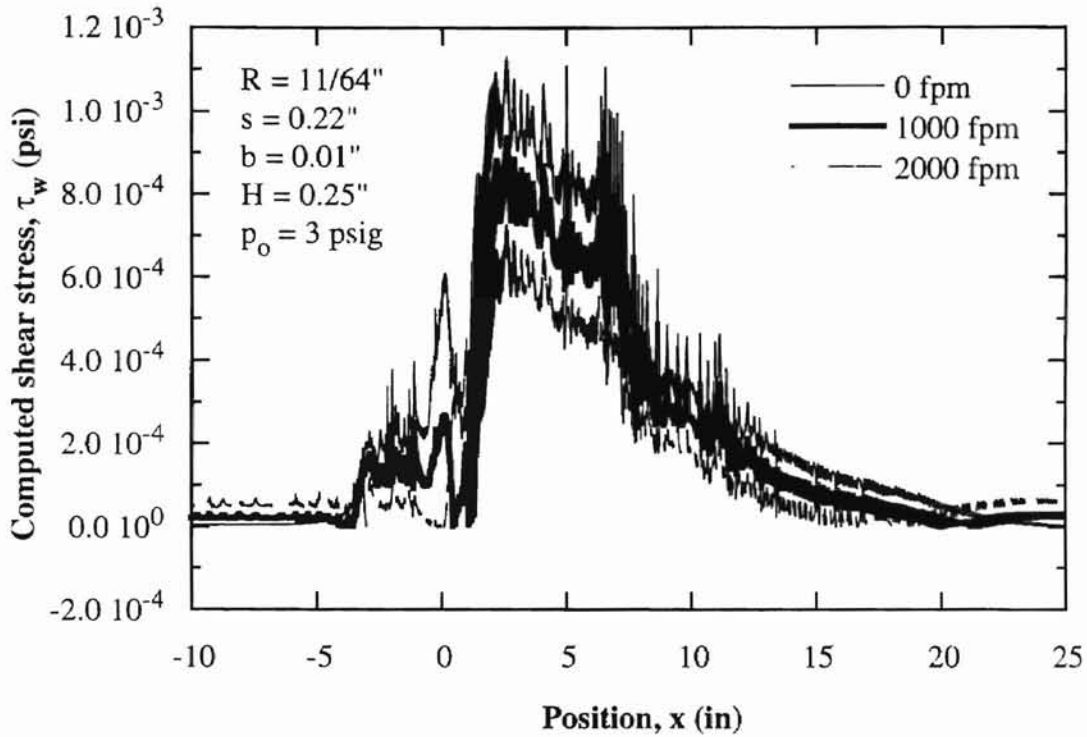
Figure 66. Effects of speed of web on shear stress profile (p_o = 3 psig)

Integrating the wall shear stress over the web (Section BC in Figure 39) gives the traction acting on the web per unit width. The trapezoidal rule was used to perform this integration over the web. As seen in Figure 67, the traction of the air jet decreases as the speed of web increases. The effects of web speed on the aerodynamic traction become less significant when the supply air pressure is high. The results are tabulated in Table 5.
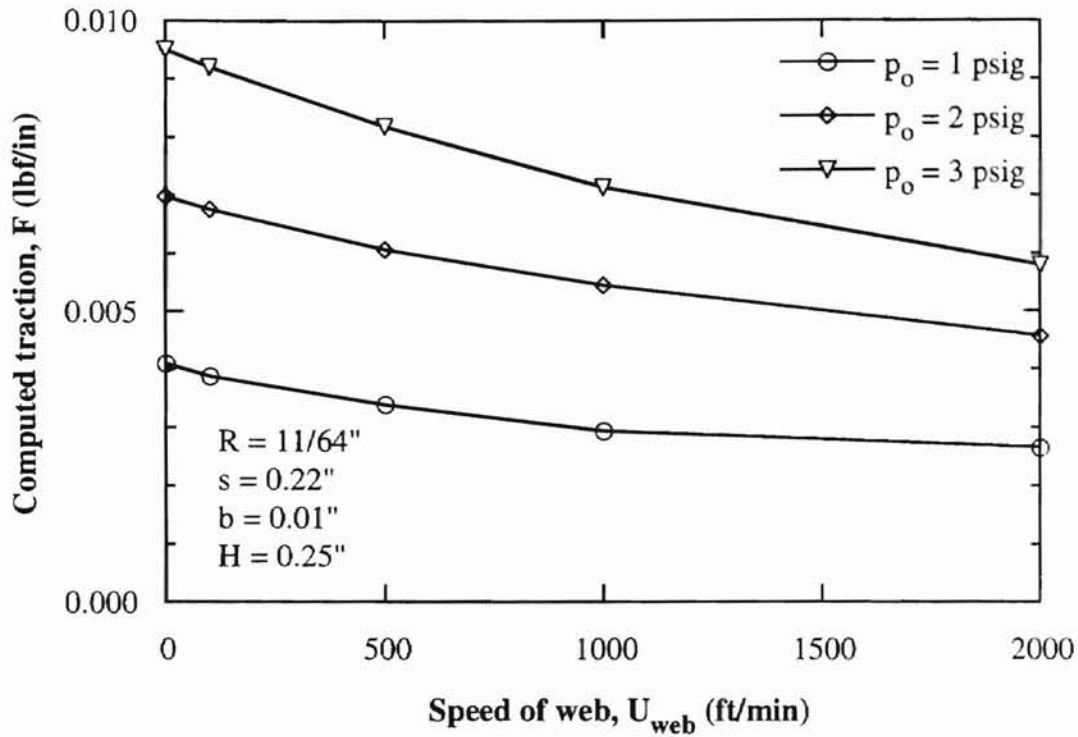
Figure 67. Traction on the moving rigid web

Table 5. Aerodynamic traction on the moving rigid web for various supply pressures and speeds of web

	$U_{web} = 0$	100 fpm	500 fpm	1000 fpm	2000 fpm
$p_o = 1$ psig	0.0041	0.00388	0.00339	0.00294	0.0026
$p_o = 2$ psig	0.0070	0.00676	0.00607	0.00545	0.0046
$p_o = 3$ psig	0.0095	0.00921	0.00818	0.00714	0.0058

Figure 68 to Figure 75 show the flow patterns in the nozzle region for various supply pressures and web speeds. Note the recirculation zone near the stationary web for $p_o = 1$ psig shown in Figure 69. In this recirculation region, velocity of the flow is nearly zero as shown in the contours of velocity and the velocity vectors (Figure 68 and Figure 69). As the web speed or supply pressure is increased, this vortex disappears (Figure 70 and Figure 75).

A stagnation zone is observed on the web, which becomes smaller and moves

downstream as the supply air pressure or the web speed increases (Figure 68, Figure 70, Figure 72, and Figure 74). In all cases the air jet was always attached to the surface of the curved block and a stream of air entrained seen in all the figures.
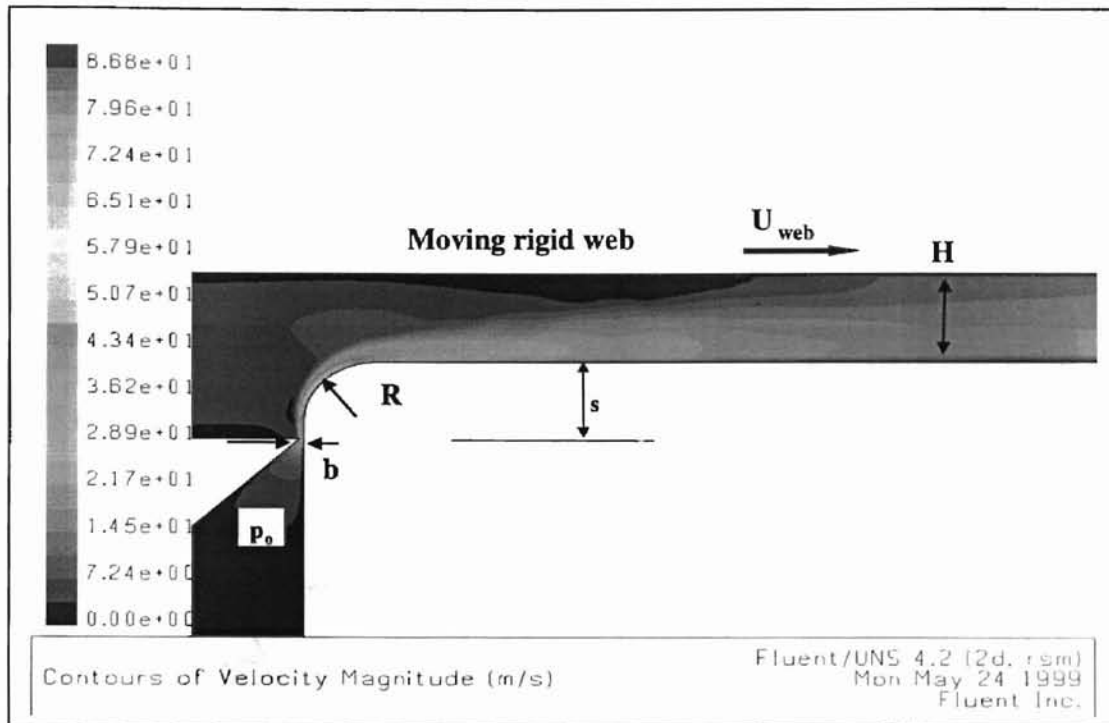
Figure 68. Velocity contours for a moving rigid web (R = 11/64 in, s = 0.22 in, b = 0.01 in, H = 0.25 in, p_o = 1 psig, U_{web} = 0 ft/min)
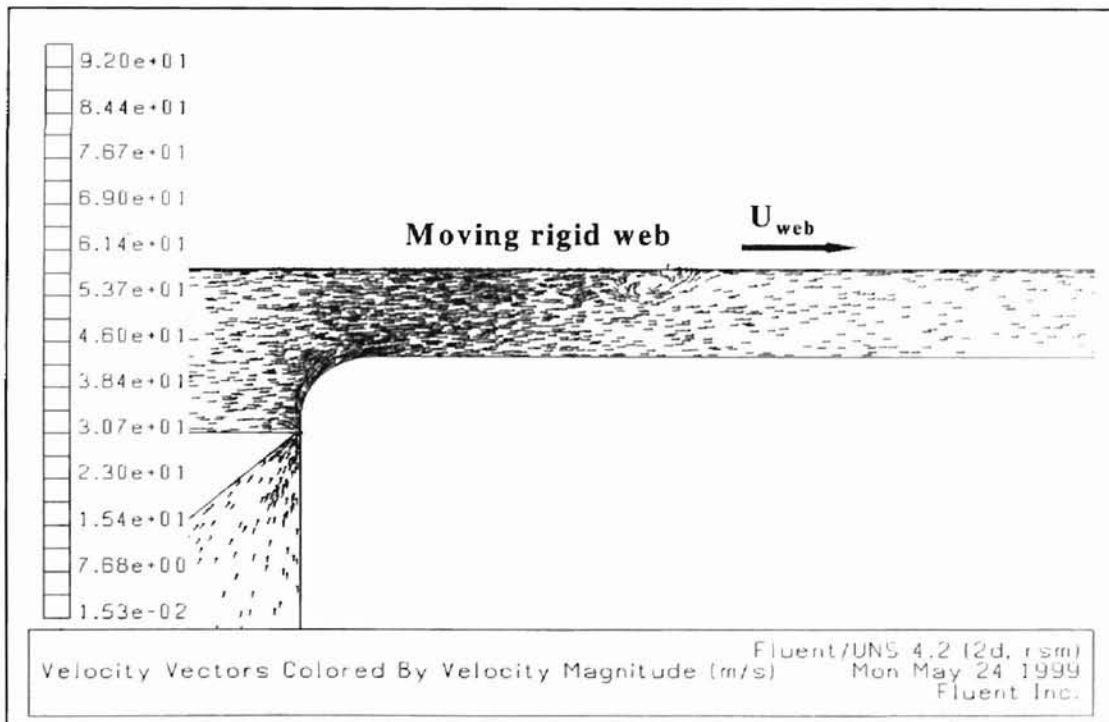
Figure 69. Velocity vectors for a moving rigid web (R = 11/64 in, s = 0.22 in, b = 0.01 in, H = 0.25 in, p_o = 1 psig, U_{web} = 0 ft/min)

70
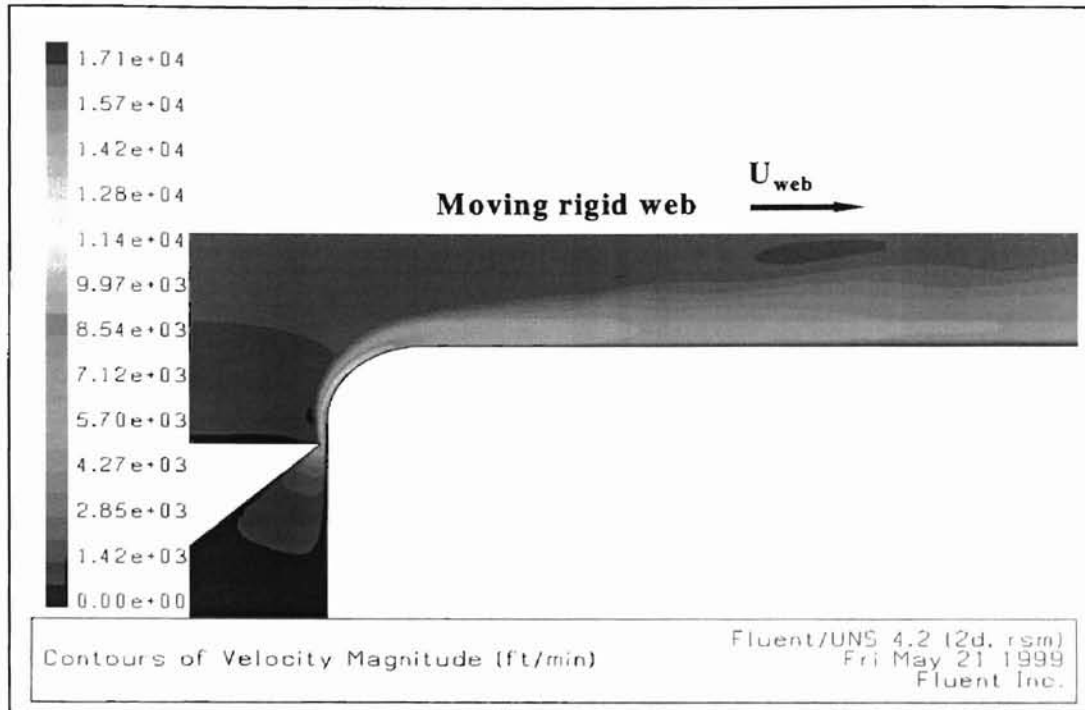
Figure 70. Velocity contours for a moving rigid web (R = 11/64 in, s = 0.22 in, b = 0.01 in, H = 0.25 in, p_o = 1 psig, U_{web} = 2000 ft/min)
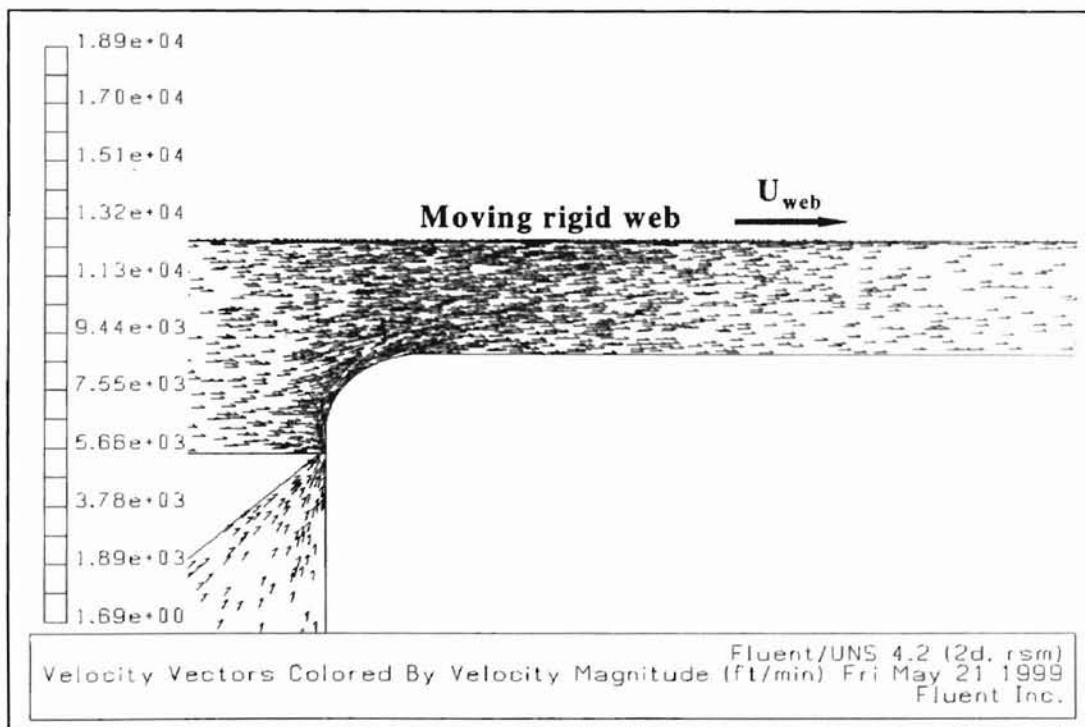
Figure 71. Velocity vectors for a moving rigid web (R = 11/64 in, s = 0.22 in, b = 0.01 in, H = 0.25 in, p_o = 1 psig, U_{web} = 2000 ft/min)
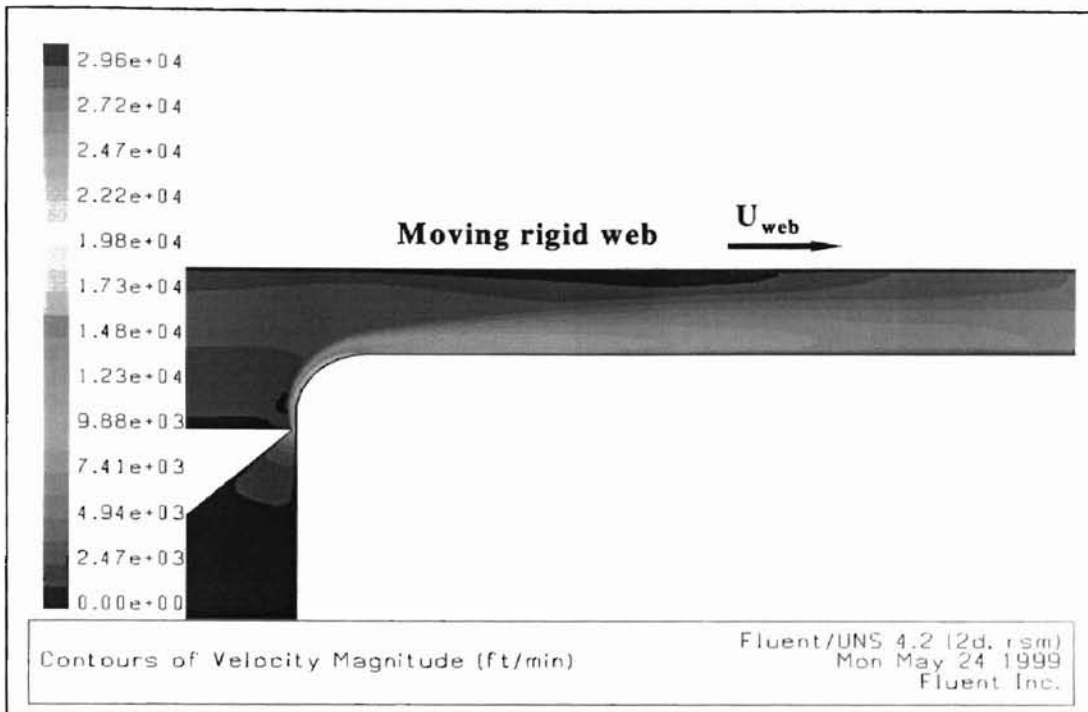
Figure 72. Velocity contours for a moving rigid web (R = 11/64 in, s = 0.22 in, b = 0.01 in, H = 0.25 in, p_o = 3 psig, U_{web} = 0 ft/min)
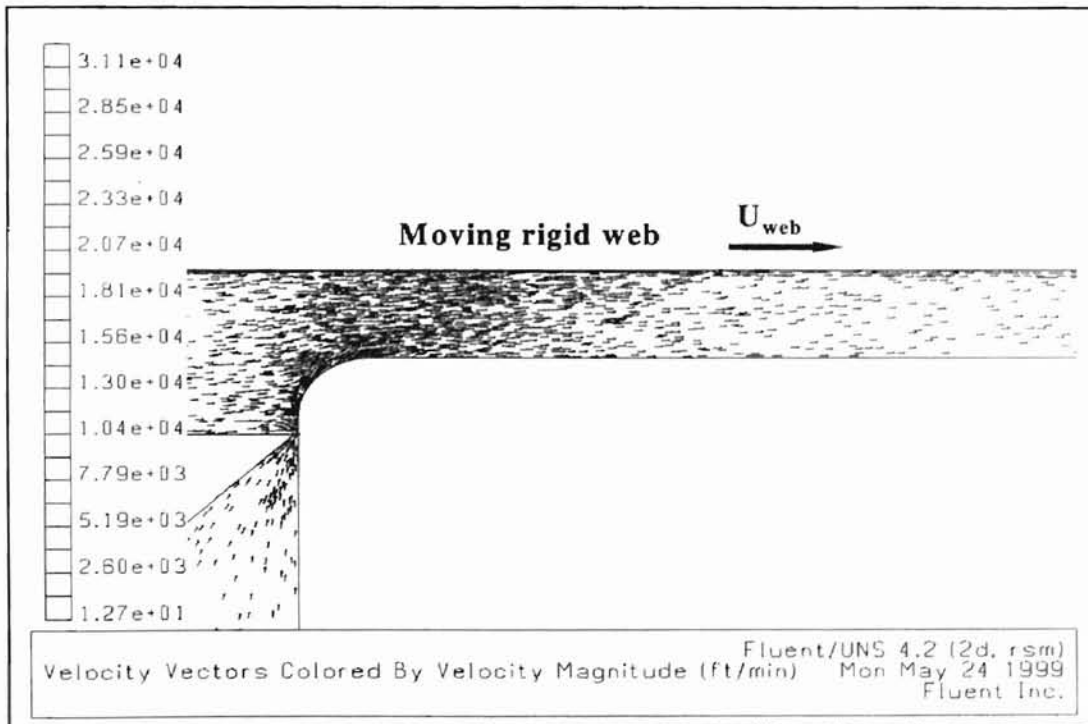
Figure 73. Velocity vectors for a moving rigid web (R = 11/64 in, s = 0.22 in, b = 0.01 in, H = 0.25 in, p_o = 3 psig, U_{web} = 0 ft/min)
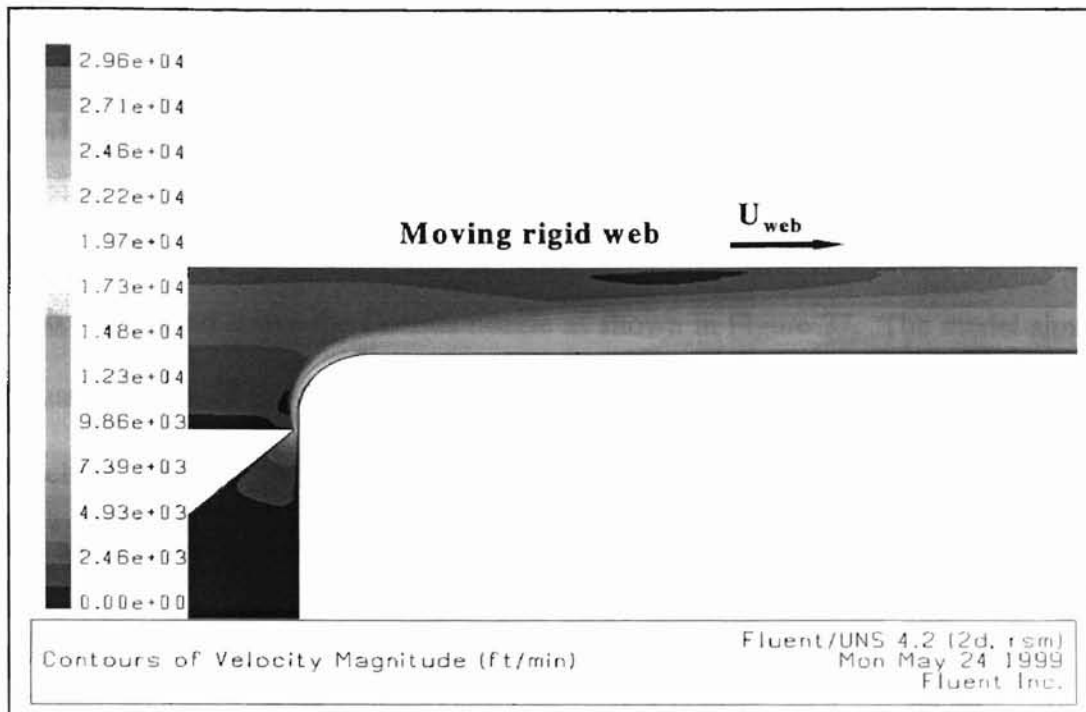
Figure 74. Velocity contours for a moving rigid web (R = 11/64 in, s = 0.22 in, b = 0.01 in, H = 0.25 in, p₀ = 3 psig, U_web = 2000 ft/min)
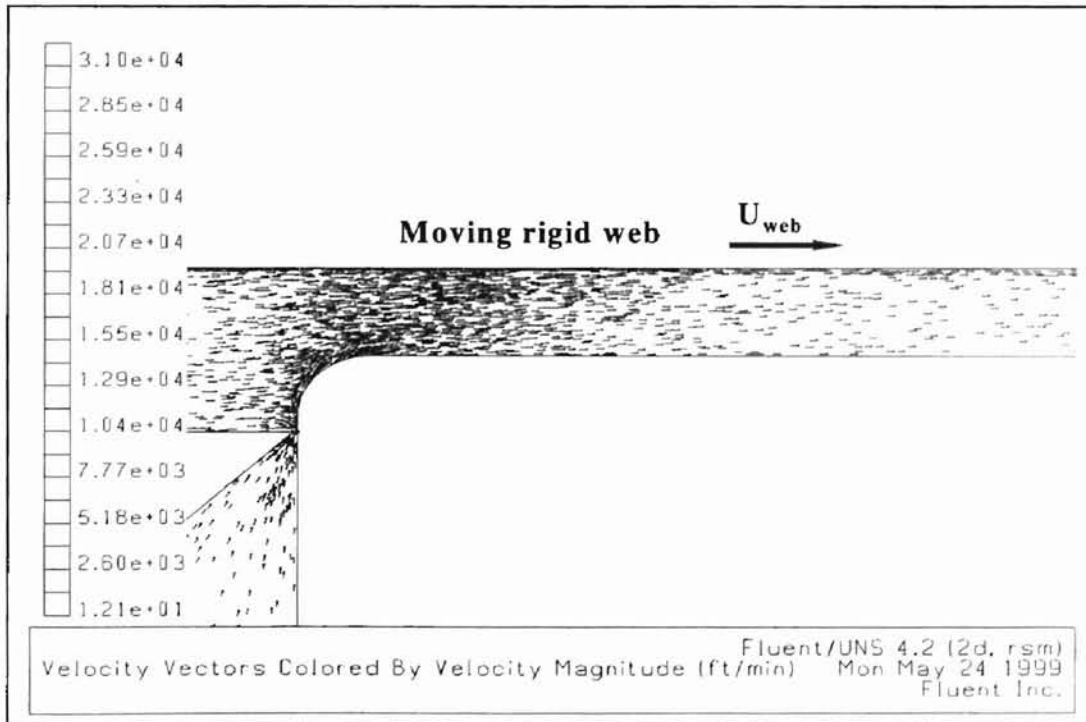
Figure 75. Velocity vectors for a moving rigid web (R = 11/64 in, s = 0.22 in, b = 0.01 in, H = 0.25 in, p₀ = 3 psig, U_web = 2000 ft/min)

73

4.4 Coanda Air Jet and a Stationary Flexible Web

4.4.1 Description of the computational model

The computational model for a flexible web is shown in Figure 76. A flexible web was placed above the Coanda nozzle as shown in Figure 77. The model simulates a situation in which the Coanda air jet is used for generating the aerodynamic traction in the machine direction. The right side of the pressure boundary was placed 160 inches from the air exit, and the left side of pressure boundary was placed 40 inches from the air exit.
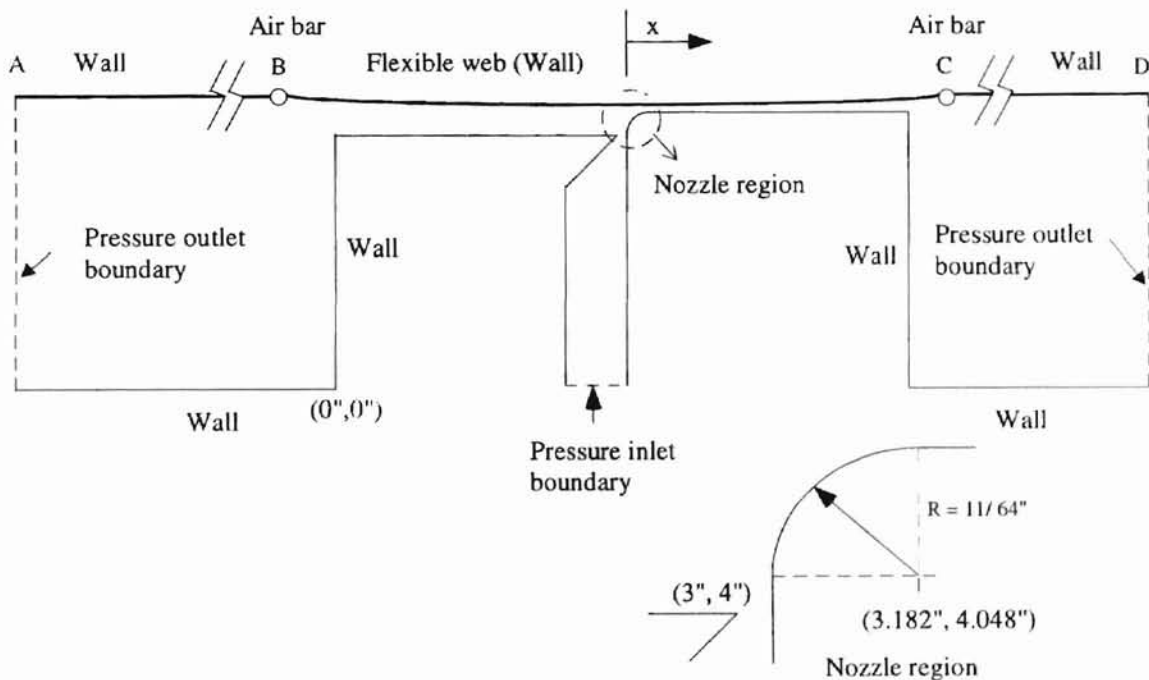
Figure 76. Computational model for flexible web

The stationary flexible web has been modeled with two boundaries which are used for supporting the web in the experiment. The web measuring 46.51 inches in length in between the two boundaries has roughness (3.1×10^{-5} inches), which is the same as that

of the web used in the experiment. The web was divided into 674 nodes on section BC. An appropriate mesh was created at the nozzle region and the region near the wall so that solutions stabilize.
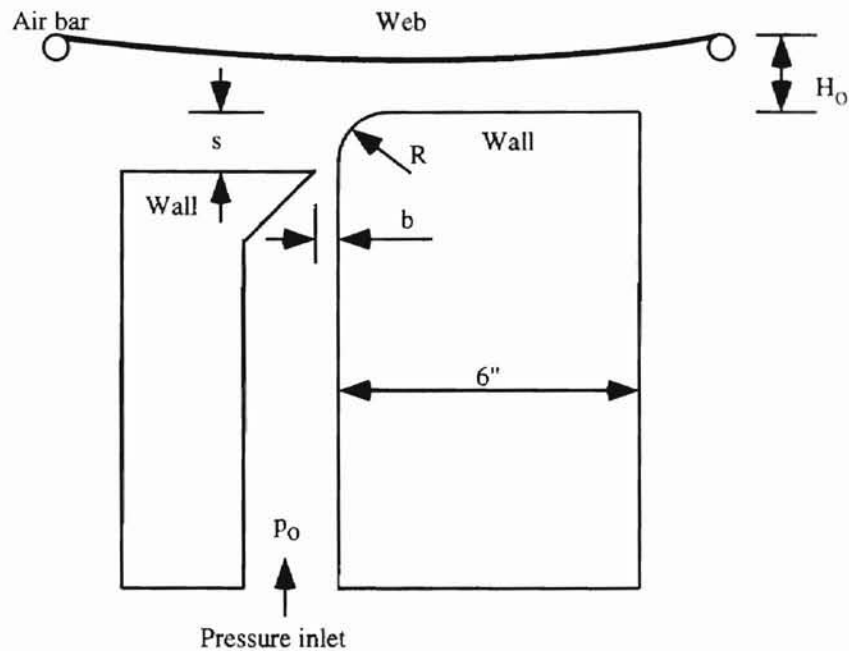
Figure 77. Schematic of the nozzle with a flexible web

Subsequent refinement evolved into an optimum mesh, appropriate for the calculation model. The final refined mesh was 38,873 nodes for the flexible web simulation. The number of iterations until convergence was around 2500 - 4000 to meet a residual value of 1×10^{-5} for this calculation.

4.4.2 Results and discussion

Pressure distribution

The effects of the web tension of a flexible web on the pressure profile are shown in Figure 78. The main effect of web tension appears as reduction of pressure on the web, especially in the region downstream of the slot nozzle.

For various applied web tensions, the dip shifts up as the applied tension is decreased. Also, the change in magnitude of the pressure peaks is inversely proportional to the applied tension. Another attribute of pressure profiles is that the dip is smoother when the applied tension is increased. Peak and dip of the pressure profiles increase and decrease with the web tension. The positive pressure will be dominant as the applied tension is decreased.

As seen in Figure 79, the lift force on the flexible web decreases with the applied tension of the web. This effect tends to disappear at higher web tensions. Examining the graph, web tension is also one of the important parameters for the equilibrium position of the web.
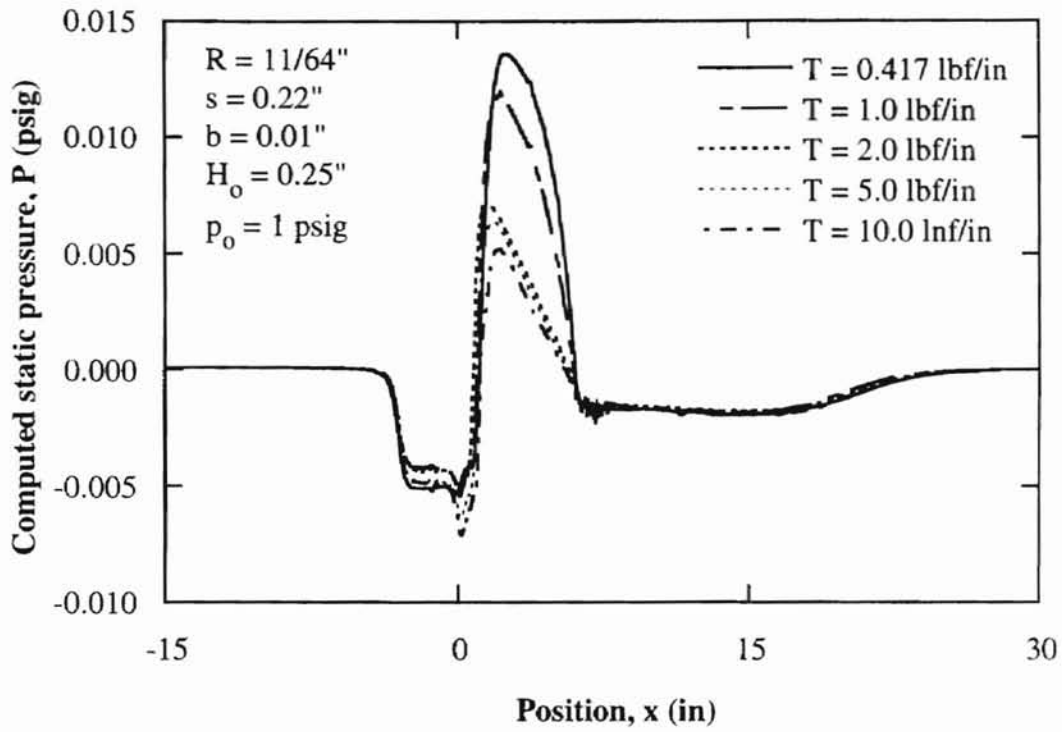
Figure 78. Effects of web tension on pressure distribution (H_o = 0.25 in)
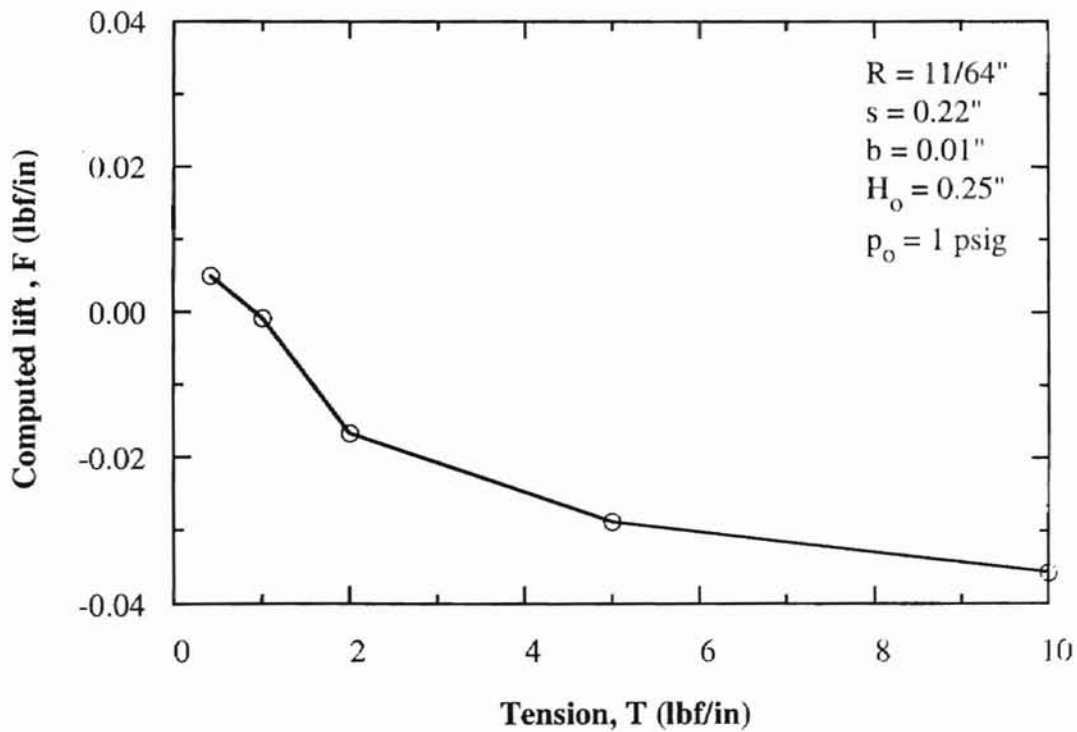
Figure 79. Effect of applied tension on lift force

Deflection profile

A flexible web can be modeled as a plate and its equilibrium equation for a flexible web can be expressed as

$$D\frac{d^4w}{ds^4} - T\frac{d^2w}{ds^2} = p_1 - p_2 \tag{1}$$

where w is the web displacement, D is the bending stiffness, T is the web tension, p_1 is the pressure on the side affected by the air jet, and p_2 is the ambient pressure. The bending stiffness is defined as

$$D = \frac{Et^3}{12(1-v^2)} \tag{2}$$

where t is the web thickness, and v is Poission's ratio.

Finite Difference Equation

Using central difference approximation, the second and fourth order terms in the governing equation can be expressed in the finite-difference form as

$$\frac{d^2W}{dS^2} = \frac{-W_{i+2} + 16W_{i+1} - 30W_i + 16W_{i-1} - W_{i-2}}{12\Delta S^2} + O(\Delta S^4) \tag{3}$$

and

$$\frac{d^4W}{dS^4} = \frac{W_{i+2} - 4W_{i+1} + 6W_i - 4W_{i-1} + W_{i-2}}{\Delta S^4} + O(\Delta S^2) \tag{4}$$

The finite-difference equation of Eq. (1) can be written as

$$\frac{D}{\Delta S^4}\left(w_{i+2} - 4w_{i+1} + 6w_i - 4w_{i-1} + w_{i-2}\right)$$
$$-\frac{T}{12\Delta S^2}\left(-w_{i+2} + 16w_{i+1} - 30w_i + 16w_{i-1} - w_{i-2}\right) = P_{1i} - P_{2i} \tag{5}$$

or

$$\left(\frac{D}{\Delta S^4} + \frac{T}{12\Delta S^2}\right)w_{i+2} - \left(\frac{4D}{\Delta S^4} + \frac{16T}{12\Delta S^2}\right)w_{i+1} + \left(\frac{6D}{\Delta S^4} + \frac{30T}{12\Delta S^2}\right)w_i$$
$$+\left(\frac{D}{\Delta S^4} + \frac{T}{12\Delta S^2}\right)w_{i-2} - \left(\frac{4D}{\Delta S^4} + \frac{16T}{12\Delta S^2}\right)w_{i-1} = P_{1i} - P_{2i} \tag{6}$$

which can be rewritten as

$$E_1 w_{i-2} + E_2 w_{i-1} + E_3 w_i + E_4 w_{i+1} + E_5 w_{i+2} = F_i \tag{7}$$

where

$$E_1 = E_5 = \frac{D}{\Delta S^4} + \frac{T}{12\Delta S^2}$$
$$E_2 = E_4 = -\left(\frac{4D}{\Delta S^4} + \frac{4T}{3\Delta S^2}\right) \tag{8}$$
$$E_3 = \frac{6D}{\Delta S^4} + \frac{5T}{2\Delta S^2}$$
$$F_i = P_{1i} - P_{2i}$$

Boundary Conditions

Two air bars were used during the experiments to support the two edges of the flexible web. The corresponding boundary conditions can be written as

$$w\big|_{S=0} = 0, \quad \frac{dw}{dS}\bigg|_{S=0} = 0, \quad w\big|_{S=L} = 0, \quad \text{and} \quad \frac{dw}{dS}\bigg|_{S=L} = 0 \tag{9}$$

The boundary conditions at the starting point for the finite-difference equation can be written as

$$w_0 = 0 \quad and \quad \frac{dw}{dS}\bigg|_{i=0} = \frac{w_1 - w_{-1}}{2\Delta S} = 0 \tag{10}$$

or

$$w_0 = 0 \quad and \quad w_1 = w_{-1} \tag{11}$$

At nodes 1 and 2,

$$\begin{aligned}
E_1 \times w_{-1} + E_2 \frac{1}{16} \times 0 + E_3 w_1 + E_4 w_2 + E_5 w_3 = F_1 \qquad &\text{node 1} \\
E_1 \times 0 + E_2 w_1 + E_3 w_2 + E_4 w_3 + E_5 w_4 = F_2 \qquad &\text{node 2}
\end{aligned} \tag{12}$$

or

$$(E_1 + E_3) w_1 + E_4 w_2 + E_5 w_3 = F_1 \qquad \text{node 1}$$

$$E_2 w_1 + E_3 w_2 + E_4 w_3 + E_5 w_4 = F_2 \qquad \text{node 2}$$

(13)

The boundary conditions at the end point are

$$w_{n+1} = 0 \quad and \quad \left. \frac{dw}{dS} \right|_{i=n+1} = \frac{(w_{n+2} - w_n)}{2\Delta S} = 0$$

(14)

or

$$w_{n+1} = 0 \quad and \quad w_{n+2} = w_n$$

(15)

At nodes n and n-1,

$$E_1 w_{n-3} + E_2 w_{n-2} + E_3 w_{n-1} + E_4 w_n + E_5 \times 0 = F_{n-1} \qquad \text{node n-1}$$

$$E_1 w_{n-2} + E_3 w_{n-1} + E_3 w_n + E_4 \times 0 + E_5 w_{n+2} = F_n \qquad \text{node n}$$

(16)

or

$$E_1 w_{n-3} + E_2 w_{n-2} + E_3 w_{n-1} + E_4 w_n = F_{n-1} \qquad \text{node } n-1$$

$$E_1 w_{n-2} + E_2 w_{n-1} + (E_3 + E_5) w_n = F_n \qquad \text{node } n$$

(17)

81

Matrix Form

The finite-difference can be rewritten in matrix form as

$$
\begin{bmatrix}
E_{1,1} & E_{1,2} & E_{1,3} & 0 & & & & & \\
E_{2,1} & E_{2,2} & E_{2,3} & E_5 & 0 & & & & \\
E_1 & E_2 & E_3 & E_4 & E_5 & 0 & & & \\
0 & . & . & . & . & . & 0 & & \\
& 0 & . & . & . & . & . & 0 & \\
& & 0 & E_1 & E_2 & E_3 & E_4 & E_5 & \\
& & & 0 & E_1 & E_{n-1,n-2} & E_{n-1,n-1} & E_{n-1,n} & \\
& & & & 0 & E_{n,n-2} & E_{n,n-1} & E_{n,n} &
\end{bmatrix}
\begin{bmatrix}
w_1 \\ w_2 \\ w_3 \\ . \\ . \\ w_{n-2} \\ w_{n-1} \\ w_n
\end{bmatrix}
=
\begin{bmatrix}
F_1 \\ F_2 \\ F_3 \\ . \\ . \\ F_{n-2} \\ F_{n-1} \\ F_n
\end{bmatrix}
\qquad (18)
$$

where

$$
E_{1,1} = E_1 + E_3 = \left(\frac{D}{\Delta S^4} + \frac{T}{12\Delta S^2} \right) + \left(\frac{6D}{\Delta S^4} + \frac{5T}{2\Delta S^2} \right) = \frac{7D}{\Delta S^4} + \frac{31}{12}\frac{T}{\Delta S^2}
$$

$$
E_{1,2} = E_4 = -\left(\frac{4D}{\Delta S^4} + \frac{4T}{3\Delta S^2} \right)
$$

$$
E_{1,3} = E_5 = \left(\frac{D}{\Delta S^4} + \frac{T}{12\Delta S^2} \right)
$$

$$
E_{2,1} = E_2 = -\left(\frac{4D}{\Delta S^4} + \frac{4T}{3\Delta S^2} \right)
\qquad (19)
$$

$$
E_{2,2} = E_3 = \left(\frac{6D}{\Delta S^4} + \frac{5T}{2\Delta S^2} \right)
$$

$$
E_{2,3} = E_4 = -\left(\frac{4D}{\Delta S^4} + \frac{4T}{3\Delta S^2} \right)
$$

and

$$E_{n-1,n-2} = E_2 = -\left(\frac{4D}{\Delta S^4} + \frac{4T}{3\Delta S^2}\right)$$

$$E_{n-1,n-1} = E_3 = \left(\frac{6D}{\Delta S^4} + \frac{5T}{2\Delta S^2}\right)$$

$$E_{n-1,n} = E_4 = -\left(\frac{4D}{\Delta S^4} + \frac{4T}{3\Delta S^2}\right)$$

$$E_{n,n-2} = E_1 = \left(\frac{D}{\Delta S^4} + \frac{T}{12\Delta S^2}\right)$$

$$E_{n,n-1} = E_2 = -\left(\frac{4D}{\Delta S^4} + \frac{4T}{3\Delta S^2}\right)$$

$$E_{n,n} = E_3 + \frac{15}{8}E_4 = \left(\frac{6D}{\Delta S^4} + \frac{5T}{2\Delta S^2}\right) + \left(\frac{D}{\Delta S^4} + \frac{T}{12\Delta S^2}\right) = \frac{7D}{\Delta S^4} + \frac{31}{12}\frac{T}{\Delta S^2}$$

Once the pressure distribution (gage pressure) and web tension are known, the out-of-plane deflection profile of the web can be obtained using Eq. (1). The code to obtain the deflection profile of the web is attached in the Appendix.

Figure 80 shows one of the examples of the convergence step to obtain the deflection profile of the web. Calculation started with the flat rigid web profile. Once the gage pressure on the web is known, an out-of-plane web profile can be obtained using the code corresponding to the applied tension. Then, the deflection profile was fit to new geometry in FLUENT/UNS. New static gage pressure on the web is determined from the calculation in FLUENT/UNS. This is one step in obtaining the deflection profile. This process is conducted by continued repetition until the convergence of the deflection profile. At a lower case of tension, many calculation steps are needed to perform this work. For example, 27 calculation steps were required to obtain the converged deflection profile in case of 0.417 lbf/in tension: 3 times for 10 lbf/in, 9 times for 5 lbf/in, and 8 times for 2 lbf/in. For the case of 5 lbf/in, calculation started with the deflection profile

which was found at web tension of 10 lbf/in. Such repetition can be used for the iteration problem.
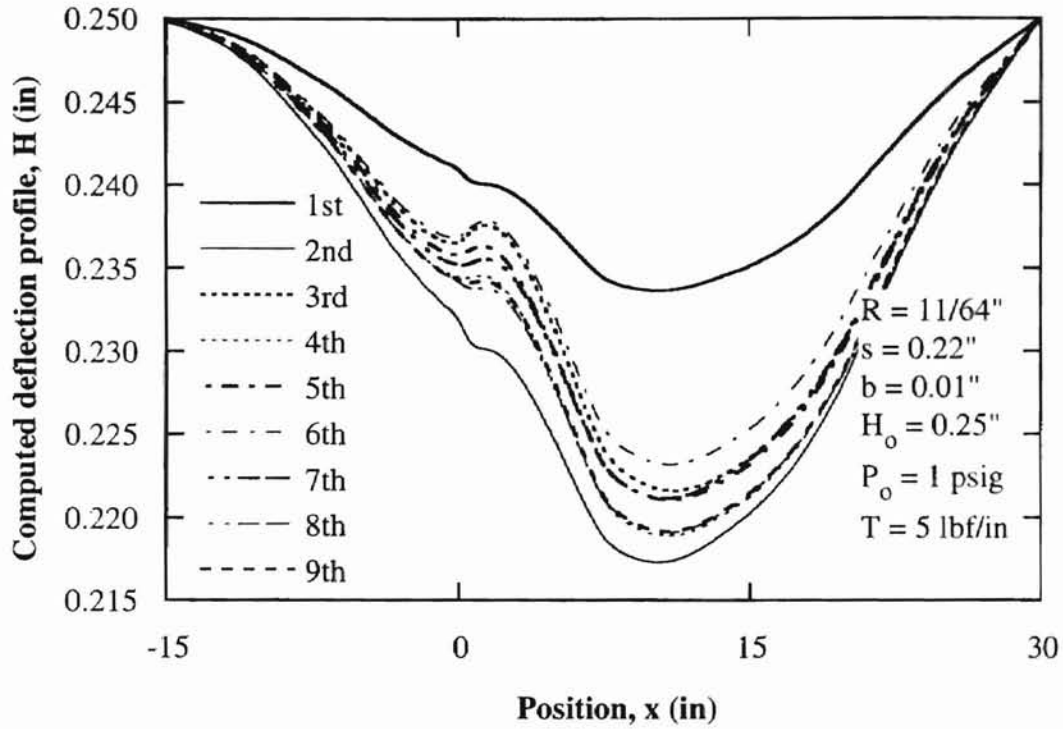
Figure 80. Deflection profile of the web (T = 5 lbf/in)

Several deflection profiles at each applied tension are shown in Figure 81. Looking at the deflection profile of the web for various applied web tensions, the deflection profile visibly drops near the top of the nozzle. Comparing the deflection profiles for different applied tensions, more web flexibility of the web is seen as the applied web tension is decreased. Considering the scale of y-axis to x-axis, the deflection profiles are almost flat even for the lowest case of tension (T = 0.417 lbf/in).
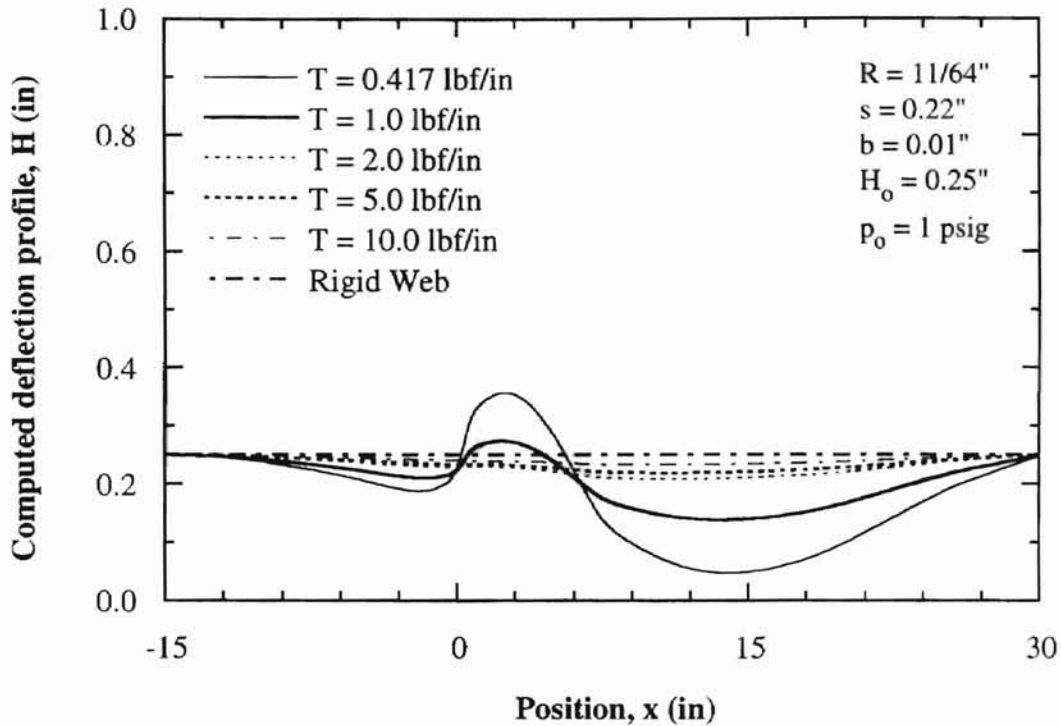
Figure 81. Deflection profile of the flexible web for different applied tensions

Aerodynamic friction force on the web

Wall shear stress profiles are shown in Figure 82. This figure reveals that there are two peaks of the wall shear stress; they occur before and right after the slot nozzle. As expected, compared with other regions a large peak in shear stress occurred after the air exit. Also, it is seen that the shear stress gradually decreases to zero while moving away from the slot nozzle.

Almost the same trend of curves is seen for the wall shear stress profile in this flexible simulation for the high applied web tensions. The same kind of magnitude of shear stress peaks are seen for the high applied tensions (2 and 5 lbf/in) near the slot nozzle. Note that the shear stress peak at the air exit seems to disappear for the low tension case of 0.417 lbf/in, which means that traction for the low web tension will be

smaller than that of high tension cases.
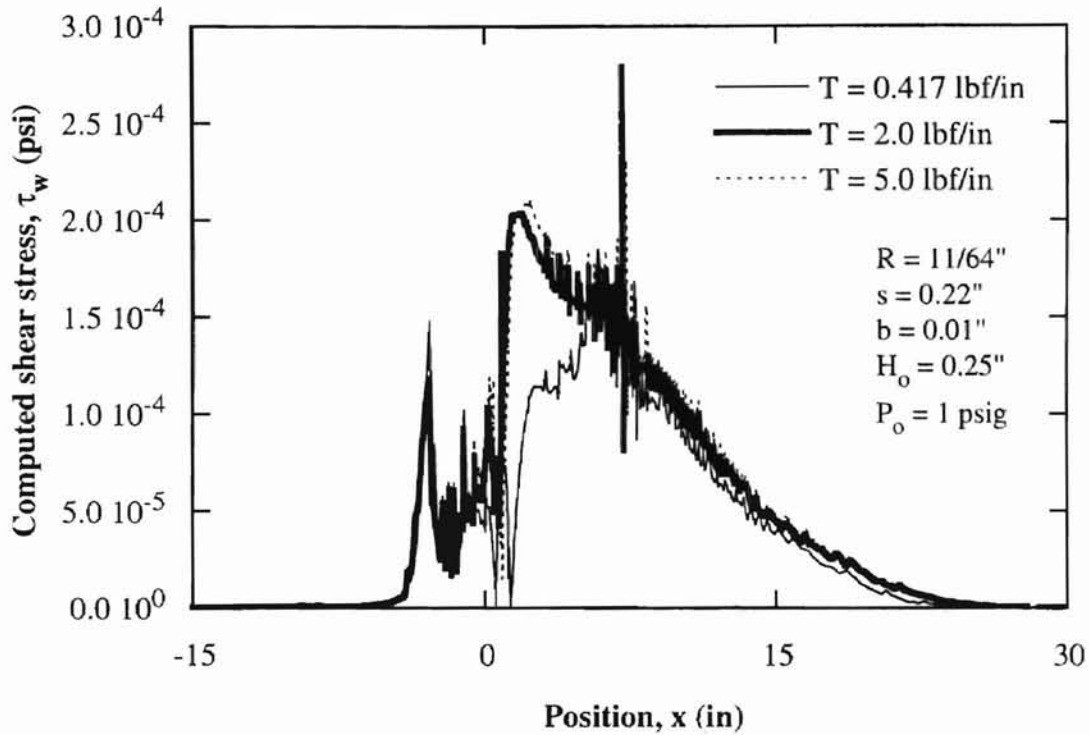
Figure 82. Distribution of wall shear stress on the flexible web

Integrating the wall shear stress over the web (Section BC) gives the traction acting on the web per unit width. The trapezoidal rule was used to perform this integration over the web. As seen in Figure 83, traction force on the flexible web increases with the applied tension of the web. This effect tends to disappear at high web tensions. If the applied tension on the web is increased, a web subjected to the Coanda air jet is more stable and a larger traction on the web can be generated; however, there is a limit in the tension as shown in Figure 83. The results have been tabulated in Table 6. The force acting on the web increases as shown in the table.
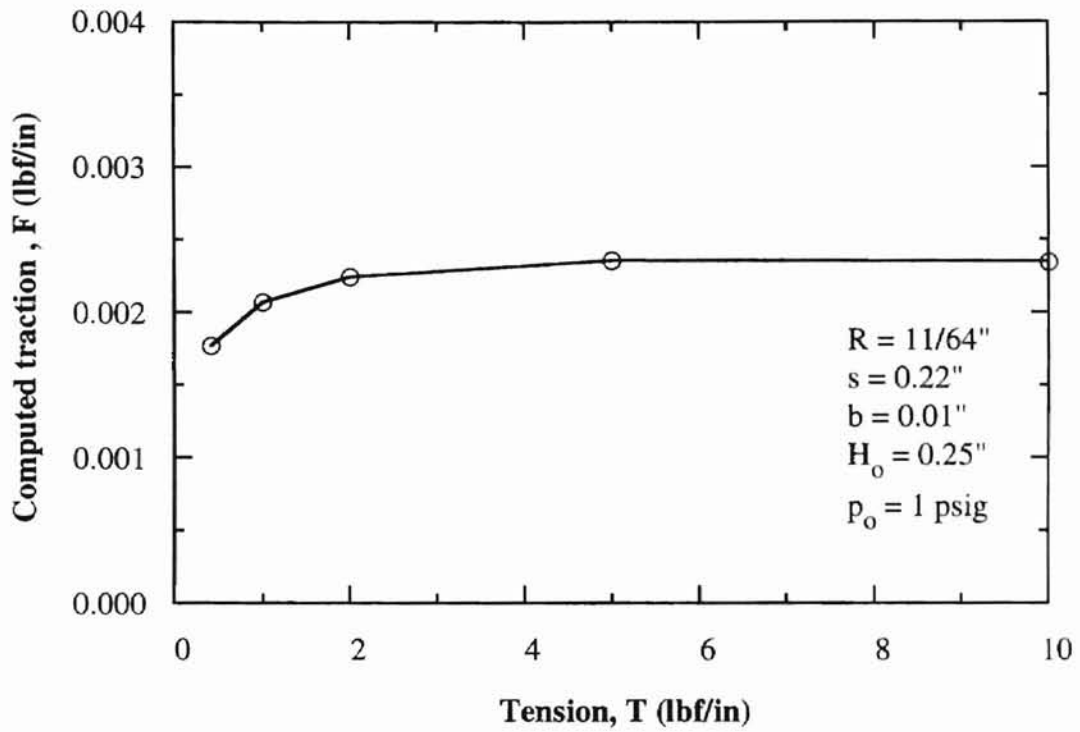
Figure 83. Effect of applied tension on traction
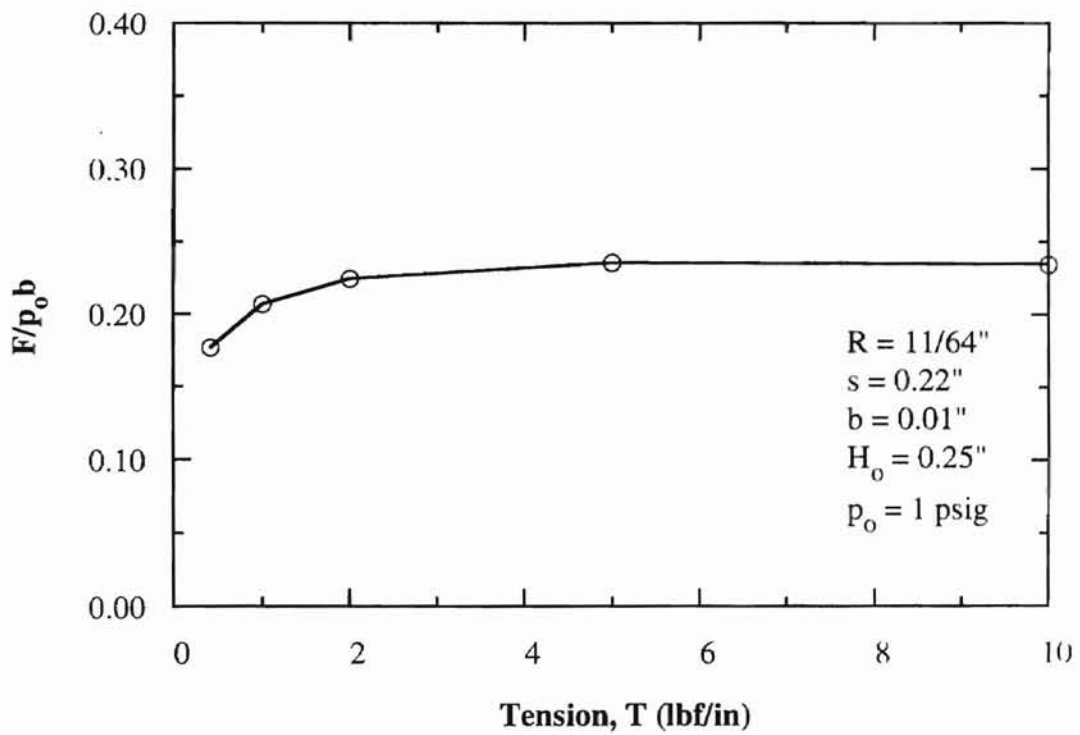
Figure 84. Effect of applied tension on non-dimensional traction

Table 6. Aerodynamic traction on the stationary flexible web for various web tensions

Web tension, (lbf/in)	Aerodynamic traction, (lbf/in)
0.417	0.0017665
1	0.0020724
2	0.0022445
5	0.0023583
10	0.0023410

Figure 85 to Figure 94 show the flow pattern in the nozzle region for various applied web tensions. Note the recirculation in the flow was created due to the interaction between the flexible web and entrained air and the mainstream when the applied tension of web was 0.417 lbf/in (p_o = 1 psig). In this recirculation region, velocity of flow was nearly zero as shown in contours of velocity and velocity vectors (Figure 85 and Figure 86). As the applied web tension increased, this vortex disappeared.

In Figure 85, the stagnation zone of velocity was observed widely on the web, but it almost disappeared with increased web tension (Figure 89, Figure 91, and Figure 93). The entrained air separates into three layers in the flow, which is caused by the high web tensions (T = 5 lbf/in and T = 10 lbf/in) in Figure 91 and Figure 93.

For all the cases the air jet was always attached to the surface of the curved block and air entrainment was also clearly seen in all the figures.
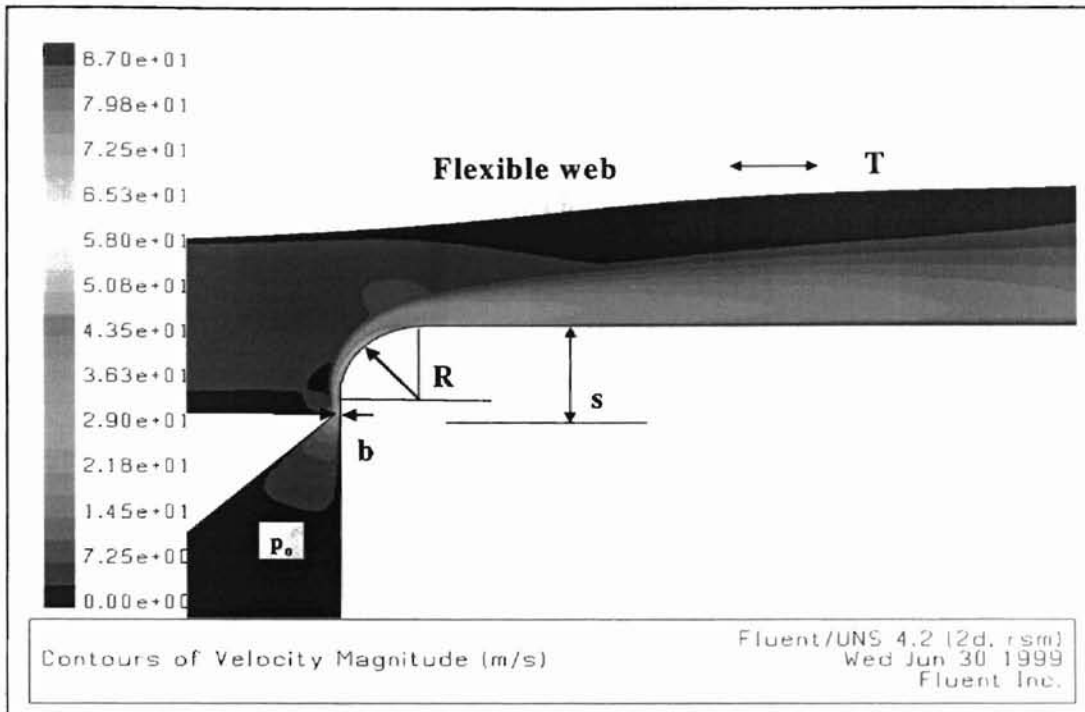
Figure 85. Velocity contours for a stationary flexible web (R = 11/64 in, s = 0.22 in, b = 0.01 in, H_o = 0.25 in, p_o = 1 psig, T = 0.417 lbf/in)
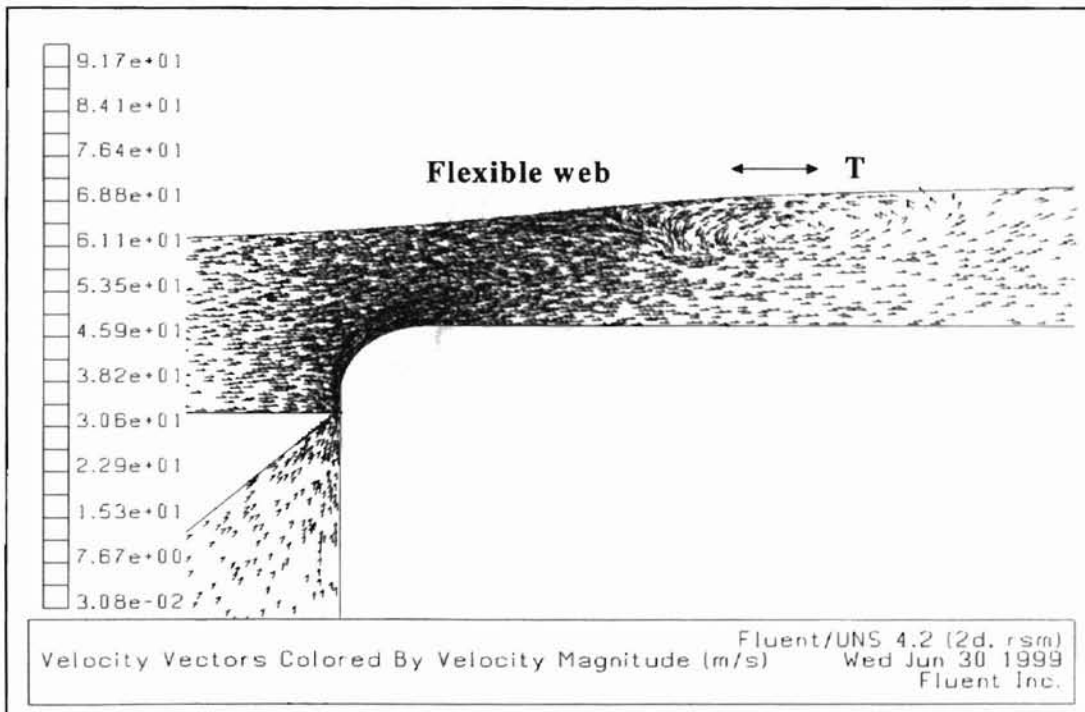
Figure 86. Velocity vectors for a stationary flexible web (R = 11/64 in, s = 0.22 in, b = 0.01 in, H_o = 0.25 in, p_o = 1 psig, T = 0.417 lbf/in)
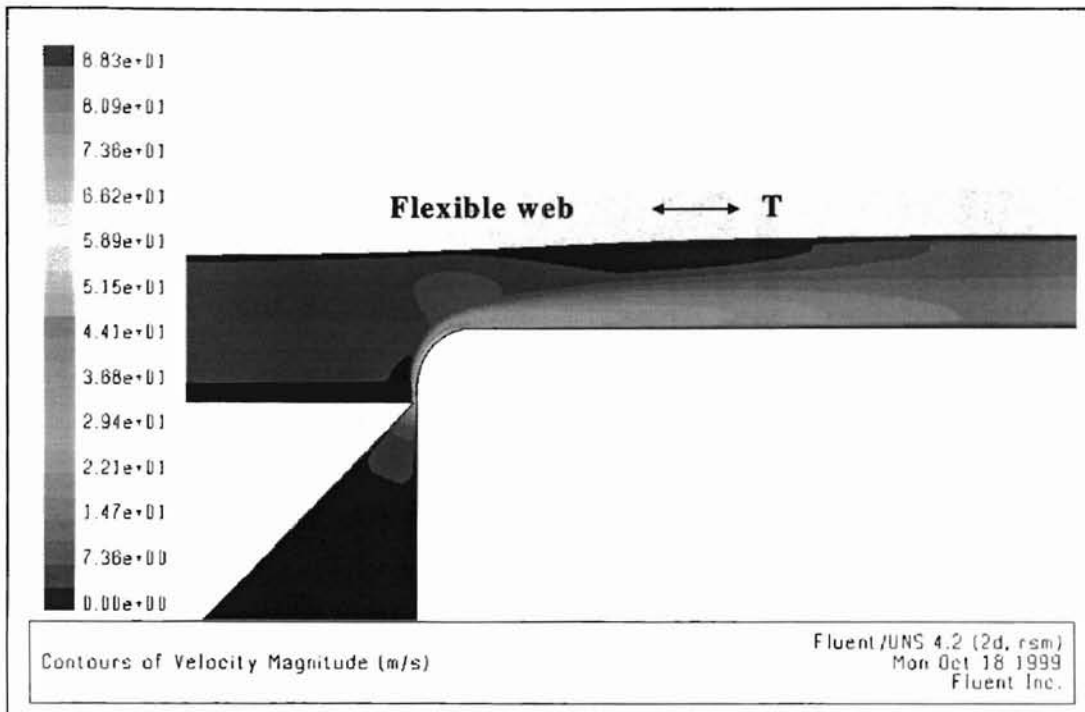
Figure 87. Velocity contours for a stationary flexible web (R = 11/64 in, s = 0.22 in, b = 0.01 in, H_o = 0.25 in, p_o = 1 psig, T = 1 lbf/in)
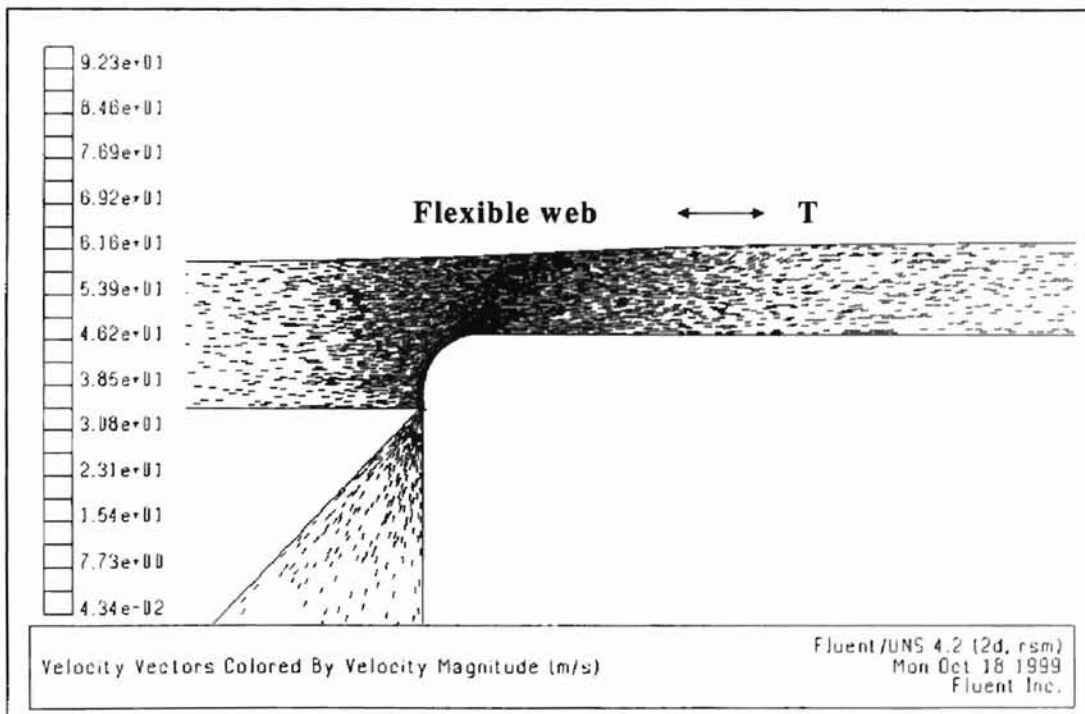
Figure 88. Velocity vectors for a stationary flexible web (R = 11/64 in, s = 0.22 in, b = 0.01 in, H_o = 0.25 in, p_o = 1 psig, T = 1 lbf/in)
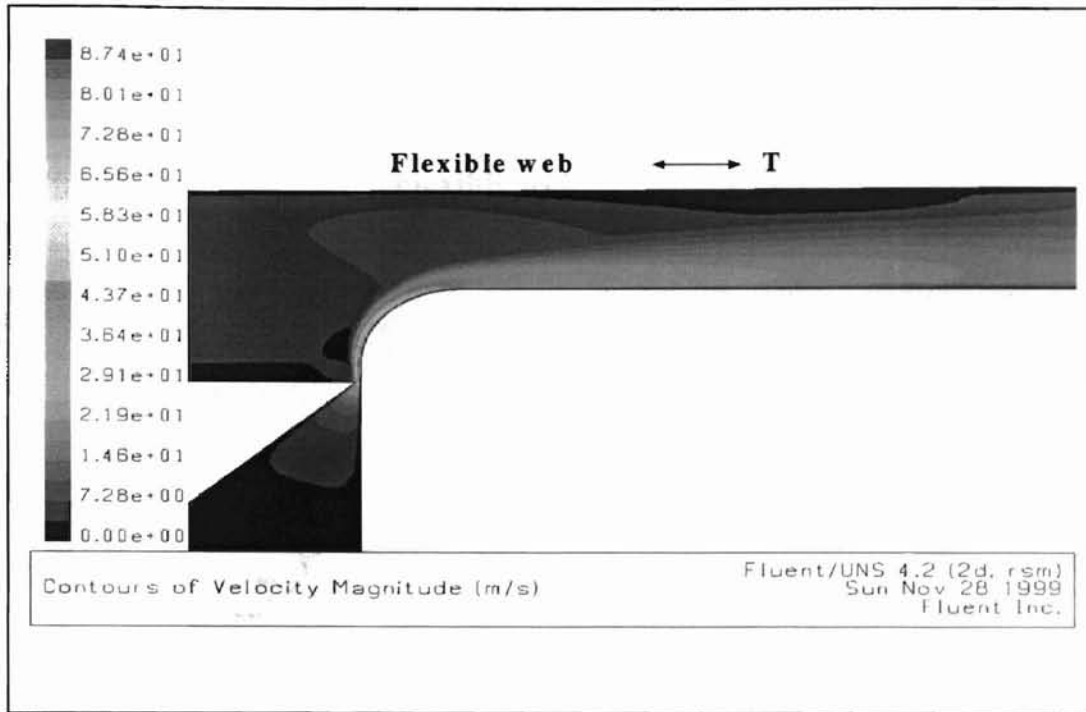
Figure 89. Velocity contours for a stationary flexible web (R = 11/64 in, s = 0.22 in, b = 0.01 in, H_o = 0.25 in, p_o = 1 psig, T = 2 lbf/in)
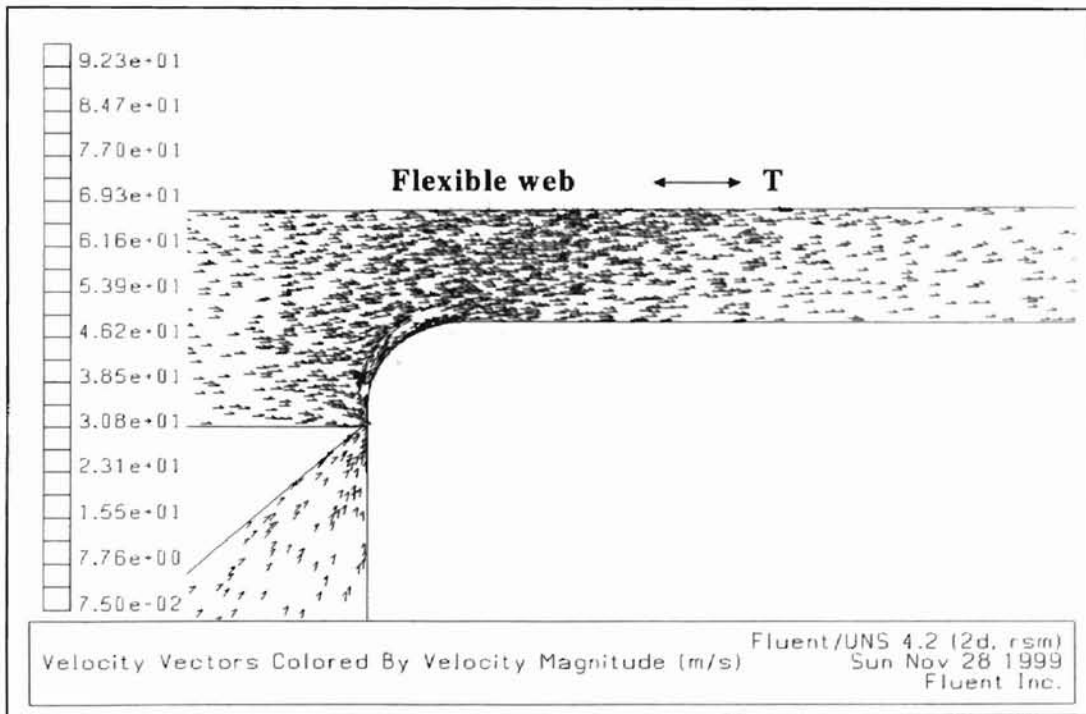
Figure 90. Velocity vectors for a stationary flexible web (R = 11/64 in, s = 0.22 in, b = 0.01 in, H_o = 0.25 in, p_o = 1 psig, T = 2 lbf/in)
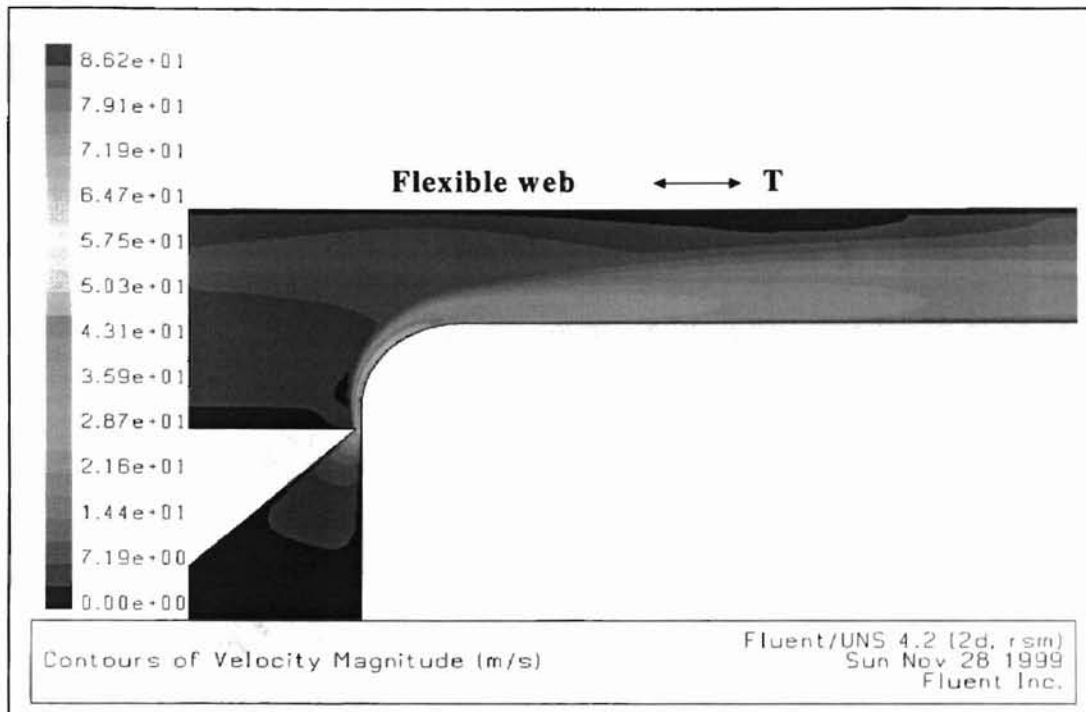
Figure 91. Velocity contours for a stationary flexible web (R = 11/64 in, s = 0.22 in, b = 0.01 in, H$_o$ = 0.25 in, p$_o$ = 1 psig, T = 5 lbf/in)
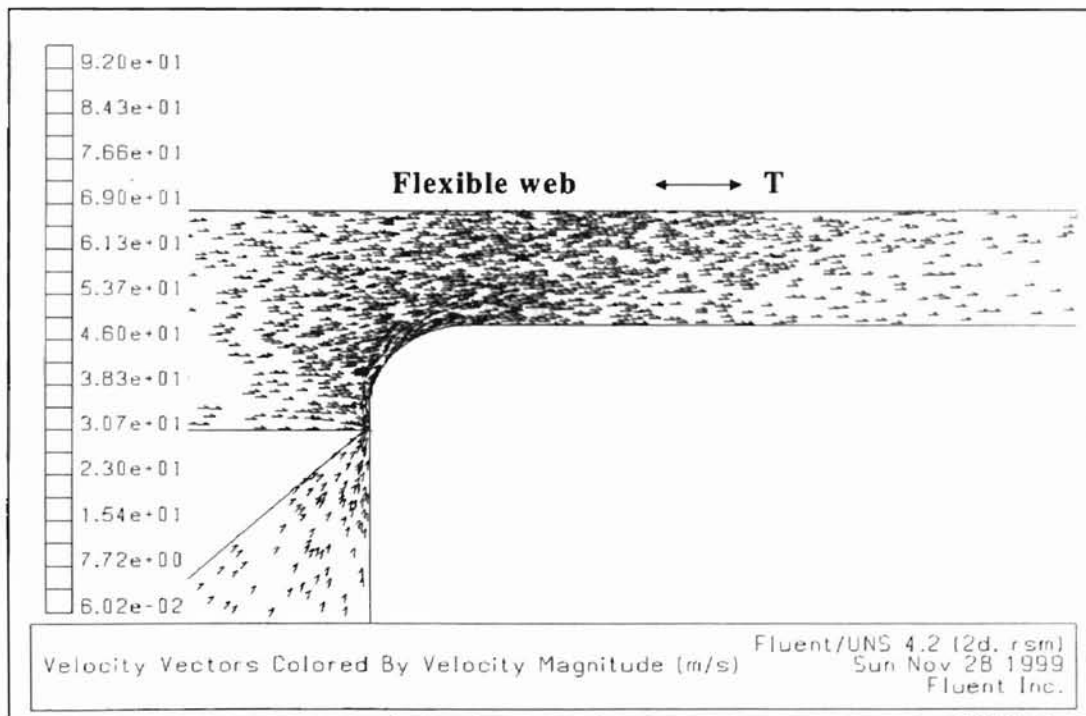
Figure 92. Velocity vectors for a stationary flexible web (R = 11/64 in, s = 0.22 in, b = 0.01 in, H$_o$ = 0.25 in, p$_o$ = 1 psig, T = 5 lbf/in)
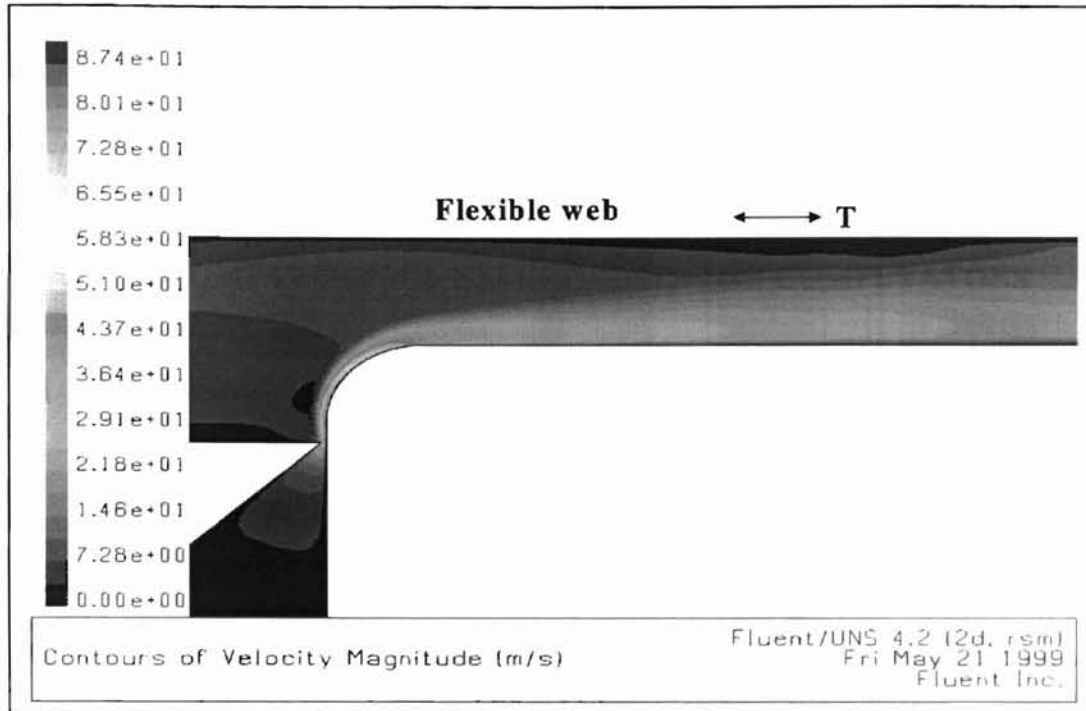
Figure 93. Velocity contours for a stationary flexible web (R = 11/64 in, s = 0.22 in, b = 0.01 in, H_o = 0.25 in, p_o = 1 psig, T = 10 lbf/in)
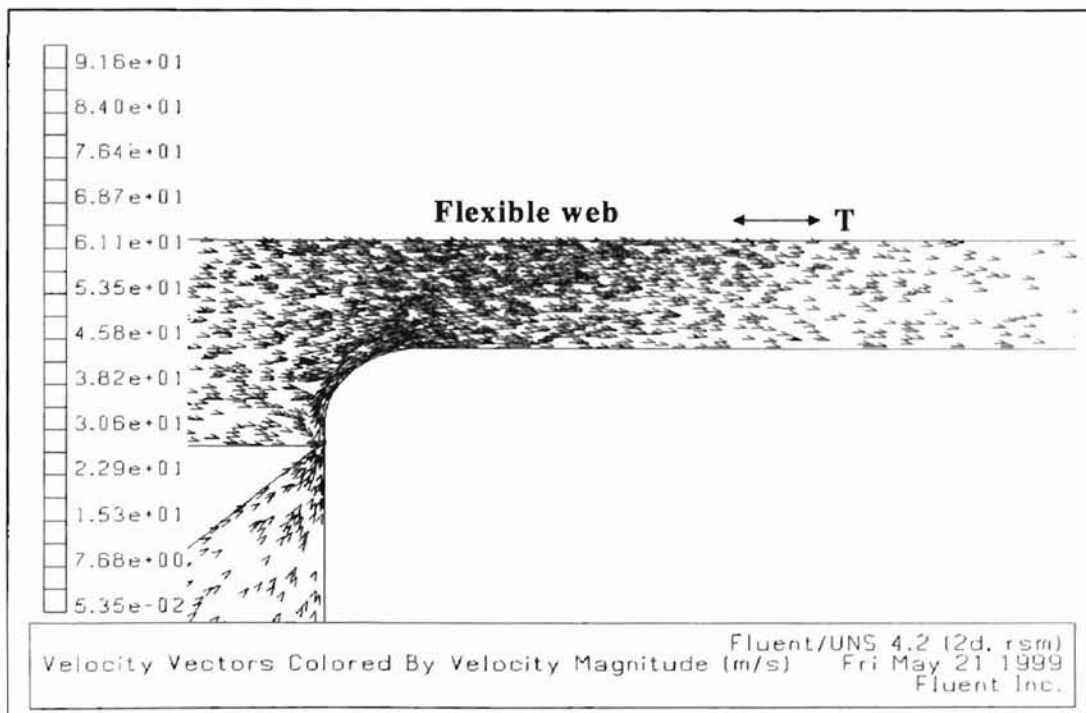
Figure 94. Velocity vectors for a stationary flexible web (R = 11/64 in, s = 0.22 in, b = 0.01 in, H_o = 0.25 in, p_o = 1 psig, T = 10 lbf/in)

CHAPTER V

COMPARISON OF EXPERIMENTS AND COMPUTATONS

5.1 Aerodynamic Forces on a Rigid Web

The computed pressure profile on the rigid web is compared with the measured profile for the floatation height of H = 0.25" in Figure 95. The two results show a similar trend, but the computed static pressures tend to be higher than the measured values. The discrepancy between the computed and measured pressure profile appears to be increased when the floatation is H = 0.15" Figure 96.

One possible reason for the discrepancy between the computed and measured pressure profile is the experimental error caused by the machine-direction tilting. As seen in Figure 97, the computed pressure profile on the web is very sensitive to the lift angle. Therefore, it is believed that a small error in the machine-direction lift angle is one of the major causes of these discrepancies.
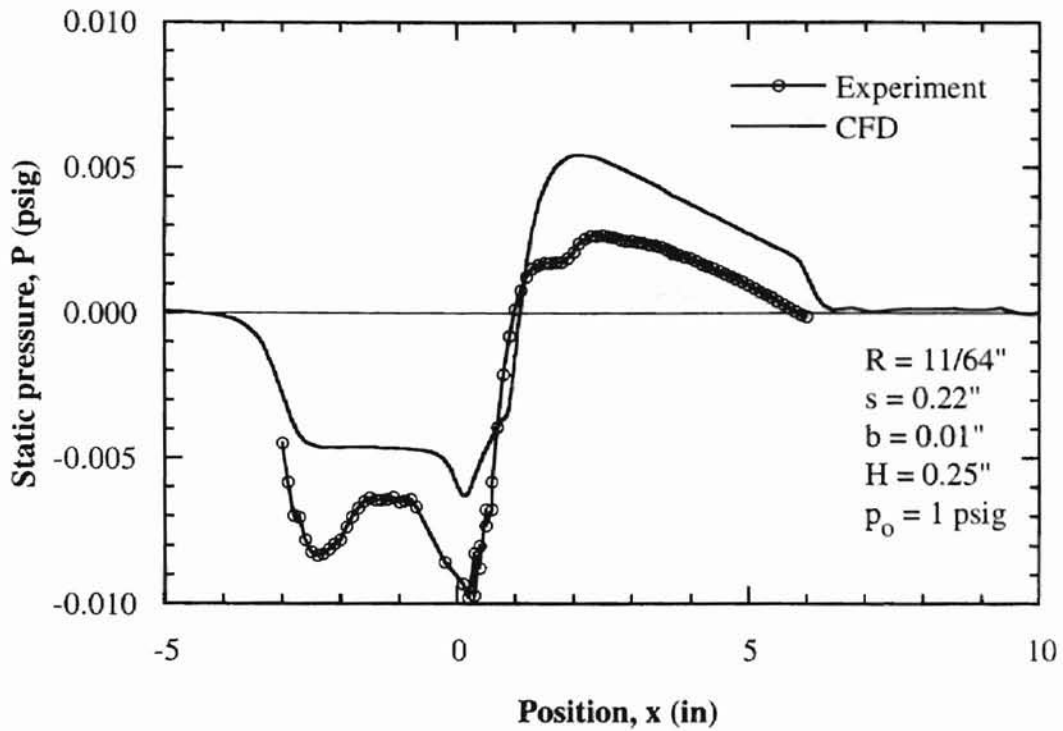
Figure 95 Comparison of pressure profile on the rigid web (H = 0.25 in)
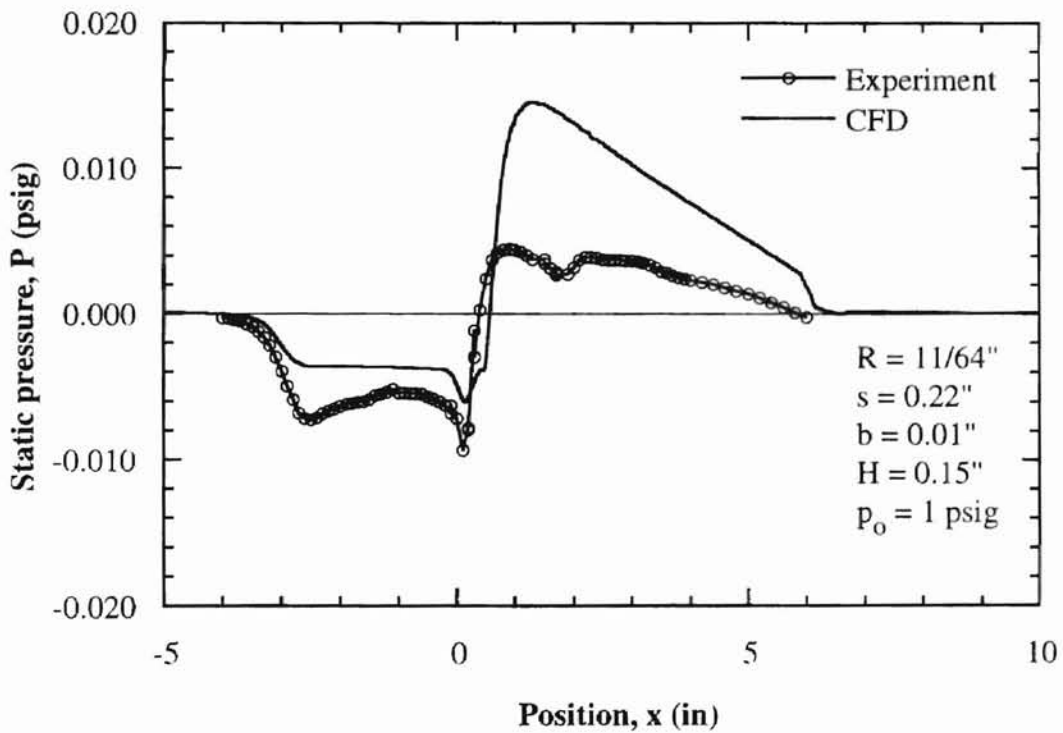
Figure 96. Comparison of pressure profile on the rigid web (H = 0.15 in)
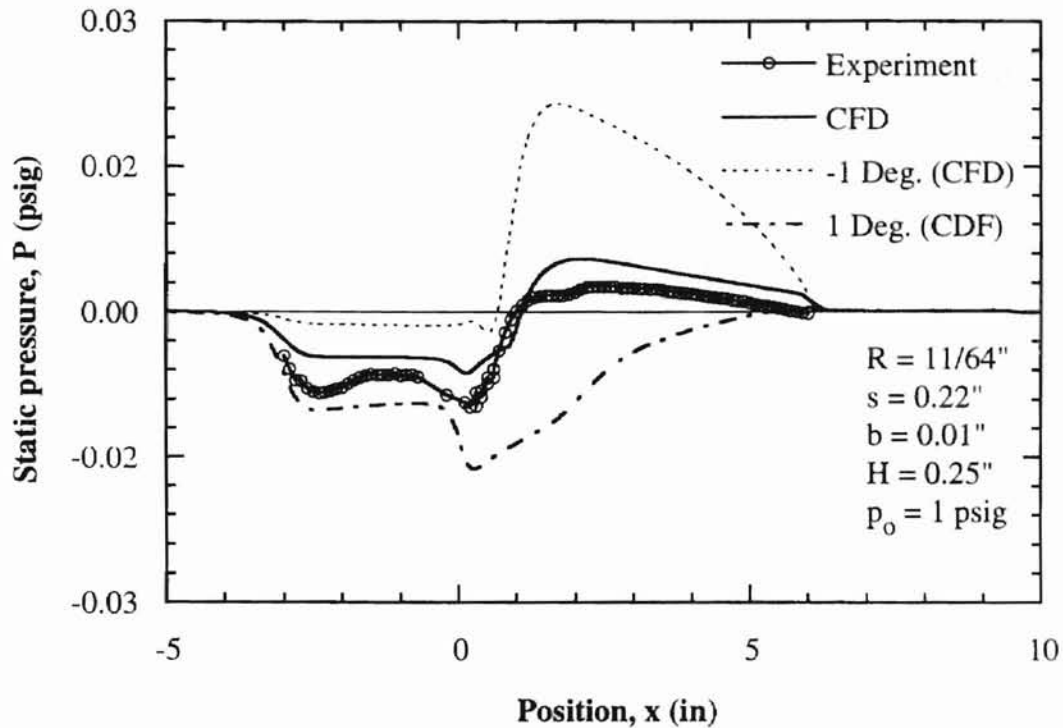
Figure 97. Comparison of pressure profile with an inclined rigid web

For the floatation height of H = 0.20", the computation appears to predict the traction on the rigid web reasonably well within the range of calculation (Figure 98 and Figure 99). When the floatation height was increased to H = 0.25", the computation overpredicts the traction (Figure 100 and Figure 101). The non-dimensional traction ($F/p_o b$) on the rigid web for H = 0.20" was around 0.2 and the non-dimensional traction for H = 0.25" was between 0.1 and 0.2.
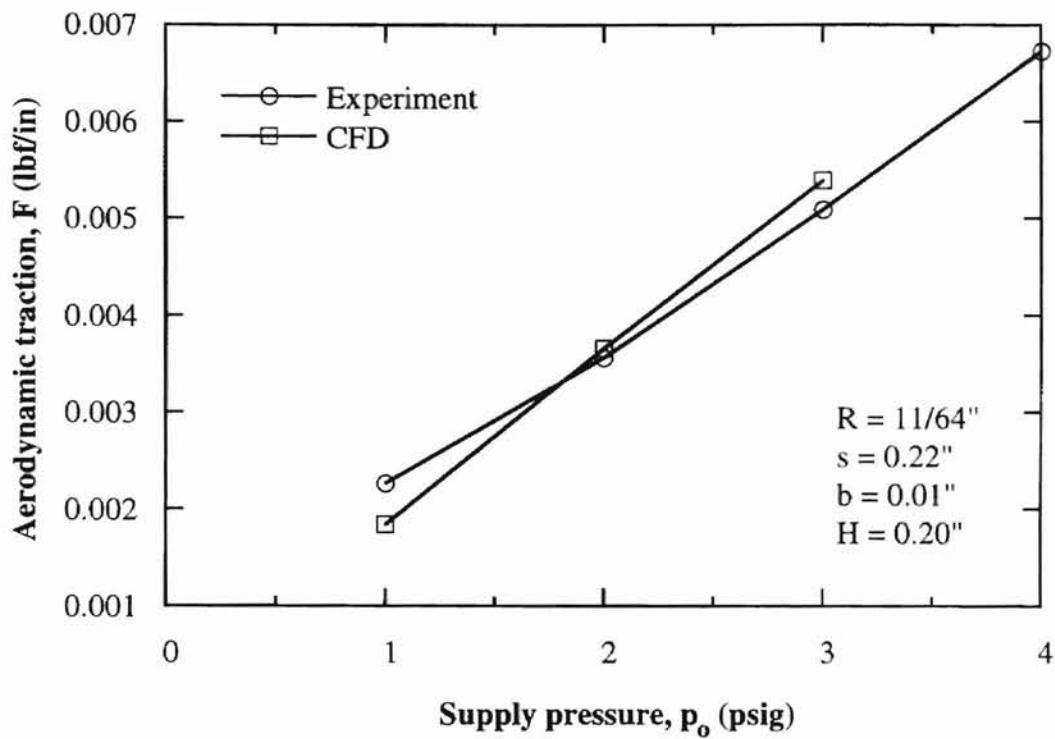
Figure 98. Comparison of traction on the rigid web (H = 0.20 in)
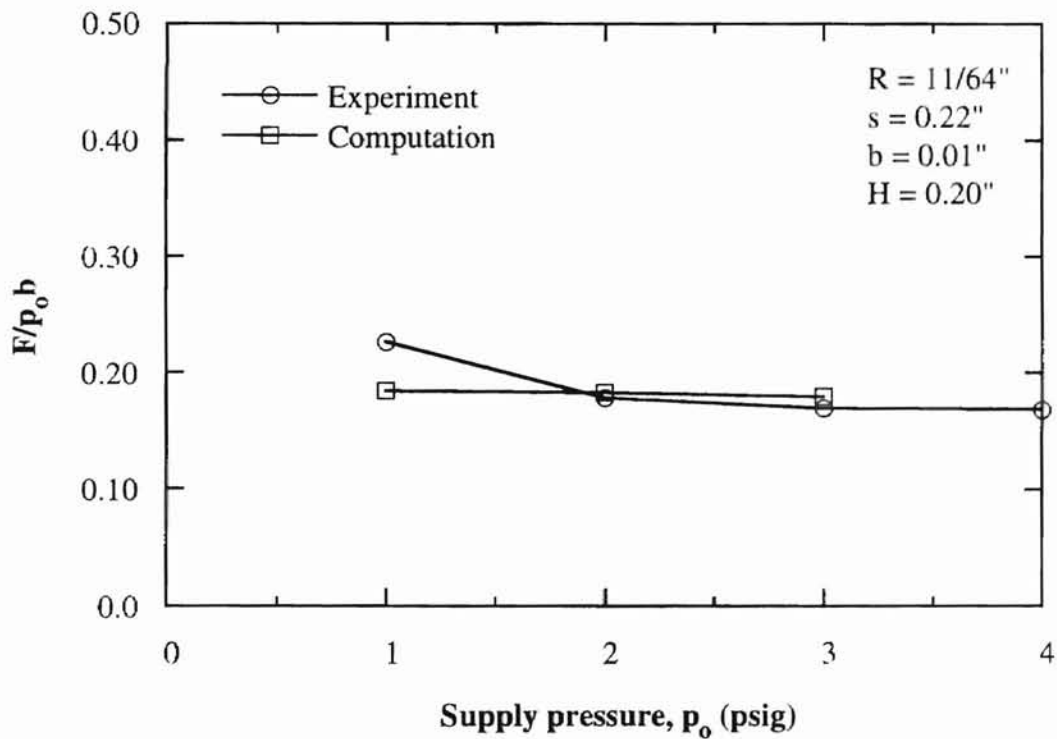
Figure 99. Comparison of non-dimensional traction on the rigid web (H = 0.20 in)

97
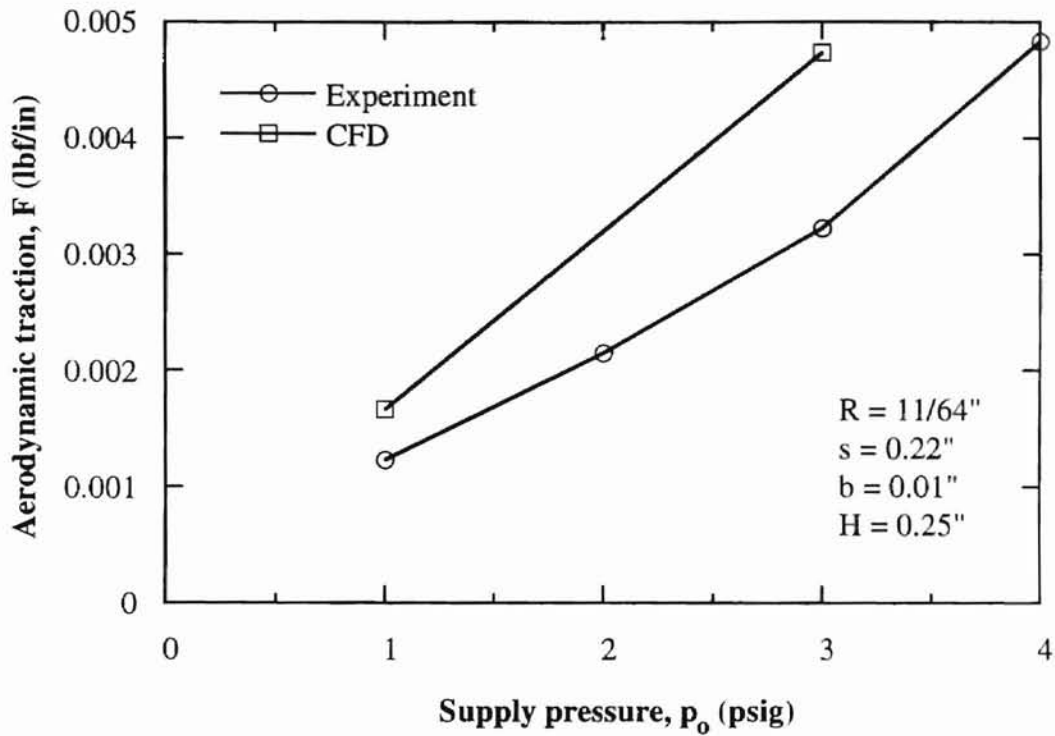
Figure 100. Comparison of traction on the rigid web (H = 0.25 in)
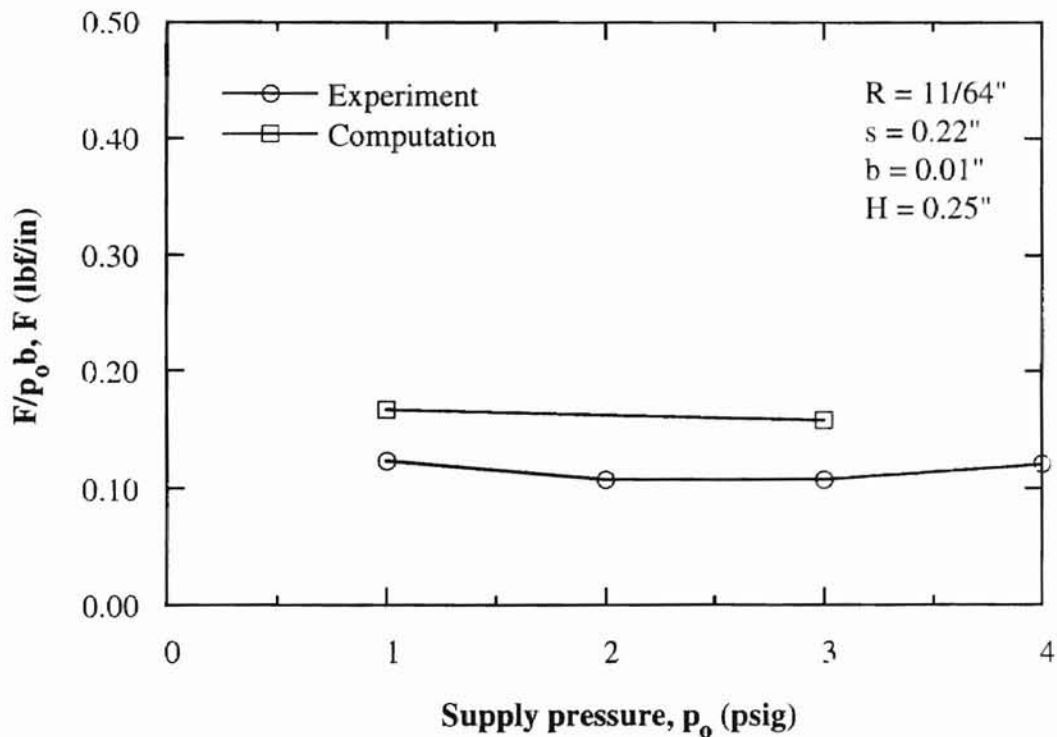
Figure 101. Comparison of non-dimensional traction on the rigid web (H = 0.25 in)

5.2 Aerodynamic Traction on a Flexible Web

It is difficult to compare the measured and computed results because computations were done only for one value of supply pressure (1 psig) and the range of web tension for experiments (0.083 to 0.417 lbf/in) is different from that for computations (0.417 to 10 lbf/in). It is seen, however, that the measured and computed values of traction for the supply pressure of 1 psig seem to be close to each other regardless of web tension (Figure 102 and Figure 103). Figure 104 and Figure 105 show the measured and computed tractions for various values of web tension. The measured and computed deflection profiles of the web for $H_o = 0.25"$ and $p_o = 1$ psig do not agree well (Figure 106).
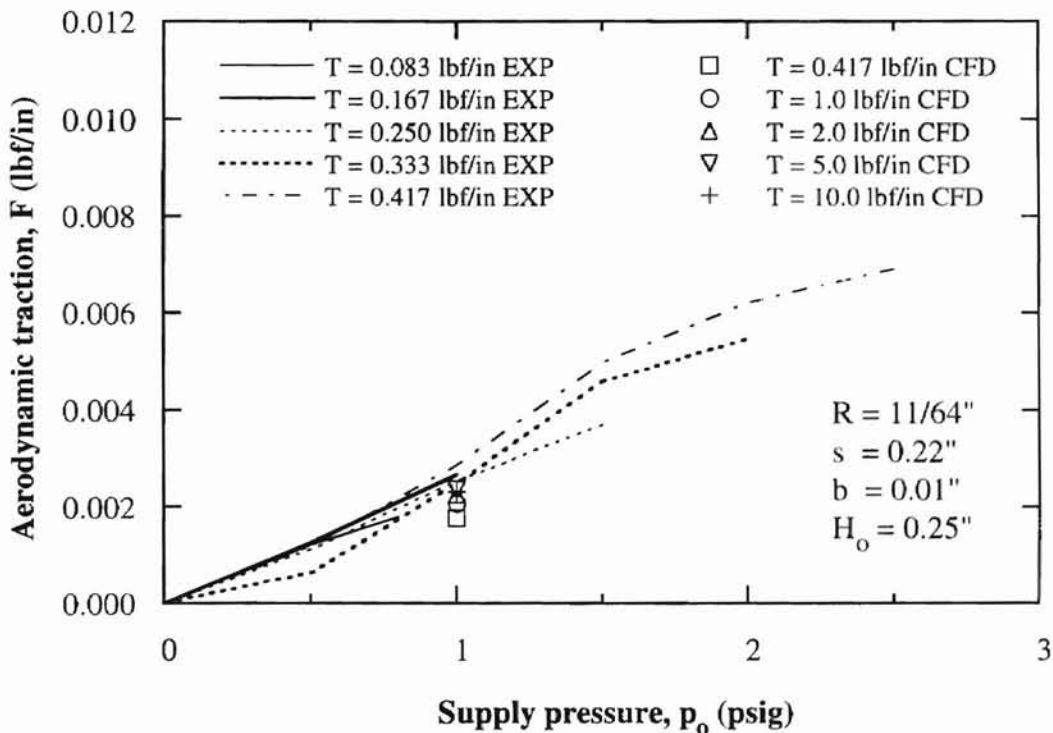
Figure 102. Comparison of traction on the flexible web ($H_o = 0.25$ in)
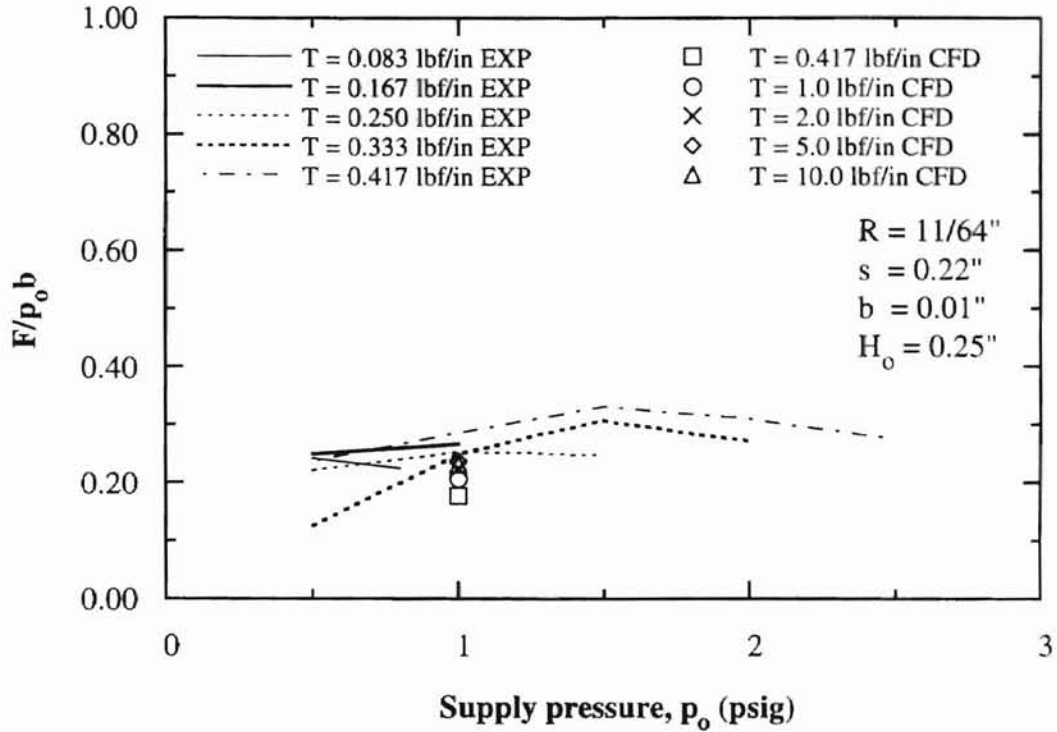
Figure 103. Comparison of non-dimensional traction on the flexible web ($H_o = 0.25$ in)
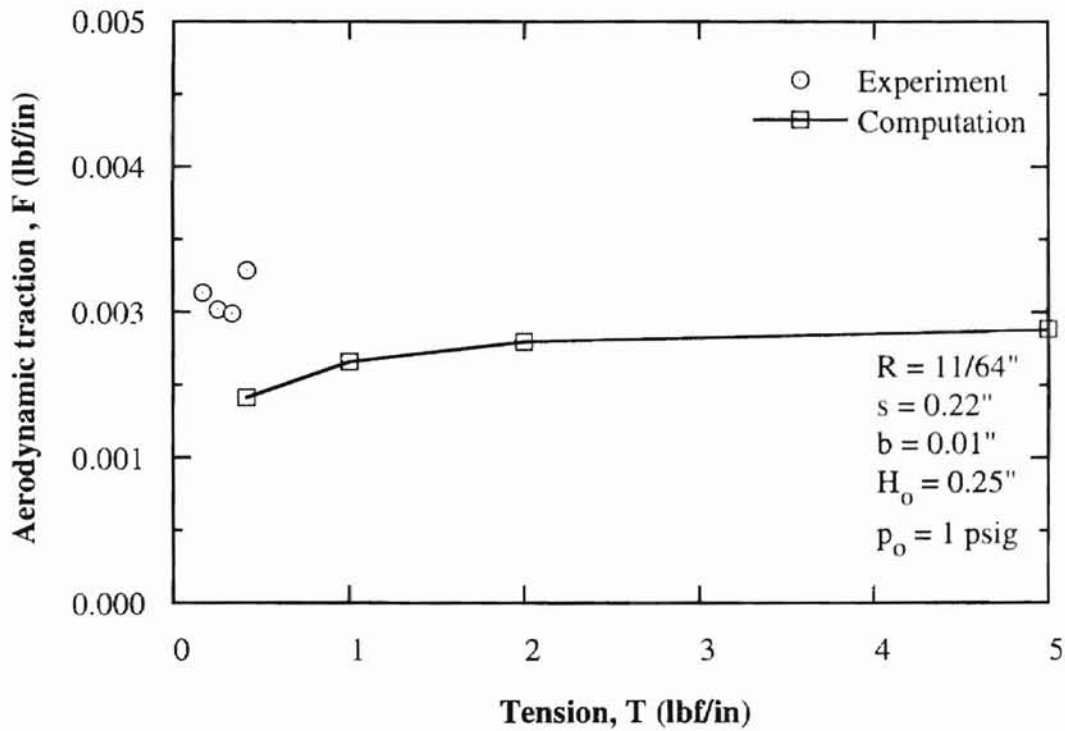
Figure 104. Comparison of traction on the flexible web ($H_o = 0.25$ in, $p_o = 1$ psig)

100
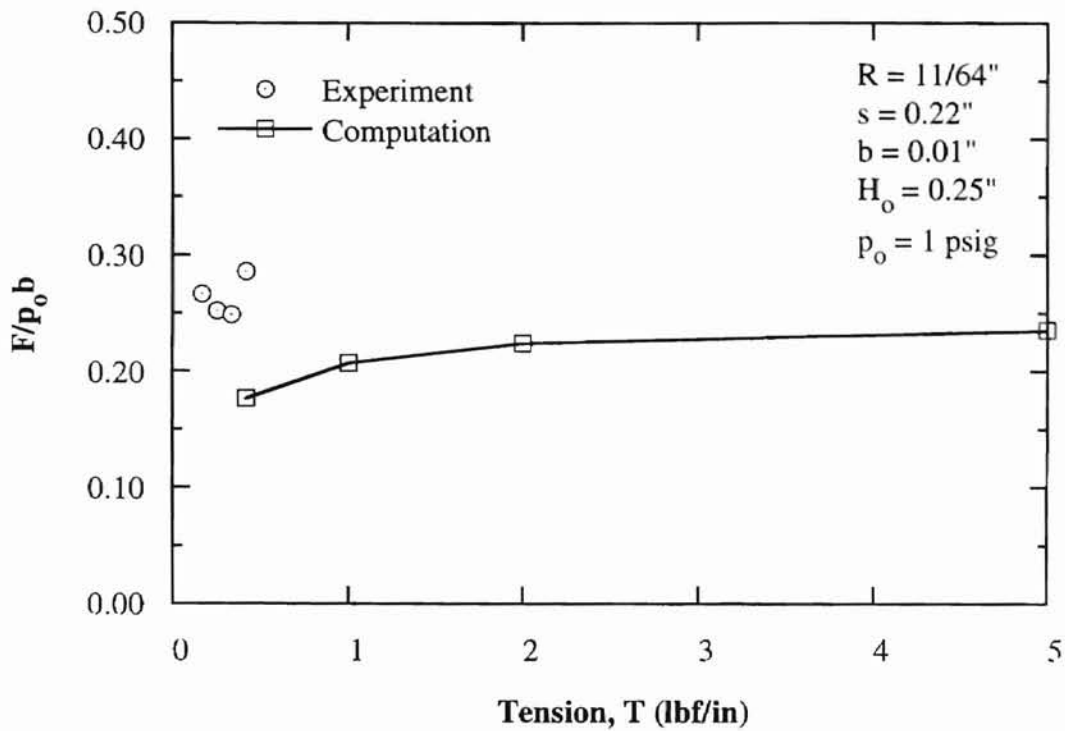
Figure 105. Comparison of non-dimensional traction on the flexible web ($H_o = 0.25$ in, $p_o = 1$ psig)
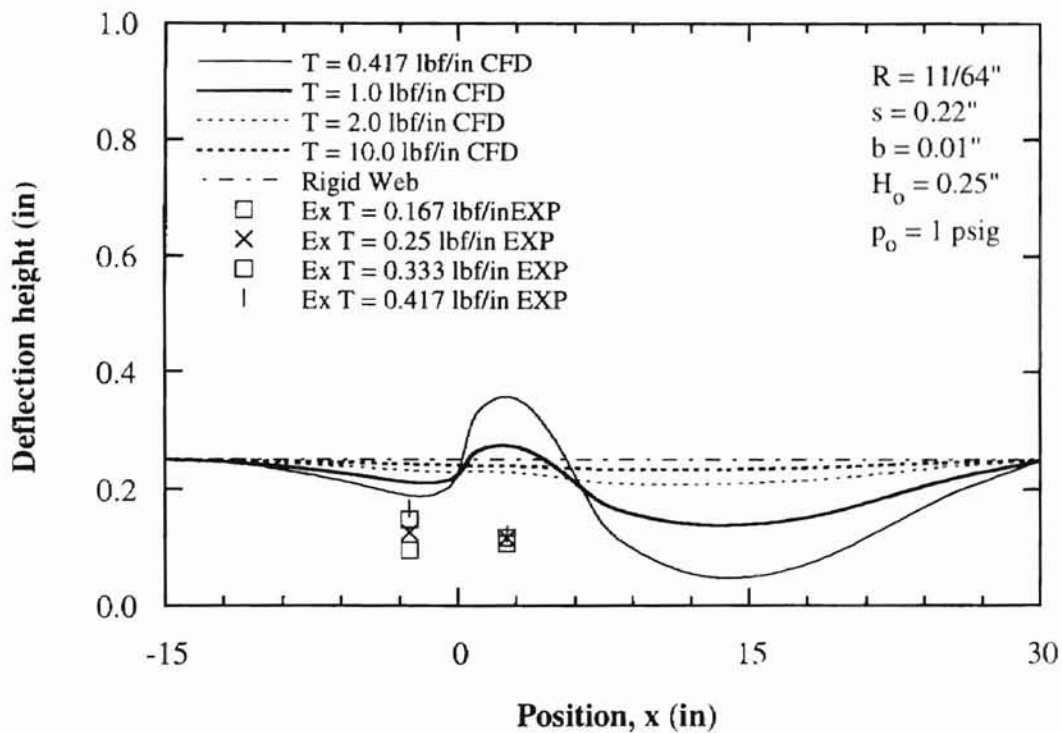
Figure 106. Comparison of deflection profile on the flexible web ($H_o = 0.25$ in, $p_o = 1$ psig)

CHAPTER VI

CONCLUSIONS

The following conclusions can be drawn from this experimental and computational study:

1) The magnitudes of peak pressures on a stationary rigid web subjected to the Coanda air jet are linearly proportional to the supply pressure.

2) The floatation height of H = 0.25" is the equilibrium position for a stationary rigid web for the nozzle width of b = 0.01". This value of floatation height is almost unaffected by supply air pressure.

3) The aerodynamic traction on a stationary rigid web is almost linearly proportional to the supply pressure.

4) The measured aerodynamic traction on a stationary flexible web is almost linearly proportional to the supply air pressure.

5) Computational results show that both the static pressure and the aerodynamic traction on a moving rigid web decrease with the translation speed of the web when the air jet is in the same direction of web motion.

6) The effects of web speed on the static pressure and the aerodynamic drag become less significant when the supply air pressure is high.

7) When a rigid web is subjected to the Coanda air jet, a stagnation zone can appear. Such a zone where the flow is stagnant disappears when the web translates.

8) The aerodynamic traction on a flexible web has no significant relationship with the height of web supports.

9) The aerodynamic traction on a flexible web increases with web tension within the test ranges.

10) The measured traction of the air jet is in the range of 20 – 30 percent of the supply pressure multiplied by the width of the air jet, $F/p_o b = 0.2 - 0.3$, in most test conditions of the flexible web. This relationship needs to be confirmed for various values of the nozzle width (b).

CHAPTER VII

RECOMMENDATIONS FOR FUTURE STUDY

The following recommendations are made for future study:

1) Study the effects of web speed on the interaction between a flexible web and the Coanda air jet.

2) Measure both the out-of-plane deflection profile of a stationary flexible web and the aerodynamic traction in a wider range of test conditions.

3) Flow velocity profile near the nozzle should be measured and compared with the computed profile for the validity of the computation model.

4) Measure the value of non-dimensional traction ($F/p_o b$) as a function of web tension, supply air pressure (p_o), nozzle opening (b), location of web supports (H_o), and the radius of curvature of the nozzle (R).

5) Develop design methods for flutter-free nozzles.

104

REFERENCES

Aravamudhan, V. R., Moretti, P. M., and Chang, Y. B., "An Experimental Study of the Coanda Effect for 90° Turning of Subsonic Air Jets," Presented at the 1998 ASME Fluids Engineering Division Summer Meeting, June, 1998, Washington, DC.

Aravamudhan, V. R., "An Experimental Study of the Coanda Air Jet and its Application to Web Support and Traction," M.S. Thesis, Oklahoma State University, 1998.

Bourque, C. and Newman, B. G., "Reattachment of a Two-Dimensional, Incompressible Jet to an Adjacent Flat Plate," *Aeronautical Quarterly*, Vol. 11, 1960, pp. 192-204.

Cornelius, K. C. and Lucius, G. A., "Physics of a Coanda Jet Detachment at High-Pressure Ratio," *Journal of Aircraft*, Vol. 31, No 3, 1994, pp. 591-597.

Felsing, G. W. and Moller, P. S., "Coanda Flow Over a Circular Cylinder With Injection Normal to the Surface," *AIAA Journal*, Vol. 7, No. 5, 1969, pp. 842-846.

Kline, S. J. and McClintock, F. A.. "Describing Uncertainties in Single-Sample Experiments," *Mechanical Engineering*, Vol. 1, January, 1953, pp. 3-8.

Murai, K., Kawashima, Y., Nakanishi, S., and Taga, M., "Self-Oscillation Phenomena of Turbulent Jets in a Channel," *Canadian Journal of Chemical Engineering*, Vol. 67, 1989, pp. 906-911.

Reba, I., "Applications of the Coanda Effect," *Scientific American*, Vol. 214, No. 6, 1966, pp. 84-92.

Rodman, L. C., Wood, N. J., and Roberts, L., "Experimental Investigation of Straight and Curved Annular Wall Jets," *AIAA Journal*, Vol. 27, No. 8, 1989, pp. 1059-1067.

Richmond, M. C. and Patel, V. C., "Convex and Concave Surface Curvature Effects in Wall-Bounded Turbulent Flows," *AIAA Journal*, Vol. 29, No. 6, 1991, pp. 895-902.

Sawada, K. and Asami, K., "Numerical Study on the Underexpanded Coanda Jet," *Journal of Aircraft*, Vol. 34, No. 5, 1997, pp. 641-647.

Squire, H. B., "Jet Flow and It's Effect on Aircraft," *Aircraft Engineering*, Vol. 22, March 1950.

Thirumal, S. P., "A Computational Study of the Coanda Effect and Its Implementation in Web Support and Traction," M.S. Thesis, Oklahoma State University, 1998.

Wetmore, A. C., "Evaluation of a Coanda Nozzle for Pneumatic Conveying," M.S. Thesis, Oklahoma State University, 1972.

White, F. M., *Viscous Fluid Flow*, 2nd Edition, McGraw-Hill International Editions, 1974.

Wille, R. and Fernholz, H., "Report on the First European Mechanics Colloquium on the Coanda Effect," *Journal of Fluid Mechanics*, Vol. 23, No. 4, 1965, pp. 801-819.

APPENDIX A

C PROGRAM FOR CALCULATION OF THE WEB DEFLECTION PROFILE

```c
#include<stdio.h>
#include<math.h>
#include<iostream.h>


#define SWAP(a,b) {dum=(a);(a)=(b);(b)=dum;}
#define TINY     1.0e-20
#define N        3000                              // maximum number of data is 3000
#define M1       2                                 // band size of matrix a[][]
#define T        0.333                             // tension [lbf/in]
#define E        1.0e+5                            // Young's Modulus (Psi)
#define t        3.0e-3                            // Web thickness (inches)
#define NU       0.4                               // Poison's ratio
#define D        ( E*pow(t,3)/(12*(1.0-NU*NU)) )   // bending stiffness of web
#define P_AMB    0                                 // Psi  14.7

void initial(double a[][6], double al[][6], unsigned long [], double []);  // a, P1, H1, P2, HS
void shell(double a[][6], double al[][6], unsigned long [], double [], double []);     // H, P1, P2
void solve(double a[][6], unsigned long, int, int, double al[][6], unsigned long [], float&);
void solve2(double a[][6], unsigned long, int, int, double al[][6], unsigned long [], double[]);
void output(double []);

int n;
FILE *fi;
double percent,X[N+5];


void main()
{
  double H[N+5],P[N+5],a[N+5][M1+M2+2],al[N+5][M1+M2+2];
  unsigned long indx[N+5];

  cout << " Enter the total number of data ?";
  cin >> n;
  n = n-2;               // two of them are boundary points

  cout << " Enter the weight factor, percent of the  profile ?";
  cin >> percent;

  initial(a, al, indx, P);    // 1. Read initial pressure and location profile
```

```
                              // 2. Set DX matrix
                              // 3. Set tirdiagonal coefficient matrix for shell equation

      // solve the shell equation
      shell(a, al, indx, P, H);

      // print out the result, gap profile H[i]
      output(H);
}


void initial(double a[][6], double al[][6], unsigned long indx[], double P[])
{
   int i;
   double DX[N+5];
   float d;

   // read initial pressure profiles
   //fi = fopen("input_p1_t2.5_28.txt","r");      // 10initial.txt is input file
   fi = fopen("input_p1_t0.333_4.txt","r");

   for(i = 0; i<=n+1; i++)
      fscanf(fi, "%lf", &X[i]);          // read poisition in inches
   for(i = 0; i<=n+1; i++)
      fscanf(fi, "%lf", &P[i]);          // read pressure in Psi(absolute)
   fclose(fi);

   // making DX matrix
   for(i=1 ; i<=n ;i++)
                  DX[i]=X[i]-X[i-1];

   // calculate compactly stored array a[][] for shell equation
            a[1][1] =   0.0;                // useless element      first prime at n=0
            a[1][2] =   0.0;                // useless element
            a[1][3] =   7.0*D/pow(DX[1],4) + (31.0/12.0)*T/pow(DX[1],2);
            a[1][4] = -4.0*D/pow(DX[1],4) - ( 4.0/3.0 )*T/pow(DX[1],2);
            a[1][5] =       D/pow(DX[1],4) + ( 1.0/12.0)*T/pow(DX[1],2);

            a[2][1] =   0.0;                // useless element
            a[2][2] =   -4.0*D/pow(DX[2],4) - (4.0/3.0)*T/pow(DX[2],2);
            a[2][3] =   6.0*D/pow(DX[2],4) + (5.0/2.0)*T/pow(DX[2],2);
            a[2][4] =   -4.0*D/pow(DX[2],4) - (4.0/3.0)*T/pow(DX[2],2);
            a[2][5] =       D/pow(DX[2],4) +(1.0/12.0)*T/pow(DX[2],2);

            for( i=3 ; i<=n-2 ; i++) {
                     a[i][1] =       D/pow(DX[i],4) + (1.0/12.0)*T/pow(DX[i],2);
                     a[i][2] = - 4.0*D/pow(DX[i],4) - (4.0/3.0 )*T/pow(DX[i],2);
                     a[i][3] =   6.0*D/pow(DX[i],4) + (5.0/2.0 )*T/pow(DX[i],2);
                     a[i][4] = - 4.0*D/pow(DX[i],4) - (4.0/3.0 )*T/pow(DX[i],2);
                     a[i][5] =       D/pow(DX[i],4) + (1.0/12.0)*T/pow(DX[i],2);
            }

            a[n-1][1] =       D/pow(DX[n-1],4) + (1.0/12.0)*T/pow(DX[n-1],2);
            a[n-1][2] = -4.0*D/pow(DX[n-1],4) - (4.0/3.0 )*T/pow(DX[n-1],2);
            a[n-1][3] =   6.0*D/pow(DX[n-1],4) + (5.0/2.0 )*T/pow(DX[n-1],2);
```

108

```
        a[n-1][4] = -4.0*D/pow(DX[n-1],4) - (4.0/3.0 )*T/pow(DX[n-1],2);
        a[n-1][5] =  0.0;  // useless element  first prime at n=n+1

        a[n][1] =      D/pow(DX[n],4) + ( 1.0/12.0)*T/pow(DX[n],2);
        a[n][2] = -4.0*D/pow(DX[n],4) - ( 4.0/3.0 )*T/pow(DX[n],2);
        a[n][3] =  7.0*D/pow(DX[n],4) + (31.0/12.0)*T/pow(DX[n],2);
   a[n][4] =   0.0;           // useless element
        a[n][5] =  0.0;               // useless element

  // LU decomposition : modifiy a[][] and al[][].
  // indx[] is the information of pivoting which will use solving matrix
        solve(a, n, M1, M2, al, indx, d);

}


void shell(double a[][6],double al[][6],unsigned long indx[],double P[],double H[]) //[A]{H}={E}
{
        register int i;
        double f[N+5];

  // calculate the coefficient, f[]
        for( i=1 ; i<=n ; i++)
                f[i] =  P[i]-P_AMB;

  // then solve shell equation
        solve2(a, n, M1, M2, al, indx, f);                 // output f[]

  // Transfer output f[] to H[]
        for(i=1 ; i<=n ; i++)
                H[i] = f[i];
  // Set Boundary Points
        H[0] = 0;
        H[n+1] =0;

}


void output(double H[])
{
 int i;
 //fi = fopen("output_p1_t2.5_28.txt","w");
 fi = fopen("output_p1_t0.333_4.txt","w");

 fprintf(fi,"\n   X[inches]   H[inches]  percent= %lf\n",percent);
 for(i=0; i<=n+1 ; i++)
        fprintf(fi,"\n %e   %e",X[i],H[i]*percent);
 fclose(fi);
}


// this is a function for solving band diagonal system
// Note : LU decomposition method for band diagonal matrix.
void solve(double a[][6], unsigned long n, int m1, int m2, double al[][6], unsigned long indx[], float& d)
/*
```

109

Given an n*n band diagonal matrix A with m1 subdiagonal rows and m2 superdiagonal rows.
compactly stored array, a[1..n][[1,,m1+m2+1] The upper triangular matrix replaces a, while
the lower triangular matrix is returned in al[1..n][1..m1]. indx[1..n] is an output vector
which records the row permutation affected by the partial pivoting; d is output as +-1
depending on whether the number of row interchanges was even or odd, respectively.
*/

```
{
        unsigned long i,j,k,l;
        int mm;
        double dum;
        mm=m1+m2+1;
        l=m1;
        for (i=1; i<=m1 ;i++) {
                for (j=m1+2-i ; j<=mm ; j++) a[i][j-1]=a[i][j];
                l--;
                for (j=mm-l; j<=mm ; j++) a[i][j]=0.0;
        }
        d=1.0;
        l=m1;
        for (k=1; k<=n ; k++) {
                dum=a[k][1];
                i=k;
                if (l < n) l++;
                for (j=k+1; j<=l ; j++) {    // Find the povot element.
                        if (fabs( a[j][1]) > fabs(dum)) {
                                dum=a[j][1];
                                i=j;
                        }
                }
                indx[k]=i;
                if (dum == 0.0) a[k][1]=TINY;
                // Matrix is algotithmically singular, but proceed anyway
                // with TINY povot
                if (i != k) {       // interchange rows.
                        d = -(d);
                        for (j=1 ; j<=mm ; j++) SWAP(a[k][j],a[i][j])
                }
                for (i=k+1 ; i<=l ; i++) {              // elimination
                        dum = a[i][1]/a[k][1];
                        al[k][i-k]=dum;
                        for (j=2; j<=mm ; j++) a[i][j-1]=a[i][j]-dum*a[k][j];
                        a[i][mm]=0.0;
                }
        }
}
```

void solve2(double a[][6], unsigned long n, int m1, int m2, double al[][6], unsigned long indx[], double b[])
/*
Given arrays a, al,and indx as returned from solve, and given a right-hand side vector
b[1..n], solves the band diagonal linear equations A*x=b.
The solution vector x overwtires b[1..n]. The other input arrays are not modified.
and can be left in place for successive calls with different right-hand sides.
*/

```
{
        unsigned long i,k,l;
```

```
int mm;
double dum;

mm=m1+m2+1;
l=m1;
for (k=1 ; k<=n ; k++) {     // Forward substitution
        i=indx[k];
        if (i != k) SWAP(b[k],b[i])
        if (l < n) l++;
        for (i=k+1 ; i<=l ; i++) b[i] -= al[k][i-k]*b[k];
}
l=1;
for (i=n ; i>=1 ; i--) {                    //Back substitution
        dum=b[i];
        for (k=2 ; k<=l ; k++) dum -= a[i][k]*b[k+i-1];
        b[i]=dum/a[i][1];
        if (l < mm) l++;
}
}
```

APPENDIX B

ADDITIONAL TABLES

Table 7. Aerodynamic traction on the flexible web ($H_o = 0.00''$)

Web tension, T (lbf/in)	Supply air pressure, p_o (psig)	Measured traction, F (lbf/in)
0.083	0.0	0.00000
	0.5	0.00074
	1.0	0.00163
0.333	0.0	0.00000
	0.5	0.00029
	1.0	0.00068
	1.5	0.00153
	2.0	0.00209
	2.5	0.00238
0.417	0.0	0.00000
	0.5	0.00070
	1.0	0.00200
	1.5	0.00338
	2.0	0.00486

Table 8. Non-dimensional traction on the flexible web ($H_o = 0.00''$)

Web tension, T (lbf/in)	Supply air pressure, p_o (psig)	Non-dimensional traction, $F/p_o b$
0.083	0.5	0.14778
	1.0	0.16333
0.333	0.5	0.05889
	1.0	0.06833
	1.5	0.10222
	2.0	0.10472
	2.5	0.09512
0.417	0.5	0.14000
	1.0	0.20000
	1.5	0.22519
	2.0	0.24278

Table 9. Aerodynamic traction on the flexible web ($H_o = 0.25"$)

Web tension, T (lbf/in)	Supply air pressure, p_o (psig)	Measured traction, F (lbf/in)
0.083	0.0	0.00000
	0.5	0.00089
	1.0	0.00252
	1.5	0.00323
0.333	0.0	0.00000
	0.5	0.00112
	1.0	0.00166
	1.5	0.00346
	2.0	0.00432
0.417	0.0	0.00000
	0.5	0.00121
	1.0	0.00173
	1.5	0.00417
	2.0	0.00526
	2.5	0.00617

Table 10. Non-dimensional traction on the flexible web ($H_o = 0.25"$)

Web tension, T (lbf/in)	Supply air pressure, p_o (psig)	Non-dimensional traction, $F/p_o b$
0.083	0.5	0.17750
	1.0	0.25166
	1.5	0.26910
0.333	0.5	0.22334
	1.0	0.16556
	1.5	0.23037
	2.0	0.21611
0.417	0.5	0.24112
	1.0	0.17278
	1.5	0.27815
	2.0	0.26278
	2.5	0.24667

Table 11. Aerodynamic traction on the flexible web ($H_o = 0.50"$)

Web tension, T (lbf/in)	Supply air pressure, p_o (psig)	Measured traction, F (lbf/in)
0.083	0.0	0.00000
	0.5	0.00116
	1.0	0.00245
	1.5	0.00268
0.333	0.0	0.00000
	0.5	0.00079
	1.0	0.00212
	1.5	0.00343
	2.0	0.00457
	2.5	0.00561
0.417	0.0	0.00000
	0.5	0.00055
	1.0	0.00236
	1.5	0.00395
	2.0	0.00553
	2.5	0.00674
	3.0	0.00782

Table 12. Non-dimensional traction on the flexible web ($H_o = 0.50"$)

Web tension, T (lbf/in)	Supply air pressure, p_o (psig)	Non-dimensional traction, $F/p_o b$
0.083	0.5	0.23222
	1.0	0.24445
	1.5	0.24394
0.333	0.5	0.15778
	1.0	0.21167
	1.5	0.22889
	2.0	0.22834
	2.5	0.22444
0.417	0.5	0.11083
	1.0	0.23625
	1.5	0.26333
	2.0	0.27646
	2.5	0.26950
	3.0	0.26069

114

Table 13. Aerodynamic traction on the flexible web ($H_o = 1.00"$)

Web tension, T (lbf/in)	Supply air pressure, p_o (psig)	Measured traction, F (lbf/in)
0.083	0.0	0.00000
	0.5	0.00118
	1.0	0.00245
0.333	0.0	0.00000
	0.5	0.00071
	1.0	0.00142
	1.5	0.00254
	2.0	0.00334
	2.5	0.00444
	3.0	0.00543
0.417	0.0	0.00000
	0.5	0.00091
	1.0	0.00243
	1.5	0.00277
	2.0	0.00334
	2.5	0.00400
	3.0	0.00520
	3.5	0.00643

Table 14. Non-dimensional traction on the flexible web ($H_o = 1.00"$)

Web tension, T (lbf/in)	Supply air pressure, p_o (psig)	Non-dimensional traction, $F/p_o b$
0.083	0.5	0.23666
	1.0	0.24500
0.333	0.5	0.14250
	1.0	0.14208
	1.5	0.16917
	2.0	0.16688
	2.5	0.17750
	3.0	0.18083
0.417	0.5	0.18250
	1.0	0.24250
	1.5	0.18472
	2.0	0.16708
	2.5	0.16017
	3.0	0.17333
	3.5	0.18357

Table 15. Aerodynamic traction on the flexible web ($H_o = 0.25"$, $T = 0.083$ lbf/in)

Test runs	Supply air pressure, p_o (psig)	Measured traction, F (lbf/in)
1st	0.0	0.00000
	0.5	0.00160
	0.8	0.00250
2nd	0.0	0.00000
	0.5	0.00165
	0.8	0.00252
3rd	0.0	0.00000
	0.5	0.00133
	0.8	0.00205
4th	0.0	0.00000
	0.5	0.00135
	0.8	0.00207
5th	0.0	0.00000
	0.5	0.00150
	0.8	0.00222
6th	0.0	0.00000
	0.5	0.00155
	0.8	0.00225
7th	0.0	0.00000
	0.5	0.00153
	0.8	0.00225
8th	0.0	0.00000
	0.5	0.00157
	0.8	0.00213

Table 16. Non-dimensional traction on the flexible web ($H_o = 0.25"$, $T = 0.083$ lbf/in)

Test runs	Supply air pressure, p_o (psig)	Non-dimensional traction, $F/p_o b$
1st	0.5	0.32000
	0.8	0.31250
2nd	0.5	0.33000
	0.8	0.31459
3rd	0.5	0.26666
	0.8	0.25625
4th	0.5	0.27000
	0.8	0.25834
5th	0.5	0.30000
	0.8	0.27708
6th	0.5	0.31000
	0.8	0.28125
7th	0.5	0.30667
	0.8	0.28125
8th	0.5	0.31333
	0.8	0.26667
Average		0.28007

116

Table 17. Aerodynamic traction on the flexible web ($H_o = 0.25$", $T = 0.167$ lbf/in)

Test runs	Supply air pressure, p_o (psig)	Measured traction, F (lbf/in)
1st	0.0	0.0000
	0.5	0.00153
	1.0	0.00325
2nd	0.0	0.00000
	0.5	0.00162
	1.0	0.00312
3rd	0.0	0.00000
	0.5	0.00140
	1.0	0.00288
4th	0.0	0.00000
	0.5	0.00133
	1.0	0.00293
5th	0.0	0.00000
	0.5	0.00115
	1.0	0.00242
6th	0.0	0.00000
	0.5	0.00108
	1.0	0.00242

Table 18. Non-dimensional traction on the flexible web ($H_o = 0.25$", $T = 0.167$ lbf/in)

Test runs	Supply air pressure, p_o (psig)	Non-dimensional traction, $F/p_o b$
1st	0.5	0.30666
	1.0	0.32500
2nd	0.5	0.32334
	1.0	0.31167
3rd	0.5	0.28000
	1.0	0.28833
4th	0.5	0.26666
	1.0	0.29333
5th	0.5	0.23000
	1.0	0.24167
6th	0.5	0.21666
	1.0	0.24167
Average		0.25792

Table 19. Aerodynamic traction on the flexible web ($H_o = 0.25"$, $T = 0.250$ lbf/in)

Test runs	Supply air pressure, p_o (psig)	Measured traction, F (lbf/in)
1st	0.0	0.00000
	0.5	0.00135
	1.0	0.00287
	1.5	0.00450
2nd	0.0	0.00000
	0.5	0.00150
	1.0	0.00282
	1.5	0.00475
3rd	0.0	0.00000
	0.5	0.00108
	1.0	0.00228
	1.5	0.00392
4th	0.0	0.00000
	0.5	0.00100
	1.0	0.00227
	1.5	0.00390
5th	0.0	0.00000
	0.5	0.00090
	1.0	0.00177
	1.5	0.00265
6th	0.0	0.00000
	0.5	0.00098
	1.0	0.00185
	1.5	0.00277
7th	0.0	0.00000
	0.5	0.00094
	1.0	0.00181
	1.5	0.00271
8th	0.0	0.00000
	0.5	0.00122
	1.0	0.00367
	1.5	0.00458

Table 20. Non-dimensional traction on the flexible web ($H_o = 0.25"$, $T = 0.250$ lbf/in)

Test runs	Supply air pressure, p_o (psig)	Non-dimensional traction, $F/p_o b$
1st	0.5	0.27000
	1.0	0.28667
	1.5	0.30000
2nd	0.5	0.30000
	1.0	0.28167
	1.5	0.31667
3rd	0.5	0.21666
	1.0	0.22833
	1.5	0.26111
4th	0.5	0.20000
	1.0	0.22667
	1.5	0.26000
5th	0.5	0.18000
	1.0	0.17667
	1.5	0.17667
6th	0.5	0.19667
	1.0	0.18500
	1.5	0.18445
7th	0.5	0.18833
	1.0	0.18083
	1.5	0.18056
8th	0.5	0.24333
	1.0	0.36667
	1.5	0.30556
Average		0.24009

Table 21. Aerodynamic traction on the flexible web ($H_o = 0.25"$, $T = 0.333$ lbf/in)

Test runs	Supply air pressure, p_o (psig)	Measured traction, F (lbf/in)
1st	0.0	0.00000
	0.5	0.00050
	1.0	0.00283
	1.5	0.00512
	2.0	0.00605
2nd	0.0	0.00000
	0.5	0.00062
	1.0	0.00268
	1.5	0.00510
	2.0	0.00597
3rd	0.0	0.00000
	0.5	0.00087
	1.0	0.00290
	1.5	0.00495
	2.0	0.00610
4th	0.0	0.00000
	0.5	0.00083
	1.0	0.00288
	1.5	0.00495
	2.0	0.00597
5th	0.0	0.0000
	0.5	0.00047
	1.0	0.00183
	1.5	0.00375
	2.0	0.00432
6th	0.0	0.00000
	0.5	0.00047
	1.0	0.00182
	1.5	0.00377
	2.0	0.00433

Table 22. Non-dimensional traction on the flexible web ($H_o = 0.25"$, $T = 0.333$ lbf/in)

Test runs	Supply air pressure, p_o (psig)	Non-dimensional traction, $F/p_o b$
1st	0.5	0.10000
	1.0	0.28333
	1.5	0.34111
	2.0	0.30250
2nd	0.5	0.12333
	1.0	0.26833
	1.5	0.34000
	2.0	0.29833
3rd	0.5	0.17333
	1.0	0.29000
	1.5	0.33000
	2.0	0.30500
4th	0.5	0.16667
	1.0	0.28833
	1.5	0.33000
	2.0	0.29833
5th	0.5	0.09333
	1.0	0.18333
	1.5	0.25000
	2.0	0.21584
6th	0.5	0.093334
	1.0	0.18167
	1.5	0.25111
	2.0	0.21666
Average		0.23850

Table 23. Aerodynamic traction on the flexible web ($H_o = 0.25"$, $T = 0.417$ lbf/in)

Test runs	Supply air pressure, p_o (psig)	Measured traction, F (lbf/in)
1st	0.0	0.00000
	0.5	0.00082
	1.0	0.00385
	1.5	0.00822
	2.0	0.01023
	2.5	0.01128
2nd	0.0	0.00000
	0.5	0.00085
	1.0	0.00382
	1.5	0.00823
	2.0	0.01015
	2.5	0.01143
3rd	0.0	0.00000
	0.5	0.00210
	1.0	0.00402
	1.5	0.00582
	2.0	0.00718
	2.5	0.00795
4th	0.0	0.00000
	0.5	0.00215
	1.0	0.00403
	1.5	0.00585
	2.0	0.00718
	2.5	0.00800
5th	0.0	0.00000
	0.5	0.00057
	1.0	0.00072
	1.5	0.00082
	2.0	0.00123
	2.5	0.00137
6th	0.0	0.00000
	0.5	0.00060
	1.0	0.00072
	1.5	0.00092
	2.0	0.00125
	2.5	0.00140

Table 24. Non-dimensional traction on the flexible web (H_o = 0.25", T = 0.417 lbf/in)

Test runs	Supply air pressure, p_o (psig)	Non-dimensional traction, $F/p_o b$
1st	0.5	0.16333
	1.0	0.38500
	1.5	0.54778
	2.0	0.51165
	2.5	0.45132
2nd	0.5	0.17000
	1.0	0.38167
	1.5	0.54889
	2.0	0.50750
	2.5	0.45732
3rd	0.5	0.42000
	1.0	0.40167
	1.5	0.38778
	2.0	0.35917
	2.5	0.33125
4th	0.5	0.43000
	1.0	0.40333
	1.5	0.39000
	2.0	0.35917
	2.5	0.33195
5th	0.5	0.11333
	1.0	0.07167
	1.5	0.05445
	2.0	0.06167
	2.5	0.05467
6th	0.5	0.12000
	1.0	0.071667
	1.5	0.061111
	2.0	0.062500
	2.5	0.056000
Average		0.28886

Table 25. Aerodynamic traction on the flexible web ($H_o = 0.25"$)

Web tension T (lbf/in)	Supply air pressure, p_o (psig)	Measured traction, F (lbf/in)
0.083	0.0	0.0000
	0.5	0.00121
	0.8	0.00180
0.167	0.0	0.0000
	0.5	0.0012
	1.0	0.00267
0.250	0.0	0.0000
	0.5	0.00111
	1.0	0.00252
	1.5	0.00370
0.333	0.0	0.0000
	0.5	0.00063
	1.0	0.00249
	1.5	0.00461
	2.0	0.00546
0.417	0.0	0.00000
	0.5	0.00118
	1.0	0.00286
	1.5	0.00498
	2.0	0.00621
	2.5	0.00690

Table 26. Non-dimensional traction on the flexible web ($H_o = 0.25"$)

Web tension, T (lbf/in)	Supply air pressure, p_o (psig)	Non-dimensional traction, $F/p_o b$
0.083	0.5	0.24167
	1.0	0.22479
0.167	0.5	0.24900
	1.0	0.26683
0.250	0.5	0.22153
	1.0	0.25229
	1.5	0.24644
0.333	0.5	0.12500
	1.0	0.24916
	1.5	0.30704
	2.0	0.27278
0.417	0.5	0.23611
	1.0	0.28583
	1.5	0.33167
	2.0	0.31027
	2.5	0.27600
Average		0.256026

124

VITA

Eui Yeol Hong

Candidate for the Degree of

Master of Science

Thesis: AERODYNAMIC FORCES ON A WEB
SUBJECTED TO THE COANDA AIR JET

Major Field: Mechanical Engineering

Biographical:

Personal Data: Born in Seoul, Korea, on March 7, 1975, the son of
Mr. K. H. Hong and Mrs. S. R. Oh.

Education: Received Bachelor of Engineering degree in Mechanical
Engineering from Kon-Kuk University, Seoul, Korea in February
1997. Completed the requirements for Master of Science degree
with a major in Mechanical Engineering at Oklahoma State
University in December 1999.

Experience: Research Assistant, Mechanical and Aerospace Engineering,
Oklahoma State University from January 1998 to present.